DESIGN OF GRAPHITIC CARBON MATERIALS FOR ELECTROCHEMICAL ENERGY CONVERSION AND STORAGE

A Dissertation

by

GANG YANG

Submitted to the Office of Graduate and Professional Studies of
Texas A&M University
in partial fulfillment of the requirements for the degree of

DOCTOR OF PHILOSOPHY

Chair of Committee,	Choongho Yu
Committee Members,	Arum Han
	Hong Liang
	Partha Mukherjee
Head of Department,	Andreas A. Polycarpou

August 2017

Major Subject: Mechanical Engineering

ABSTRACT

The climate change induced by greenhouse gas emissions has urged us to look for alternative energy sources instead of relying on burning fossil fuels. Converting chemical energy to electrical energy through a zero-emission path has been regarded as a clean way for this purpose. On the other hand, storing energy from renewable energy sources such as wind and solar is another way to reduce the greenhouse gas emissions. Therefore it is of vital importance to develop electrochemical systems with high energy conversion and storage efficiency. The key of electrochemical systems is electrode, where all electrochemical reactions are happening. This work is about designing graphitic carbon based materials to improve the energy conversion and storage efficiencies in fuel cells and lithium batteries.

Fuel cells have been regarded as attractive systems for the next generation energy conversion because of their high efficiency and low emission together with their modular and distributed nature and zero noise pollution. The most limiting factor comes from the cathode, where expensive Pt catalysts are necessary to overcome high activation barriers for the oxygen reduction reaction. In this dissertation, a number of graphitic carbon based catalysts have been developed without using any precious metals to replace the expensive Pt catalysts. The designed catalysts demonstrated outstanding catalytic activity and stability in both acidic and alkaline media. Their high porosity and free-standing nature would further promote mass transfer during the reaction as well as eliminate the use of a

gas diffusion or catalyst supporting layer, indicating a high promise for commercial applications.

Lithium-sulfur batteries theoretically have ~10 times higher energy density than traditional Li-ion batteries. However, the practically low areal capacity and safety issues from lithium anode prevent their commercialization. Here, a catholyte method with an efficient catholyte reservoir has been developed to solve the problem from cathode side. In order to achieve high areal capacities, a sulfur/lithium dual host has been invented to (1) increase active surface area through exfoliation of graphitic layers; (2) create effective nano-reactors to shorten diffusion length of active materials; (3) improve lithium stripping/deposition by creating lithiophilic surface.

ACKNOWLEDGEMENTS

First, I would like to show my appreciations to my advisor Dr. Choongho Yu who has been supporting me, guiding me, and giving me freedom on research. His high standard of and commitment to research influence me to devote myself to the work I love. I also appreciate the suggestions and helps from my committee members, Dr. Arum Han, Dr. Hong Liang, and Dr. Partha Mukherjee, which consistently supports my PhD research.

Second, I want to give many thanks to my lab mates (Dr. Xiong Pu, Dr. Hong Wang, Dr. Sang Won Jee, Dr. Subrata Kundu, Abdullah, Tazebay, Woongchul Choi, Suk Lae Kim, Su-In Yi, Jui-Hung Hsu, Henry Lin, Jian Tan, Yifan Liu), my collaborators (Dr. Arum Han, Dr. Celal Erbay, Dr. Dong Hee Son, Dr. Ho Jin, Dr. Hongcai Zhou, Xinyu Yang, Chris Scotti), and my friends. Without their support and help, I couldn't have made any big progress on my research.

Third, I want to express my sincere gratitude to the ConocoPhillips Graduate Fellowship and Texas A&M Energy Institute for providing the fellowship that allows me to focus more on my research.

Lastly, I cannot overstate my appreciation to my parents, my wife, and my little Aiyou. Deeply buried in my heart are their understanding, sacrifice, and love. They make my day, my year, and my life! Thank You!

CONTRIBUTORS AND FUNDING SOURCES

This work was supported by a dissertation committee consisting of Professor Choongho Yu [advisor], Professor Hong Liang and Professor Partha Mukherjee of the Department of Mechanical Engineering and Professor Arum Han of the Department of Electrical and Computer Engineering.

The microbial fuel cell performance tests for Chapter III was provided by Dr. Celal Erbay. The analyses depicted in Chapter IV were conducted in part by Dr. Xiong Pu and were published in 2015 in an article listed in the Biographical Sketch. The UV-Vis analyses depicted in Chapter V were conducted in part by Dr. Ho Jin.

All other work conducted for the dissertation was completed by the student independently.

Graduate study was supported by a fellowship from Texas A&M Energy Institute and a funding support from National Science Foundation.

NOMENCLATURE

LIBs	Lithium-ion Batteries
Li-S	Lithium-Sulfur
PEM	Proton Exchange Membrane
MFC	Microbial Fuel Cell
CV	Cyclic Voltammetry
SHE	Standard Hydrogen Electrode
HOMO	Highest Occupied Molecular Orbital
LOMO	Lowest Unoccupied Molecular Orbital
CNT	Carbon Nanotube

TABLE OF CONTENTS

Page

LIST OF FIGURES

Page

LIST OF TABLES

Page

CHAPTER I

INTRODUCTION AND LITERATURE REVIEW

1.1 Fundamentals of electrochemical energy conversion and storage

There are two forms of energy in every electrochemical system – electrical energy and chemical energy. The system is normally consisted with electrodes and a medium separating the electrodes from contacting each other. The conversion process is referred to transforming the chemical energy stored in chemicals to electrical energy, while the storage process is vice versa. There are two types of electrodes commonly known as cathode and anode, where all electrochemical reactions are occurring. During operation, reactive chemicals would go through reduction and oxidation reactions, forming electron transfer through the outside circuit. Inside the system, instead of electrons, ions are moving between the anode and cathode to maintain charge neutral at each electrode. There are mainly three types of electrochemical systems being widely used: batteries, capacitors, and fuel cells. A comparison of these systems in terms of specific energy and specific power is shown in Fig. 1. Fuel cells are considered as good options for high energy applications due to their high specific energy which is defined as the total energy in the system normalized by the total weight. At the other end, capacitors are commonly used in high power systems but rarely used for large energy storage. Batteries fit into the intermediate space meaning a balance between specific energy and specific power. The high power and high energy of internal combustion engine can be achieved through a combination of electrochemical systems. For example, a combination of capacitors and

fuel cells would provide high power from the capacitor part and high energy from fuel cell part.

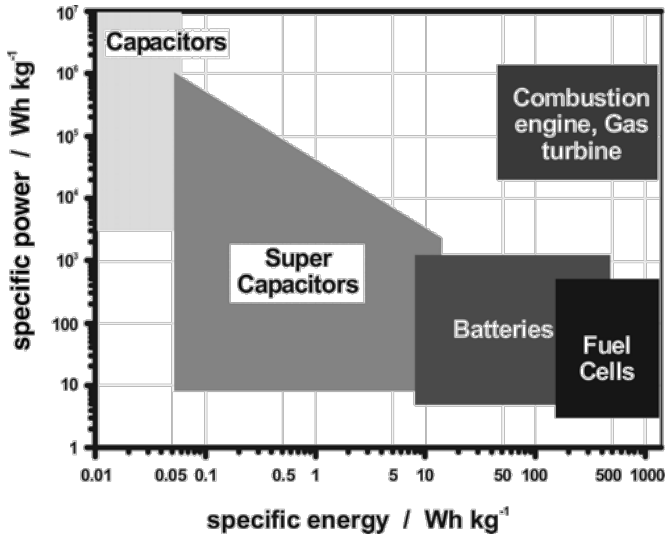

Figure 1 Ragone plot of the energy storage domains for the various electrochemical energy systems compared to an internal combustion engine. Reprinted with permission from 1.

1.2 Fuel cell systems

Fuel cells are electrochemical devices that convert chemical energy into electrical energy through electrochemical reactions. Their high efficiency and low emission with their modular and distributed nature and zero noise pollution make them very attractive for the next generation energy conversion systems. The physical structure of a fuel cell consists of an electrolyte layer in contact with an anode and a cathode on either side. The charged particles or ions move through the electrolyte which is an electronic insulator. The electrons move through the external circuit to establish a complete circuit. Catalysts are commonly used at the electrodes to accelerate the reactions. At the anode, the fuel is oxidized with the assist of catalysts, generating positively charged ions or cations and

electrons. At the cathode side, the chemical, usually oxygen, accepts the electrons and cations transferred from the anode and produces water (if hydrogen is the fuel) and/or carbon dioxide (if hydrocarbon is the fuel).

There are various types of fuel cells: metal hydride fuel cell, electro-galvanic fuel cell, direct formic acid fuel cell, microbial fuel cell, upflow microbial fuel cell, regenerative fuel cell, direct borohydride fuel cell, alkaline fuel cell, direct methanol fuel cell, reformed methanol fuel cell, direct ethanol fuel cell, proton exchange membrane fuel cell, phosphoric acid fuel cell, solid acid fuel cell, molten carbonate fuel cell, tubular solid oxide fuel cell, protonic ceramic fuel cell, direct carbon fuel cell, planar solid oxide fuel. Though they have different names, the working principles are the same with the major difference being the reactants at the anode and cathode.

The performance of fuel cells is normally characterized and represented by the polarization curve which shows the fuel cell voltage against the current density (current divided by the area of electrode). Fig. 2 displays a typical polarization curve of PEM fuel cell. The reversible standard potential is calculated based on the Nernst equation, which is higher than the actual operating cell voltage. There are three types of voltage loss or polarizations, dominating at different regions. Activation polarization appears at high voltage region, which is strongly affected by the reaction rate. Ohmic polarization shows at the intermediate voltage region, dominated by Ohmic resistance. Concentration polarization displays at the high current density and low voltage region, whose loss is substantially depended on the gas transport. Depending on applications, the fuel cell is evaluated at specific region.

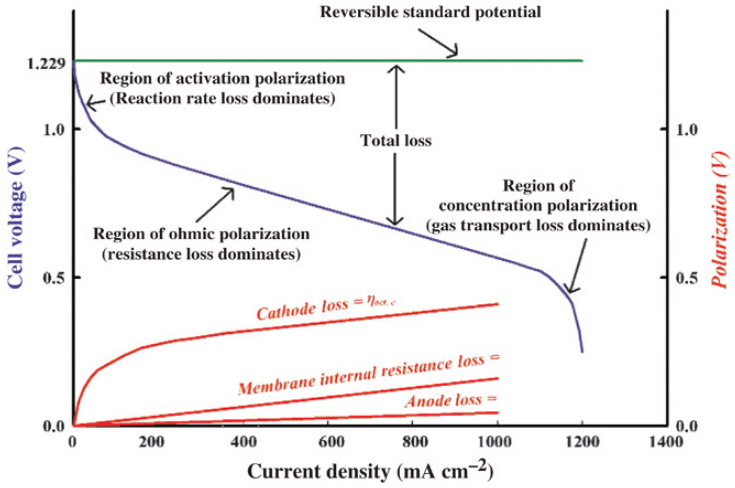

Figure 2 Polarization curve of PEM fuel cell. Reprinted from 2.

1.2.1 PEM fuel cells

The PEM fuel cell is arguably the frontrunner in the hydrogen economy and fuel cell race shown in Fig. 3. The anode and cathode are separated by a proton-conducting polymer membrane, e.g. Nafion, soaked with electrolyte. At the anode side, the hydrogen fuel is oxidized through the reaction:

$$H_2 \rightarrow 2H^+ + 2e^-.$$

The generated protons and electrons will travel through internal PEM and external circuit, respectively, to the cathode side where the ORR takes place as:

$$\frac{1}{2}O_2 + 2H^+ + 2e^- \rightarrow 2OH^-.$$

The only reaction product is water, so it is regard as a zero-carbon emission system. Notwithstanding the excellent perspectives of hydrogen economy and electrochemical energy conversion, the demands on materials and process optimizations in PEM fuel cells are formidable considering the sustained performance under widely varying operating

conditions, the lifespan, and the materials costs in view of commercialization. Though tremendous recent progress has been made in recently years, a critical performance limitation in PEM fuel cells centers on the cathode catalyst layer owing to the sluggish kinetics of the oxygen reduction reaction (ORR) and several mass transport losses.[3] Platinum (Pt) and Pt-based materials are commonly selected as the cathode catalyst due to their high catalytic activity. However, they would also lead to a high fuel cell cost as well as a durability concern in terms of Pt cathode oxidation, catalyst migration, loss of electrode active surface area, and corrosion of the carbon support.[4]

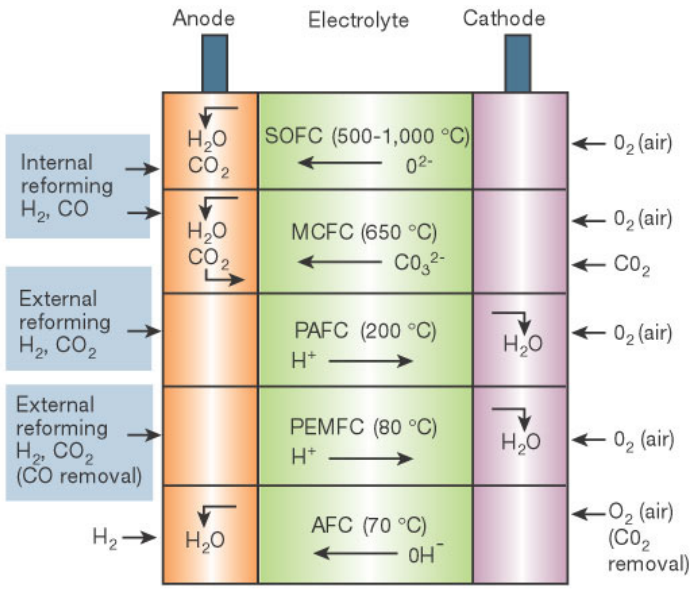

Figure 3 Summary of different fuel cell systems. Reprinted with permission from 5.

Although substantial theoretical and experimental research has been conducted in recent years for enhancing the overall performance of PEM fuel cells, the catalyst layer remains least understood part owing to its inherent complex structure and underlying multi-physical transport mechanisms. On the other hand, the three-decade long search for

non-precious metal catalysts for the ORR so far returned very few materials with promising activity and performance stability, especially in acidic environment.

Over the last decade, enormous research effort and resources have been devoted to overcoming several challenges in the development of PEM fuel cells for automotive propulsion. The main challenge toward realizing commercially viable PEM fuel cells was realized on the design and development of cheap and stable catalysts for the ORR and the low-cost manufacturing process of innovative electrode architectures. The ORR catalyst used in current PEM fuel cells is platinum nanoparticles mixed with carbon black (Pt/C), but cost and supply constraints for large-scale adoption in automotive propulsion require a factor of >4 increase in catalytic activity per mass of precious metal.[6] In this context, the Pt-utilization target for 2015, as defined by the U.S. Department of Energy, is 0.2 g of Pt per kW at 55% efficiency for a transportation PEM fuel cell stack.[7, 8] Based on this target and under the assumption that all cars in the future would be powered by the PEM fuel cell, a global annual production of 100 million PEM fuel cell cars rated at 50 kW each would require a steady Pt demand of 1,000 tons a year. In recent years, the global Pt production has only been *ca.* 200 tons a year, while the total world Pt reserves are estimated at 40,000 tons.[7, 8] Based on these estimations, in order to maintain a sustainable PEM fuel cell based vehicle fleet, the Pt cost would likely rise significantly. One such forecast estimates that the Pt catalyst alone would account for 38–56% of the stack cost assuming a low Pt price of $1,100 per troy ounce and a relatively low production volume of 500,000 PEM fuel cell stacks a year.[7, 8] Therefore, replacing platinum-based catalysts

with a more abundant material would greatly improve the outlook for the widespread development of automotive fuel cells.

Non-precious metal catalysts using abundant transition metals have long been explored and utilized.[7] However, their viability relies on how close the electrochemical performance can be compared to that of traditional, but more expensive Pt/C catalysts. Most current work on non-precious metal based ORR catalysts focused on the microstructure with nitrogen-coordinated iron in a carbon matrix, though the nature of active sites remains elusive. Numerous synthesis methods have been developed but their final products showed virtually identical catalytic activities and the corresponding PEM fuel cell performance continued to remain inferior to that loaded with Pt/C catalysts.[7] Not until the most recent years, promising advancements has been made in high-performance non-precious metal catalysts and electrode development, which may be mark as the dawn of a turning point.[4, 9-11]

In order to accelerate the PEM fuel cell technology development and near-term market entry with particular focus on automotive applications, it is imperative to develop high performance electrodes with higher power density and lower cost. In this regard, a two-pronged research approach is warranted, which involves: (1) development of low-cost and less complicated manufacturing process for novel electrode architectures using non-precious metal electrocatalysts with improved performance and durability; and (2) gaining fundamental insight into complex structure-transport-performance interactions within the electrode.

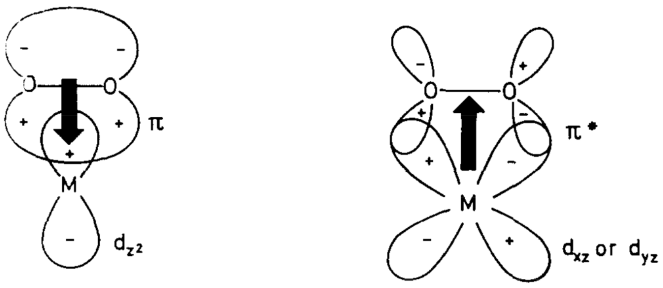

Figure 4 Schematic explanation of oxygen adsorption on a transition metal (a), and oxygen reduction by transferring electrons from the metal electrode to oxygen. Reprinted with permission from 12.

Transition metals including Fe and Co are excellent candidates, due to their good reactivity and multiple valence states. The transition metals have good catalytic reactions, as schematically shown in Fig. 4. When oxygen is adsorbed on the transition metals, electrons are transferred from oxygen to the empty d_{z^2} orbitals of the transition metals, forming a δ bond (Fig. 4 left). When electrons are transferred to cathodes during the fuel cell operation, electrons are donated to the anti-bonding π orbitals of oxygen (Fig. 4 right), weakening oxygen-metal bonding and thereby increasing oxygen reactivity with proton (i.e., resulting in H_2O).[13] Despite the good oxygen reduction, the transition metals are easily oxidized in O_2 environment. The metal oxides are electrical insulators, prohibiting further charge transfer. Moreover, oxygen molecules hardly adsorbs on the surface of the oxides.[14]

The fast degradation of catalytic activities from the transition metals have been somewhat suppressed by surrounding the metal with organic molecules. Jasinski et al. reported for macrocyclic structure containing nitrogen-metal coordination as decent oxygen reduction reaction catalysts. Several non-noble transition metals such as Co, Fe,

and Mn have been studied in the form of cobalt (II) tetramethoxy-phenylporphyrin ($Co^{II}TMPP$) and iron (II) phthalocyanine ($Fe^{II}PhC$) (Fig. 5) for ORR. Good oxygen reduction activities from the metal macrocycles are achieved,[15] but macrocycles still have poor stability. Therefore, additional heat treatment at high temperatures (above 1000 °C) were often performed to improve the durability by making stable protective graphitic layers.[16, 17]

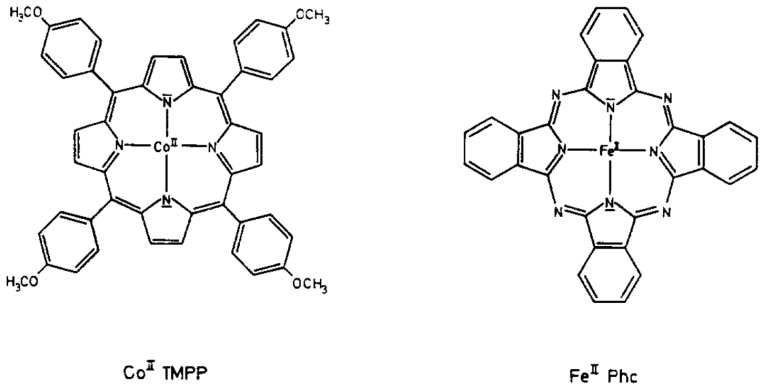

Figure 5 $Co^{II}TMPP$ and $Fe^{II}Phc$. Reprinted with permission from 12.

A recent report has demonstrated that heating precursors containing nitrogen, carbon, and transition metals (e.g., Fe, Co) have shown excellent stability and high oxygen reduction reaction activity.[11] They showed that heat treated graphitic layers are excellent to protect Co/Fe catalysts, exhibiting great performance without Pt catalysts (Fig. 6). However, it requires complicated multi-step processing including aniline mixing, polymerization, heat treatment, acid leaching, and another heat treatment, as shown in Fig. 6. They also used large amount of carbon particles as a support, which limit the amount catalysts embedded in the cathodes.

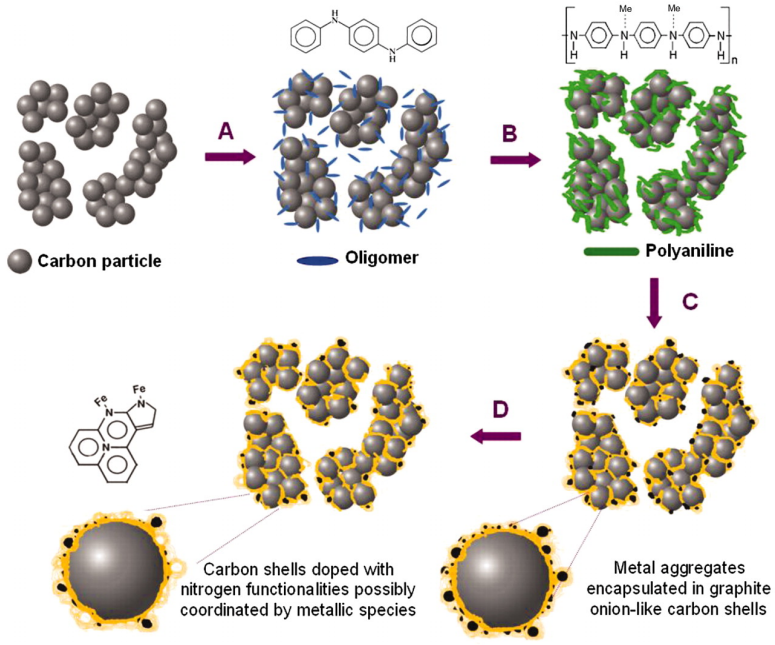

Figure 6 Schematic diagram of the synthesis of PANI-M-C catalysts. (A) Mixing of high–surface area carbon with aniline oligomers and transition-metal precursor (M: Fe and/or Co). (B) Oxidative polymerization of aniline by addition of APS. (C) First heat treatment in N_2 atmosphere. (D) Acid leaching. Reprinted with permission from 11.

The findings from the past intense research indicate that it is feasible to use non-precious metal catalysts when they are encapsulated by graphitic layers. My research is focusing on utilize the findings, but employ a one-step facile manufacturing process, with increased reactivity with nanometer scale catalysts and less inactive materials by removing a large amount of carbon supports (e.g. carbon black).

1.2.2 Microbial fuel cells (MFC)

MFCs are "green energy" devices utilizing microbial metabolism to directly generate electricity from organic substrates, and have generated excitement in environmental and bioenergy communities due to their potential for coupling wastewater treatment with energy generation[18-20]. It has been studies for years that electricity can be

generated through bacteria. For example, some iron-reducing bacteria, such as Shewanella putrefacians and Geobacter metallireducens, can be used to make electricity because they reduce Fe(III) to Fe(II). However, it requires expensive and toxic chemicals to extract electrons from the bacteria to the electrode. In addition, purified chemicals (such as glucose) are necessary for the bacteria to grow on. A typical construction of MFC is demonstrated in Fig. 7. It consists of an anode chamber, a cathode chamber, and a PEM that separates the two chambers. Electrons and protons are generated in the anode chamber, different from PEM fuel cells, through microbial metabolism. The electrons are transferred from the microbe to the anode through direct contact and/or soluble mediators, and then reach the cathode through an external electric circuit.[21] The protons are transported through the PEM into the cathode chamber. When oxygen or other electron acceptors (e.g. ferricyanide) are present in the cathode chamber, protons will combine with electrons and electron acceptors at the cathode to form water as a final product and, therefore, electricity is generated.

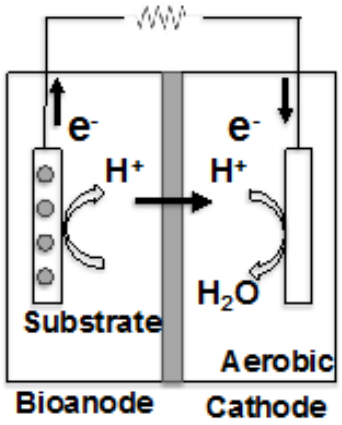

Figure 7 A schematic of microbial fuel cell.

Compare to the PEM fuel cell, the performance of MFC is strongly depended on the electron transfer from the electrochemically active microbes to the anode. Unfortunately, the efficiency of this process is not high enough to make the MFC technology commercially viable. A lot of effort has been paid to improve the performance of anode materials aside from exploring new route to lowering the cost of MFCs.[22] The key activity occurring at anode-microbe interfaces is electron generation by metabolically and electrochemically active microorganisms as well as transfer of the generated electrons to anode surface through a combination of direct contact, microbial pili (or nanowires), and mediators.[23-26] Regardless of the electron transfer route, large electrode surface areas would promote interactions between microbes and the anode. It would also result in a better electron transfer while minimizing the internal electrical resistance.

A common electrode material for MFCs is carbon based materials such as carbon cloth and carbon felt due to their relatively low cost and biocompatibility.[27] Three-dimensional (3D) carbon fiber non-woven electrodes prepared by electrospinning and solution blowing techniques have shown to provide high current densities.[28] Carbon brush electrodes have been also used since their 3D structure provides large surface area for microbial attachment. These conventional electrodes, however, have significantly less surface area than nanomaterial-based electrodes, since nanomaterials have exceptionally large surface-to-volume ratios. Their unique electrochemical properties such as strong charge interactions with organic matter would contribute to a closer bonding as well. Recently, various nanomaterials such as metal nanoparticles,[29] carbon nanotubes (CNTs),[30-35] and CNT composites[36, 37] have been used as additives for conventional MFC

electrodes. For example, multi-wall CNTs were attached to carbon cloth, papers, or textiles to increase the electrical conductivity and surface area of electrodes, resulting in 20~150% enhancement in power densities.[30, 33, 35] The observed improvements were thought to arise from the better interaction between electrochemically active microbes and the electrode mainly due to improved electrical conductivity and increased surface areas.[30, 33, 35] Nevertheless, the influence of the nanomaterials on the power output of MFCs had not been systematically studied, and hence, design principles for developing next-generation nanofabricated electrodes remain elusive.

1.3 Battery systems

A battery system is formed by connecting a number of electrochemical cells in a way that the whole system provides enough power and energy for specific applications. For each cell, there is a cathode and an anode, which are internal connected by electrolyte containing dissolved salts. The anode and cathode are connected externally where electron transfer is occurred instead of ion moving inside the cell. When the cell is discharging, anode would go through oxidation reaction and the generated electrons and ions would move to the cathode through external and internal circuit, respectively. While at the cathode side, reduction reaction would happen by accepting the transferred electrons from the anode. During charging, this process is reversed. The standard cell voltage can be calculated by:

$$E^o = -\frac{\Delta G^o}{nF}$$

where ΔG^o is the change of Gibbs free energy of the total cell reaction ($A + B \rightarrow A^{n+} + B^{n-}$) under standard conditions (25 °C and unit activity of each reactant and product). n

is the number of electrons involved in the reaction. F is the Faraday constant. If the cell is not working under standard conditions, the corresponding cell voltage can be calculated as:

$$E = E^o - \frac{RT}{nF} \ln \frac{a_{A^{n+}} a_{B^{n-}}}{a_A a_B}$$

where $a_{A^{n+}}$ and $a_{B^{n-}}$ are the activity of products. a_A and a_B are activity of reactants. R is the Boltzmann constant and T is the absolute temperature.

There are many different types of battery systems have been developed and commercialized. Fig. 8 shows several widely deployed battery systems and compares them in terms of volume (Wh/L) and weight (Wh/kg) based energy density. Among them, LIBs outperform other systems, explaining their largest market share.[38]

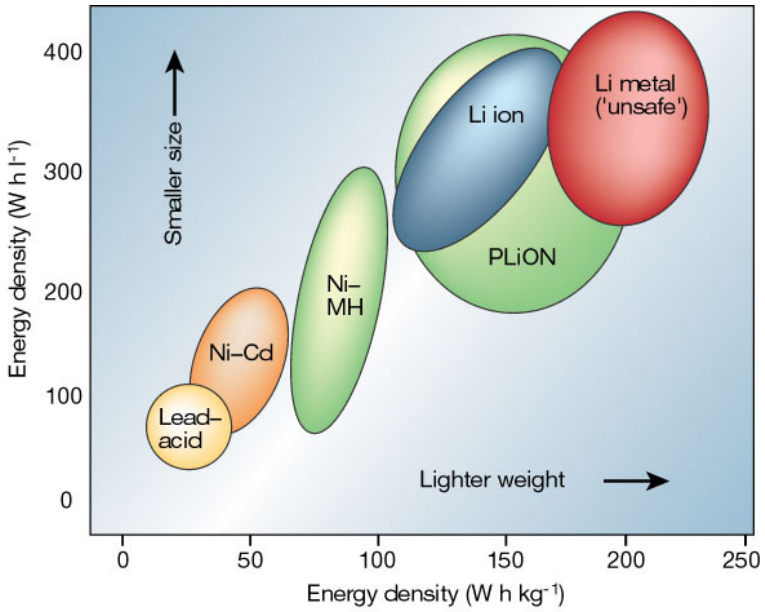

Figure 8 Comparison of the different battery technologies in terms of volumetric and gravimetric energy density. Reprinted with permission from 39.

1.3.1 Li-ion batteries (LIBs)

The initial research on LIBs starts from 1970s, when Exxon was investigating a battery system with TiS_2 as cathode, Li metal as anode, and $LiClO_4$ dissolved in dioxolane as electrolyte. However, the problem of lithium dendrite (Fig. 9a) formed after cycling on the anode put the safety in question, limiting the practical application. To overcome this issue, several methods have been proposed with the best result showing on using layered carbonaceous material through the intercalation mechanism (Fig. 9b). At the same time, cathode materials changed from chalcogenides to metal oxides and finally to Li_xMO_2, where M is Co, Ni, or Mn).[40, 41] The first commercialized LIB comes from Sony Corporation in 1991 with a graphite anode and a $LiCoO_2$ cathode, which opens the door for efficient energy storage in portable electronics.

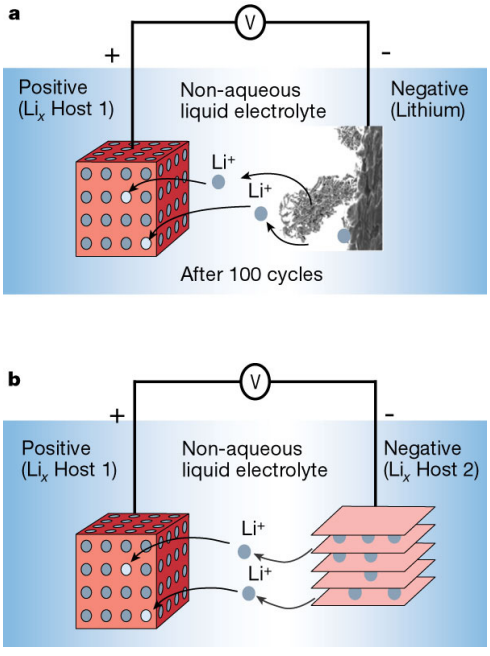

Figure 9 Schematic representation and operating principles of Li batteries. Reprinted with permission from 39.

1.3.2 Lithium-sulfur batteries

Although LIBs are currently the most promising energy storage devices, they gradually seem to hardly meet the high demand from the market for high energy storage. First, they are too expensive to be used for large-scale energy storage (e.g., wind and solar systems). Second, they have relatively small energy capacity and short cycling life compared to recently developed battery systems.[42]

Li-S batteries have been regarded as promising alternatives to LIBs due to their high theoretical energy density (2600 Wh/kg) which is at least five times higher than that of LIBs with $LiCoO_2$/graphite chemistry (387 Wh/kg). Though first reported in the 1960s, Li-S batteries didn't attract as much attention as their counterparts LIBs due to the poor cycling performance. The research on Li-S batteries soar after 2009 when Nazar's group published the pioneered work on Li-S batteries with substantially improved performance.[43] A typical Li-S battery has a lithium anode, a sulfur cathode, and an electrolyte in between (Fig. 10).

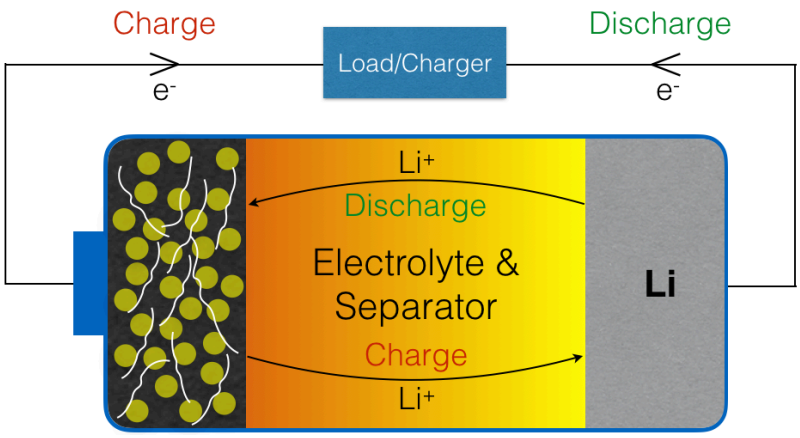

Figure 10 A schematic of Li-S battery.

When discharging, lithium anode would loss electrons and form lithium ions ($2Li \rightarrow 2Li^+ + 2e^-$), and sulfur cathode would be reduced to form Li_2S by combining the lithium ions from the anode side ($S + 2Li^+ + 2e^- \rightarrow Li_2S$). The open circuit voltage (OCV) can be calculated by using the electrochemical potential of lithium (μ_a) and sulfur (μ_c). This is shown in Fig. 11a. The voltage profile of a typical discharge process is shown in Fig. 11b, ending with increased cathode electrochemical potential. During this process, there are many intermediate products generated, which is commonly called polysulfide (Li_2S_x, x=2~8). At the beginning (Fig. 11b, region II), sulfur would be reduced to Li2S4 in a stepwise manner through Li_2S_8 and then Li_2S_6, corresponding to a 2.3 V voltage plateau. In region II, Li_2S_4 is converted to Li_2S_2 with a discharging voltage plateau at 2.1 V. The final stage is a sloped voltage profile related to the reaction from Li_2S_2 to Li_2S. When the charging process starts, Li_2S would be oxidized to high order of polysulfide in the region II', followed by the final return to sulfur from polysulfide (Fig. 11c). Therefore both the charge and the discharge processes are multi-steps, which can be clearly observed on the CV test (Fig. 11d). A plateau in the charge/discharge profile is represented by a peak in the CV plot. The total cell reaction features a two-electron reaction, compared to the one-electron reaction for LIBs. Though the working potential of Li-S batteries (2.1 V) is lower than that of LIBs (3.7 V), the high energy of Li-S batteries is a result of their large capacity. Lithium has a theoretical specific capacity of 3860 mAh/g, while the number of sulfur is 1672 mAh/g.

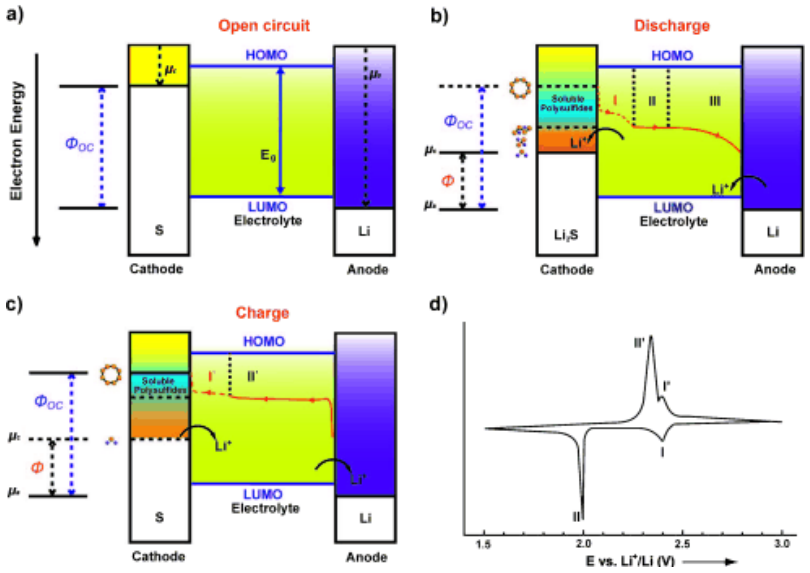

Figure 11 Electrochemistry of the Li-S battery at different stage: (a) open circuit; (b) discharge process; (c) charge process. (d) Typical cyclic voltammogram (CV) for an S cathode in a Li-S battery. Reprinted with permission from 44.

Nonetheless, there are problems are associated with Li-S batteries, limiting their wide applications. From the cathode side, there are mainly three problems:

(1) large charge transfer impedance;

This is caused by the poor conductivity of the end products at the charged (sulfur) and discharged (Li_2S_2 and Li_2S) state. Large polarization would occur at the end of discharge and charge, limiting the available capacity delivered by the system. To solve this problem, a large amount of conducting additives are required to promote the electron transfer at the interface. It has been proven to be an effective way, but the additives would occupy a large portion of total volume and weight. The benefit brought by the conducting additives should be weighed against the decreased volumetric and gravimetric energy density.

(2) polysulfide shuttle;

In the process of discharge, stepwise formed polysulfides (Li_2S_8, Li_2S_6, Li_2S_4) are soluble in the ether-based electrolyte. Due to the concentration gradient, the formed polysulfides would diffuse from cathode to anode, where they tend to be reduced to the lower order Li/S compounds and deposit on the anode surface. These reduction byproducts will be harmful to form a stable solid electrolyte interphase (SEI), which is important for stable cycling. Also, it will lead to the irreversible loss of cathode active material, decreasing the capacity.

(3) large volume change;

The density of sulfur is 2.07 g/cm^3 larger than that of Li_2S (1.66 g/cm^3), meaning a large volume expansion would happen during the discharge process. The volume change can be as large as ~80%, which is very likely giving rise to the pulverization of electrode materials. Once the particles are lost from the electrode due to pulverization, they will lose electrical contact with the electrode and become inactive. Then the loss of viable capacity can be expected.

From the anode side, metallic lithium also raises three problems:

(1) reactive with electrolyte;

Lithium is a strong reductive metal with a standard reduction potential of -3.04 V vs. SHE. The Fermi level of Li is sitting outside the operating window (between HOMO and LOMO) of most electrolytes. Therefore it will react with the electrolyte and form a SEI, leading to an irreversible capacity fading and low Coulombic efficiency.

(2) lithium dendrite formation;

During the charging process, lithium ions tend to be reduced and deposit on the metal surface of lithium. A uniform deposition of lithium is ideal, but in reality it is rarely observed. Instead, local current density variation would cause uneven distribution of lithium ions on the surface. This is the well-known lithium dendrite, which may poke through the separator as the cycling goes on. The big safety issue of internal short-circuit has been realized in using lithium metal as anode.

(3) poor SEI;

As stated previously, polysulfides can be reduced by lithium to form SEI on the anode surface. It has been studied that the SEI formed by the products of lithium-polysulfides reaction have poor stability during cycling. The unstable SEI is going to consistently consume electrochemically active materials, resulting in low Coulombic efficiency and poor cycling performance.

CHAPTER II

SCALABLE SYNTHESIS OF BI-FUNCTIONAL HIGH-PERFORMANCE CARBON NANOTUBE SPONGE CATALYSTS AND ELECTRODES WITH OPTIMUM C-N-FE COORDINATION FOR OXYGEN REDUCTION REACTION*

2.1 Introduction

ORR is the main cathode reaction in a variety of electrochemical systems such as fuel cells and metal-air batteries. However, without catalysts, the ORR is slow in kinetics due to the strong O=O bond and the three-phase (gas-phase O_2; liquid-phase electrolyte; solid-phase electrode) reaction. Among various catalysts, platinum-based catalysts have been acknowledged as the best in terms of low overpotential and long-term stability, but the excellent performance unfortunately accompanies with the high price, prohibiting a wide deployment of environmentally friendly fuel cell technologies. Intense search for alternatives over the past decades has recently resulted in several new kinds of materials including metal-nitrogen complexes on carbon matrices[4, 45], metal chalcogenides[46, 47], perovskites[48], spinel oxides[49], and doped carbonaceous materials[50-53]. Among the various catalysts, recently reported nitrogen-doped carbonaceous materials with transition metals[11, 54, 55] have shown the best performance, but these catalysts still suffered from metal leaching, anion bonding to active sites, or protonation of nitrogen in harsh acidic environments (*e.g.*, 0.5M H_2SO_4)[56, 57].

---

* Reprinted from G. Yang, W. Choi, X. Pu and C. Yu, *Energy & Environmental Science*, 2015, **8**, 1799-1807.

The exact functions of the transition metals in nitrogen-doped carbonaceous materials are still under debate. Two main arguments are considered to be most probable. First, transition metals play a role in the oxygen reduction reaction either by assisting the adsorption of oxygen or electron transfer from the electrode to oxygen[4, 58]. Second, transition metals neither participate the catalytic reaction nor become part of catalytically active sites, but they assist the formation of nitrogen-doped carbon nanostructures during nitrogen incorporation processes[59]. Here, we designed a series of carbon-based catalysts containing differently coordinated nitrogen with/without incorporation of iron or iron compounds so as to divulge their roles. This study led us to develop new nitrogen-doped CNT-based catalysts without precious metals, exhibiting outstanding catalytic activity and long-term stability, which are comparable to those of commercial platinum-carbon (Pt/C) catalyst in both acidic (0.5M H_2SO_4) and alkaline (0.1M KOH) environments. The self-standing porous 3D structures of our catalysts can potentially eliminate gas diffusion and catalyst support layers such as carbon papers or carbon cloth in various electrochemical cells. The following describe synthesis procedures and their ORR characteristics in both acidic and basic environment along with their structural and compositional information.

2.2 Experimental

2.2.1 Synthesis of the 3D CNT sponge

"Fe-CNT" samples were synthesized by a chemical vapor deposition (CVD) method in a three-zone furnace. An alumina crucible filled with ~0.3-g ferrocene (Sigma-Aldrich, 98%) was placed in zone 1 (upstream) of a quartz tube whose inner diameter is ~22 mm. During the growth, hydrogen (Airgas, 99.999%), ethylene (Airgas, 99.999%),

and argon (Airgas, 99.999%) gases were flowed into the tube at flow rates of 260 sccm, 80 sccm, and 80 sccm, respectively. The argon gas was passed through a bubbler filled with deionized (DI) water at room temperature. The furnace temperatures of zone 1, zone 2 and zone 3 (CNT growth zone) were 120 ^{o}C, 120 ^{o}C, and 650 ^{o}C, respectively. The typical growth time was 30 min to obtain a 100-mm long sponge shown in Fig. 12a. After the CVD reaction, the furnace was naturally cooled under 200-sccm argon flow. "CNT" samples were prepared by immersing Fe-CNT sample in 0.5M H_2SO_4 for 24 hr at room temperature, and then washed with enough DI water followed by a vacuum (120 mTorr) drying at 80 ^{o}C. "Fe-CNT-ox" samples were prepared by annealing Fe-CNT under air at 400 °C for 5 h.

2.2.2 Nitrogen doping processes

To obtain Fe-CNT-PA samples, as-synthesized Fe-CNT samples were first treated with a mixture of H_2SO_4 and HNO_3 for 5h and then rinsed with enough DI water followed by natural air drying at room temperature. Then 0.02-g Fe-CNT sample was immersed in a solution containing 5-mL 0.5M HCl (Macro Fine Chemicals) and 0.1-mL aniline (Alfar Aesar, 99+%), and the solution was sonicated for 30 min. For polymerization of aniline, ammonium peroxydisulfate (0.31 g) and iron chloride (0.0148 g) were added to the solution, and left at temperatures below 5 ^{o}C for 24 h. The samples were dried under vacuum (120 mTorr) at 80 ^{o}C and then heat-treated under 200-sccm argon flow at 900 °C for 4 h. To obtain CNT-PA samples, the same nitrogen doping processes for Fe-CNT-PA was carried out except the polymerization process where iron chloride was not added. For Fe-CNT-Py samples, right after growing Fe-CNT samples, the furnace temperature was

increased to 800 °C. Then pyridine (Alfa Aesar, 99+%) was introduced to the furnace tube by a syringe pump (Model KDS-100, KD Scientific) at a feeding rate of 20 mL/h under 2000-sccm argon and 100-sccm hydrogen for 30 min.

2.2.3 Sample preparation for electrochemical testing

Samples were made into ink to test their electrocatalytic activities except Fe-CNT-PA 3D. To make homogeneous ink, 7-mg sample and 160-μL 5-wt% Nafion solution (Fuel Cell Earth) were dispersed in a mixture of DI water (670 μL) and ethanol (170 μL, EMD Millipore, 92%-94%) by sonication for 0.5 hr. CV and RDE tests were carried out using an electrochemical workstation (CHI 604D, CH Instrument) in a three-electrode system with Ag/AgCl as a reference electrode, and a platinum wire as a counter electrode at room temperature. The working electrode was prepared by loading 5 μL of catalyst ink onto the glassy carbon electrode (3 mm in diameter), resulting in 0.5 mg/cm^2 catalyst loading. For comparison, 7-mg of commercial Pt/C (20-wt% Pt, Fuel Cell Earth) was made into ink with the same method as the Fe-CNT-PA ink. The working electrode was prepared by loading 5 μL of the Pt/C catalyst ink on the glassy carbon electrode, resulting in 0.5 mg/cm^2 (0.1 mg_{Pt}/cm^2) catalyst loading. For the testing with the 3D structure (denoted as Fe-CNT-PA 3D), Fe-CNT-PA (0.3 mg) was carefully cut to match the area of glassy carbon electrode and then attached to the glassy carbon electrode by using carbon paint. Fe-CNT-PA 2D was prepared by dropping the Fe-CNT-PA ink (5 μL) and then drying 8 times followed by another 2.4 μL on the electrode to make the loading mass of Fe-CNT-PA 3D and Fe-CNT-PA 2D the same.

2.2.4 Electrochemical measurements

For O_2 (or N_2) saturated measurements, the electrolyte (200-mL of 0.5M H_2SO_4 or 0.1M KOH) was purged with 100-sccm O_2 (or N_2) for longer than 15 min (or 30 min) before the test, and O_2 (or N_2) was continuously fed to the system to maintain O_2 (or N_2) saturation during the electrochemical tests. The scan rates used for all CV and RDE tests were 100 m V/s and 5 mV/s, respectively. The electrode was rotated at 1600 rpm for the RDE tests. The Koutecky-Levich plots were obtained by $J^{-1} = J_K^{-1} + B^{-1}\omega^{-1/2}$ and $B = 0.62nFCD^{2/3}\nu^{-1/6}$, where J_K^{-1} is kinetic limiting current density, ω is the rotational speed, n is the number of electron transferred, F is the Faraday constant (F = 96485 C/mol), C is the bulk concentration of O_2 (C=1.2×10^{-6} mol/cm^3 for 0.1M KOH; C = 1.1×10^{-6} mol/cm^3 for 0.5M H_2SO_4), D is the diffusion coefficient of O_2 in 0.1M KOH (D=1.9×10^{-5} cm^2/s for 0.1M KOH; D=1.8×10^{-5} cm^2/s for 0.5M H_2SO_4), and ν is the kinematic viscosity of the electrolyte (ν=0.01 cm^2/s for both 0.1M KOH and 0.5M H_2SO_4).

2.2.5 Material characterization

XRD (Bruker-AXS D8 VARIO) measurements were performed with Cu Kα radiation from 2θ=15° to 75° with a step size of 0.01° and dwell time of 0.1 s. SEM images were collected with JEOL JSM-7500F and TEM images were obtained with JEOL JEM-2010 TEM and FEI TECNAI G2 F20 FE-TEM. Raman (Horiba Jobin-Yvon LabRam) spectra were recorded with 632.8 nm excitation wavelength at room temperature with a maximum laser power of 4.0 mW in order to avoid sample heating. TGA (Q600-TGA, TA Instruments) experiments were carried out with ~10-mg samples in alumina pans were heated from room temperature to 800 °C at a rate of 10 °C/min in air (100 mL/min). XPS

(Kratos Axis Ultra DLD) survey scans were collected with 1.0 eV resolution followed by high-resolution scans of Fe 2p, C 1s, N 1s, O 1s, and S 2p with 0.05 eV resolution.

2.3 Results and discussions

2.3.1 Growth of CNT sponge and nitrogen incorporated CNT sponge

The base material of our samples has sponge-like porous structures with randomly oriented and entangled CNTs. As shown in Fig. 12a and Fig. 13a,b, the sponge replicated the cylinder shape of the quartz tube whose inner diameter is ~22 mm. The sponge length was controlled by reaction time, and ~30 min reaction yielded ~100-mm long cylindrical sponge. The as-formed CNT sponge is deformable to a large extent without any fracture (Fig. 12b), which can be attributed to the unique framework made of loosely packed and entangled CNTs. In comparison to previously reported methods of synthesizing bulk CNT structures[60-65], our method features a remarkably improved production rate (~3.6 g/h or 76 cm^3/h compared with ~0.018 g/h or 9.6 cm^3/h in literature), considerably reduced material costs (~\$0.1/g_{cnt} compared with ~\$85.2/g_{cnt} in literature: see details in Table 1), and simplified processes that do not require precursor solutions and liquid feeding systems.

The suggested growth reaction is illustrated in Fig. 12c. At the beginning, ferrocene was decomposed at temperatures above 400 °C[66] forming iron nanoparticles on the wall of a quartz tube, which serve as catalysts for growing CNTs with carbon-containing ethylene gas. As ferrocene continuously delivered to the reaction zone, additional iron nanoparticles were attached to the wall of existing CNTs during the synthesis process. Meanwhile, ethylene gas was continuously conveyed to the reaction zone, promoting the growth of new CNTs from the iron nanoparticles on the wall of the

existing CNTs, and ultimately forming 3D sponge-like porous structures. The inside of a furnace tube after 10- and 30-min growth reactions (Fig. 12d) indicates that the growth occurs in the radial direction toward the center of the tube, supporting the suggested growth process.

The synthesis process of the as-synthesized sponge was varied to have a series of different samples so as to study the roles of iron and its compounds as well as the influence of the chemical environment of nitrogen on ORR. To find the role of iron for ORR, the as-synthesized sponge (labelled as "Fe-CNT") was washed with sulfuric acid to have iron deficient CNTs, which are labelled as "CNT". In order to investigate the role of iron in forming different nitrogen doping states, CNT sponges with iron and polyaniline (labelled as "Fe-CNT-PA") and CNT sponges with only polyaniline (labelled as "CNT-PA") were prepared by selectively adding iron source ($FeCl_3$) to "CNT" for Fe-CNT-PA during the nitrogen incorporation process. The iron contents in Fe-CNT-PA and CNT-PA were found to be 1.5 and 0.1 at% according to thermogravimetric analysis (TGA) (see Table 2 and Fig. 14). Fe-CNT was also annealed in air (labelled as "Fe-CNT-ox") to convert iron and iron compounds to iron oxides so as to investigate the effect of iron oxides on ORR. The influence of pyridinic/graphitic nitrogen as well as nitrogen concentration on ORR was also studied by using pyridine instead of polyaniline as a nitrogen source (labelled as "Fe-CNT-Py").

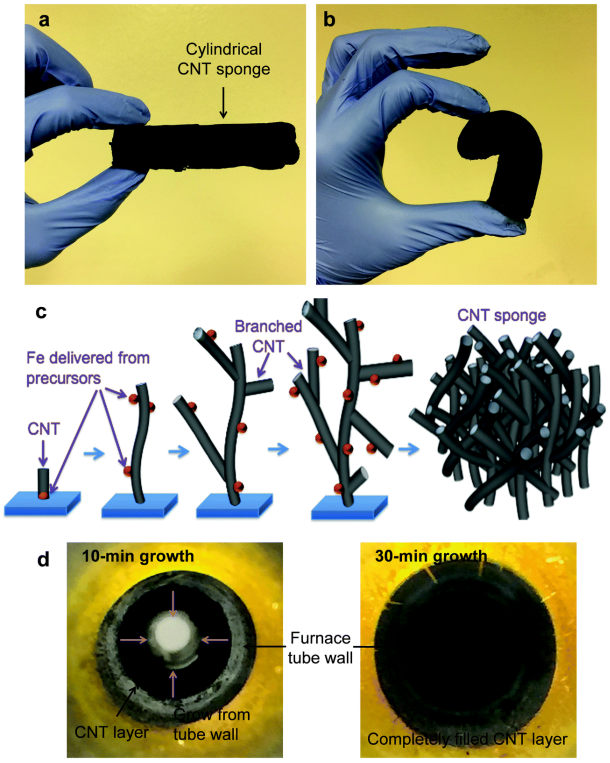

Figure 12 Sponge-like CNT framework: a, An as-synthesized cylindrical sponge-like CNT structure. b, A CNT sponge withstanding a large deformation without fracture. c, Time evolution of the proposed synthesis process of the porous CNT structure. d, Photos showing the inside of a furnace tube after 10-min (left) and 30-min (right) growth reaction.

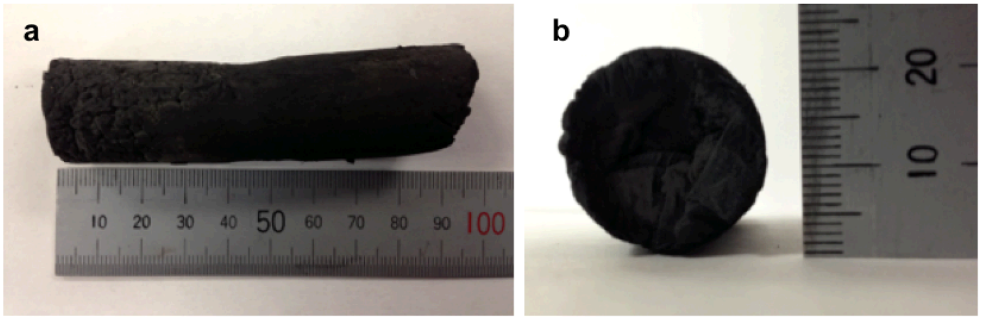

Figure 13 a,b Photos of an as-synthesized cylindrical CNT sponge.

Table 1 Cost analysis and comparison of CNT sponge synthesis methods.

	This work (30 min growth)		**Literature (240 min growth)**	
	Amount	Cost	Amount	Cost
Ferrocene, 98% ($108 for 500 g) *	0.3 g	$ 0.065	1.87 g (0.06 g/mL × 0.13 mL/min × 240 min)	$0.404
1,2-Dichlorobenzene, 99% ($169 for 2 L) *	-	-	31.2 mL (0.13 mL/min × 240 min)	$2.636
C_2H_4, UHP ($22 for/300 ft^3) **	2.4 L (80 sccm × 30 min)	$ 0.064	-	-
H_2, UHP ($45 for 300 ft^3) **	7.8 L (260 sccm × 30 min)	$ 0.041	72 L (300 sccm × 240 min)	$0.381
Ar, UHP ($48 for 300 ft^3) **	2.4 L (80 sccm × 30 min)	$ 0.014	480 L (2000 sccm × 240 min)	$2.712
Yield / Total cost	1.8 g 2.2 cm (diameter), 10 cm (length)	$ 0.184	0.072 g 4 cm (length), 3 cm (width), 0.8 cm (thickness)	$6.133
Production rate / Normalized cost	3.6 g/h 76 cm^3/h	$ 0.1/g	0.018 g/h 2.4 cm^3/h	$85.2/g

* Price information was obtained from Sigma-Aldrich website.

** Price information was quoted from Airgas.

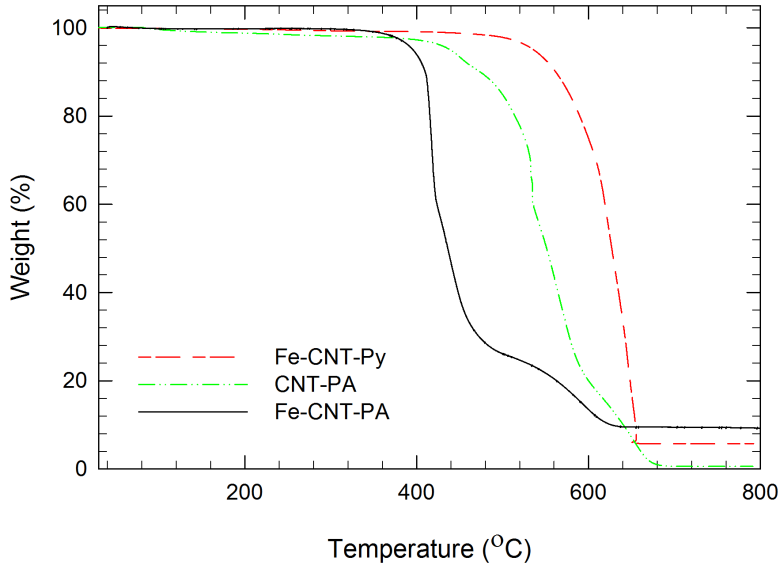

Figure 14 TGA results of Fe-CNT-Py (red), CNT-PA (green), and Fe-CNT-PA (black).

2.3.2 Microstructure of CNT sponge and nitrogen incorporated CNT sponge

A scanning electron microscope (SEM) image of Fe-CNT (Fig. 15a) displays porous CNT structures with nanoparticles attached to the stem of the CNTs, and their transmission electron microscope (TEM) images (Fig. 15b,c) indicate CNT walls are composed of multiple graphitic layers. The polyaniline coating for nitrogen doping (Fe-CNT-PA) created aggregates (Fig. 15d) and amorphous layer on the surface of CNT walls (Fig. 15e,f). The graphitic and continuous inner walls were preserved after the polymerization process of polyaniline, suggesting the presence of highly electrically conducting paths. The aggregates consisted of amorphous layers with nanoparticles (Fig. 16a) whose interlayer distance was calculated to be 0.67 nm corresponding to γ-Fe_2O_3 (102) (JCPDS 25-1402, 0.694 nm) (Fig. 16b). On the other hand, post doping with pyridine (Fe-CNT-Py) resulted in mainly graphitic CNT surface (Fig. 15g,h,i).

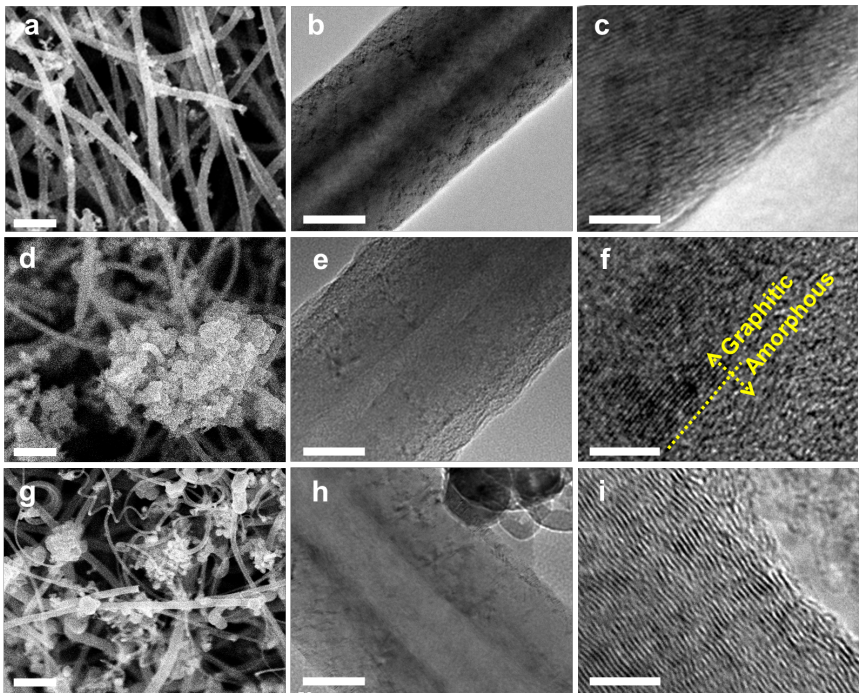

Figure 15 SEM and TEM images of CNT sponges. a,b,c, Fe-CNT. d,e,f, Fe-CNT-PA. g,h,i, Fe-CNT-Py. Fe-CNT and Fe-CNT-Py have all graphitic layers, showing the character of multi-wall CNTs whereas Fe-CNT-PA has amorphous layers on the graphitic wall of CNTs. The scale bars indicate 1 μm for the left column, 50 nm for the middle column, and 5 nm for the right column.

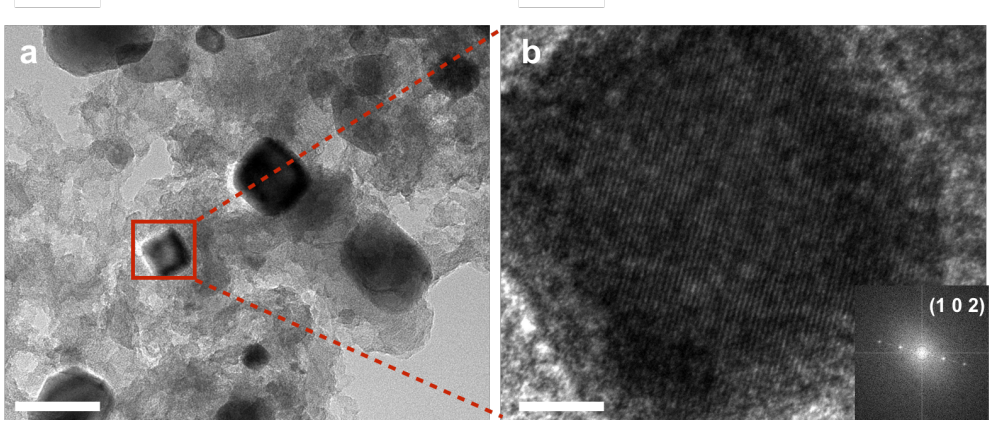

Figure 16 HRTEM images of the aggregated portion in Fe-CNT-PA (see Fig. 15d). The inset shows the fast Fourier transform pattern. The scale bars indicate 100 nm for a and 10 nm for b.

X-ray diffraction (XRD) indicates that Fe-CNT is likely to contain Fe_3C (four peaks between 2θ=43° and 46°), $Fe_{15.1}C$ (austenite), and Fe (Fig. 17a). The main carbon peak at 2θ=26.2° in XRD corresponds to the (002) layers of the concentric graphitic multi-walls, from which an interlayer distance can be calculated to be 0.34 nm (same as that from TEM) based on Bragg's law. The XRD peaks corresponding to Fe_3C, $Fe_{15.1}C$, and Fe were suppressed after the acid treatment (Fig. 17b). α-Fe_2O_3 peaks (JCPDS 33-0664) appeared after the annealing of Fe-CNT in air (oxidation) (Fig. 17c). For Fe-CNT-PA (Fig. 17d), it appears that the heat treatment process even under the environment with a low concentration of oxygen (99.999% Ar) turned the iron and iron compounds into γ-Fe_2O_3[67, 68]. The relatively small peak intensity from Fe-CNT-PA could be partly attributed to the amorphous polyaniline coating layer around CNTs (see Fig. 15e,f). The post doping process with pyridine in Fe-CNT-Py (Fig. 17e) resulted in the intensity increase of iron-carbon compounds, which may be ascribed to the introduction of additional carbon source from pyridine at high temperature (800 °C) resulting a higher crystallinity compared to Fe-CNT-PA. The nitrogen doping may have caused the higher intensity ratios of D-mode to G-mode (I_D/I_G) in the Raman spectroscopy, which indicates the defects or disorder in CNTs[69-71], as shown in Fig. 18.

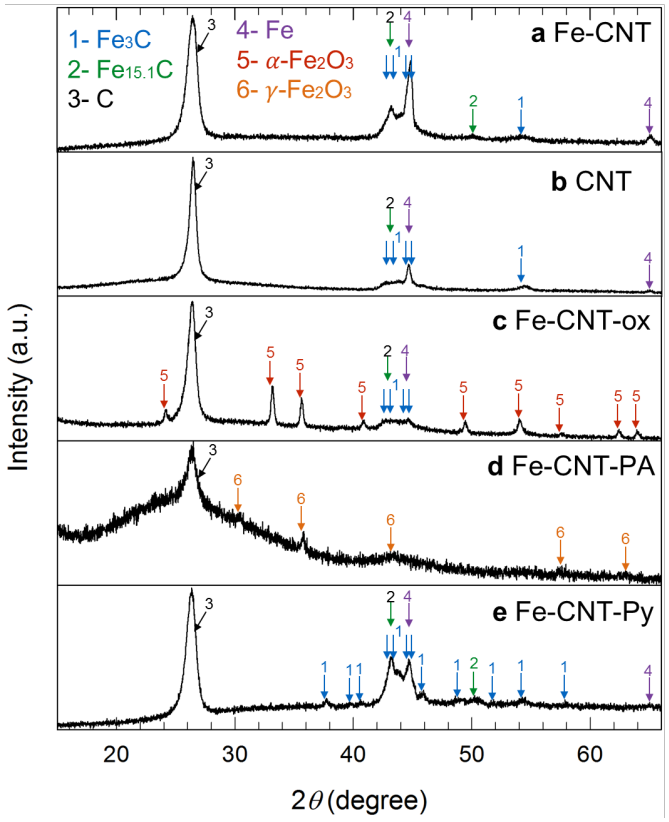

Figure 17 XRD results including the peak locations of Fe_3C, $Fe_{15.1}C$, graphitic C, Fe, α-Fe_2O_3, and γ-Fe_2O_3. a, Fe-CNT. b, CNT. c, Fe-CNT-ox. d, Fe-CNT-PA. e, Fe-CNT-Py.

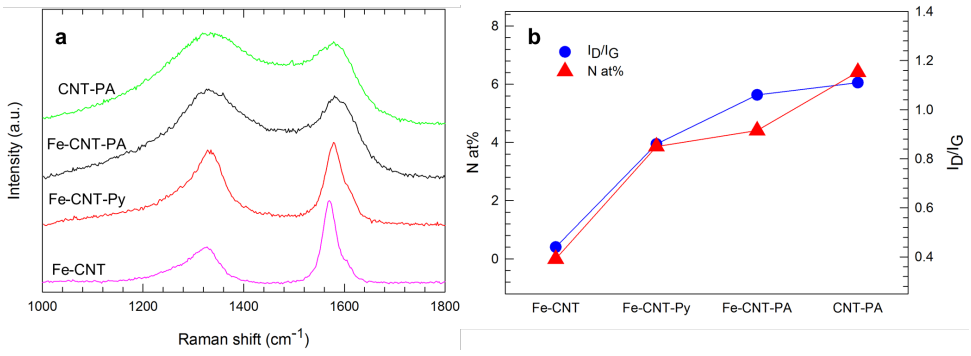

Figure 18 a, Raman spectra of Fe-CNT (pink), Fe-CNT-Py (red), Fe-CNT-PA (black), and CNT-PA (green). b, nitrogen at% and I_D/I_G of Fe-CNT, Fe-CNT-Py, Fe-CNT-PA, and CNT-PA.

2.3.3 Electrochemical performance

Their catalytic activities for ORR were tested by using both rotating disk electrode (RDE) and CV measurements in both 0.5M H_2SO_4 (Fig. 19a,b,c) and 0.1M KOH (Fig. 19d,e,f). Our samples were made into inks and applied to glassy carbon electrodes (unless specified) for easier experiments and comparison with other literature values. As depicted in Fig. 19a and 4d, the performance of Fe-CNT-PA was found to be the best in both acidic and alkaline environments. According to the RDE measurement in 0.5M H_2SO_4, the half-wave potential difference between Fe-CNT-PA and Pt/C (100 $\mu g_{Pt}/cm^2$) in 0.5M H_2SO_4 is only ~67 mV, which is comparable to or better than those of other non-Pt based catalysts tested in the same condition (practically meaningful strong 0.5M H_2SO_4 instead of weaker 0.1M $HClO_4$ commonly used in literature)[59, 72, 73]. It should be noted that other literatures used Pt/C electrodes with less Pt loading (on the order of 10 $\mu g_{Pt}/cm^2$). The limiting current density of Fe-CNT-PA, which is under mass-transport control, was slightly larger than that of Pt/C, suggesting more electrochemically active sites in Fe-CNT-PA than that of Pt/C. This could be partly due to the larger surface area and higher porosity of Fe-CNT-PA compared to Pt/C (see SEM images in Fig. 20).

The large peak current density of Fe-CNT-PA under the saturated oxygen environment in the CV result (Fig. 19b) also suggests a large number of active sites while the larger capacitive current indicates greater surface areas and enhanced O_2 transport within the catalyst layer[55] compared to Pt/C. When nitrogen was purged to deplete oxygen before and during CV test, a pair of redox peaks at 0.40 V and 0.45 V were observed, which can be attributed to the redox reaction between Fe^{2+} and Fe^{3+}.

In order to clarify the effect of the 3D pores in the sponge, CV was carried out with two differently prepared Fe-CNT-PA samples. For the first testing electrode (Fe-CNT-PA 3D), the as-synthesized Fe-CNT-PA was carefully cut and then directly attached to the glassy carbon electrode with carbon paint in order to preserve the porous 3D feature. For the second (Fe-CNT-PA 2D), the Fe-CNT-PA ink was dropped on the glassy carbon electrode until the same catalyst loading weight was reached. As shown in Fig. 19c, the 3D sample displayed markedly larger capacitive and kinetic current compared to 2D, which suggests greatly enlarged active surface areas and enhanced mass transport for ORR through the pores in the 3D structure.

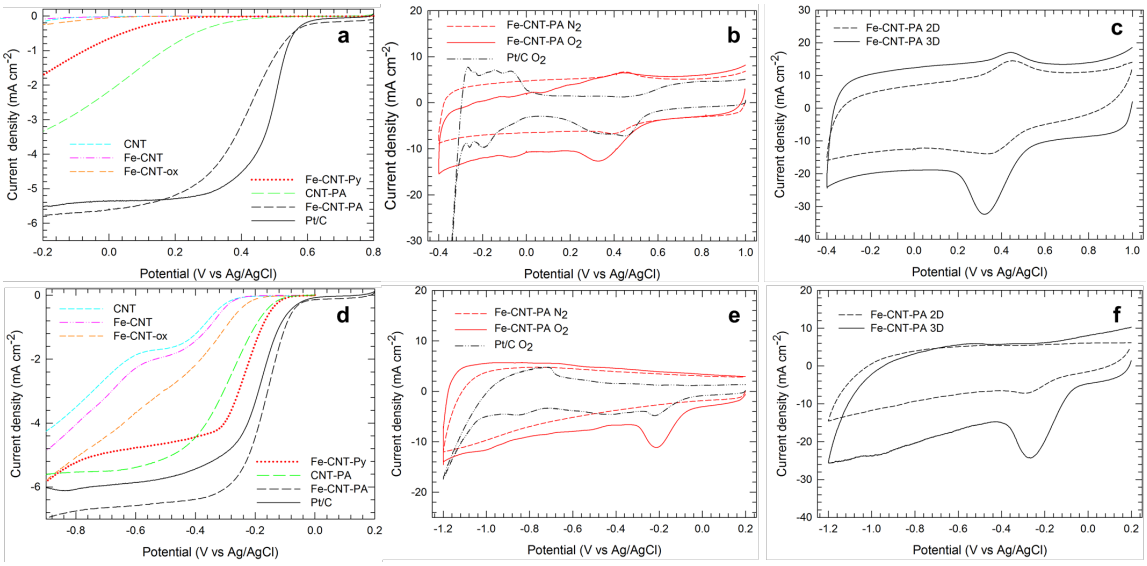

Figure 19 ORR performances in 0.5M H_2SO_4 (a,b,c) or 0.1M KOH (d,e,f). RDE polarization curves of CNT, Fe-CNT, Fe-CNT-ox, Fe-CNT-Py, CNT-PA, Fe-CNT-PA, and Pt/C in O_2-saturated 0.5M H_2SO_4 for a and in O_2-saturated 0.1M KOH for d. CV results of Fe-CNT-PA and commercial Pt/C (20 wt% Pt) in O_2- or N_2-saturated 0.5M H_2SO_4 for b and in O_2- or N_2-saturated 0.1M KOH for e. CV results of Fe-CNT-PA 2D and Fe-CNT-PA 3D in O_2-saturated 0.5M H_2SO_4 for c and in O_2-saturated 0.1M KOH for f. The apparent area was used to calculate the current density.

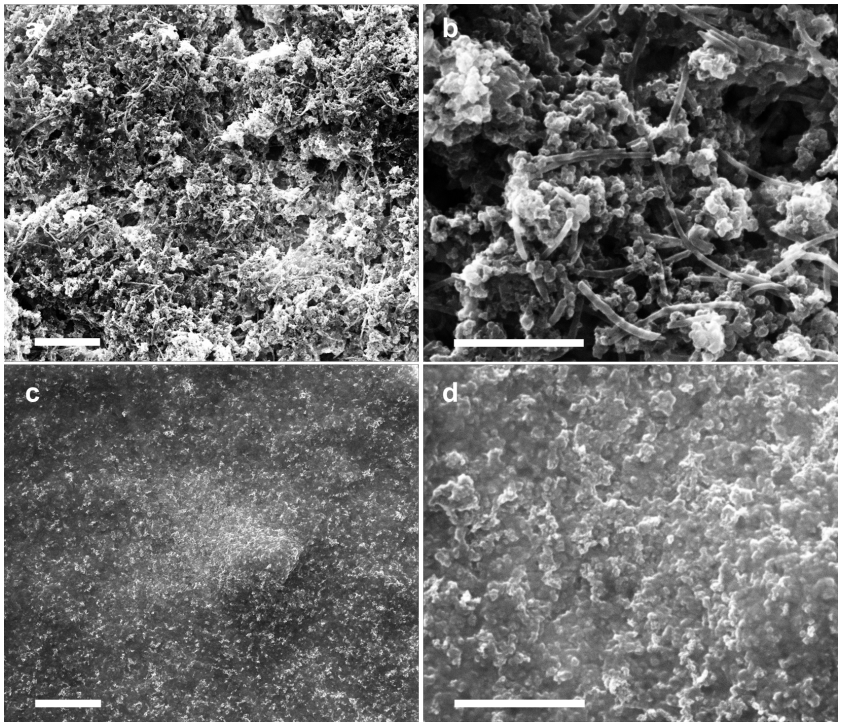

Figure 20 SEM images of the catalyst ink made of Fe-CNT-PA (a,b) and Pt/C (c,d). The ink was dopped and dried on copper foils for taking the SEM images. The scale bars indicate 10 μm for (a,c) and 4 μm for (b,d).

In 0.1M KOH, the limiting current density and half wave potential in the RDE results (Fig. 19d) for Fe-CNT-PA are both higher than those of Pt/C, indicating the high catalytic activity of Fe-CNT-PA in the basic environment. For Fe-CNT-PA, a clear reduction peak appeared on the CV profile for the O_2-saturated case in comparison to the N_2-saturated case (Fig. 19e). It also has a higher peak current density and capacitive current density than those of Pt/C, which is similar to those in the acidic environment. In addition, the Fe-CNT-PA 3D again showed a considerably improved performance compared to Fe-CNT-PA 2D in the basic environment (Fig. 19f).

In order to understand the origin of the different ORR activities, we analyzed at% of nitrogen, which is considered to comprise ORR active sites. The pyridinic N is often claimed to be more active for ORR[4, 74] presumably due to the nitrogen unbound to another carbon, but it is still under debate which one is most important among the total N, pyridinic N, and graphitic N. Our experimental results also indicate that nitrogen doping is essential to have good performance when the ORR activities of CNT, Fe-CNT, and Fe-CNT-ox (no nitrogen) were compared with those of the nitrogen-doped samples (see Fig. 19a,d). Here the nitrogen doping was differentiated by employing post doping with polyaniline for Fe-CNT-PA and CNT-PA and another post doping with pyridine for Fe-CNT-Py so as to compare the influence of nitrogen coordination and concentration on catalytic activities.

When we looked at the limiting current density (Fig. 19d; basic environment), which is closely related to the number of active sites for ORR, the highest was Fe-CNT-PA and CNT-PA was slightly better than Fe-CNT-Py. However, according to the XPS results (Table 2), the total nitrogen at% of Fe-CNT-PA was the lowest while CNT-PA had the highest total and pyridinic nitrogen at% and Fe-CNT-Py had the lowest total and pyridinic nitrogen at%'s. Note that the performance comparison was done for the basic environment since 0.5M H_2SO_4 is a very harsh environment that quickly degraded the samples "except" Fe-CNT-PA. Considering the performance of only CNT-PA and Fe-CNT-Py, this trend indicates that total or pyridinic nitrogen is important for ORR, but the high performance of Fe-CNT-PA despite the low nitrogen at% cannot be explained, suggesting ORR is not solely dependent on the nitrogen concentrations.

Table 2 Compositions of nitrogen-doped samples. Nitrogen and iron at% and the relative ratio of pyridinic N to graphitic N.

	Total N (at%)	Pyridinic N (at%)	Graphitic N (at%)	Pyridinic N : Graphitic N	Fe (at%)
CNT-PA	6.42	3.06	3.36	0.91	0.09
Fe-CNT-Py	3.86	1.81	2.05	0.88	0.90
Fe-CNT-PA	4.41	2.49	1.92	1.30	1.48

Therefore we further investigated the nitrogen coordination with iron since it has been claimed to be important in properly designing macrocycles with transition metals and nitrogen for ORR[4]. The initial ORR performance of macrocycles was found to be excellent but poor stability and complexity in synthesis made them impractical[75, 76]. For Fe-CNT-PA, we observed a clear shift of the pyridinic N 1s peak towards a higher binding energy (Fig. 21a), which can be attributed to its coordination with iron due to the formation of Fe-N_x aggregates during the pyrolysis process[77, 78]. The coordination between pyridinic N and iron was also confirmed by the downshift (lower binding energy that indicates the coordination effect[78, 79]) of Fe^{3+} $2p_{3/2}$ peak for Fe-CNT-PA compared to Fe-CNT-ox (no nitrogen content) from the high resolution Fe 2p scan (Fig. 21b). Here the Fe $2p_{3/2}$ peaks of Fe-CNT-PA and Fe-CNT-ox can be fitted with two peaks, corresponding to the Fe^{3+} in the bulk and Fe^{3+} at the surface. The higher binding energy (~715 eV) may originate from the surface mainly due to the deficiency of oxygen coordination at the surface[80, 81]. According to XRD (Fig. 17) and high-resolution TEM (HRTEM) (Fig. 16) results, Fe-CNT-PA and Fe-CNT-ox respectively have γ-Fe_2O_3 and α-Fe_2O_3. For γ-Fe_2O_3, 3/8 of the Fe^{3+} cations are in the tetrahedral sites and the rest are in the octahedral sites, while, for α-Fe_2O_3, all Fe^{3+} cations are in the octahedral sites[82]. However, according to the previous report[81], there is no clear difference in the Fe $2p_{3/2}$ peaks of γ-Fe_2O_3 and α-Fe_2O_3.

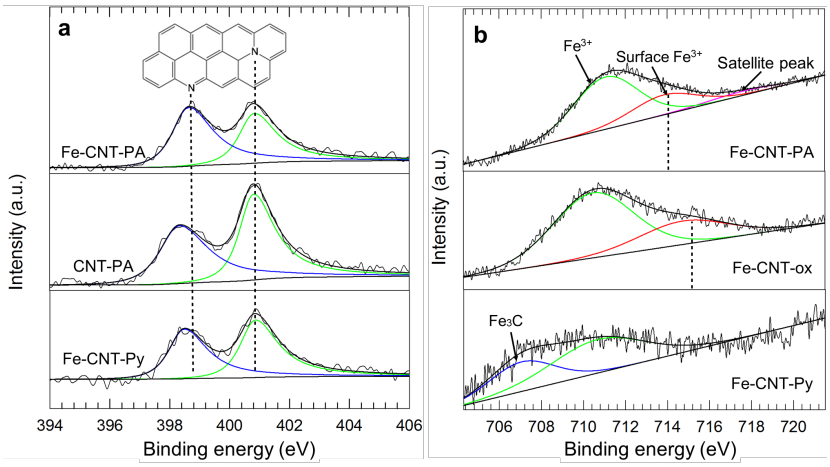

Figure 21 XPS analysis and comparison. a, N 1s peaks of the nitrogen doped samples (Fe-CNT-PA, CNT-PA, and Fe-CNT-Py). Left and right vertical broken lines respectively indicate the location of pyridinic and graphitic nitrogen in Fe-CNT-PA. b, Fe 2p peaks of the Fe-containing samples (Fe-CNT-PA, Fe-CNT-ox, and Fe-CNT-Py). The vertical broken lines indicate the peak locations of the surface Fe^{3+}.

In addition, Fe-CNT-PA has the highest iron at% (1.48%) from TGA (Table 2, Fig. 14), but the peak intensity of Fe, $Fe_{15.1}C$, and Fe_3C were the lowest according to the XRD result (Fig. 17), suggesting that many of the iron in Fe-CNT-PA may be coordinated with nitrogen to form the primary ORR active site rather than crystalized into the iron compounds. Hence, we speculate that the pyridinic N coordinated with iron is the primary ORR active site that provides the high ORR activity, while the other nitrogen sites are the secondary ORR active sites. For Fe-CNT-Py, the peak at ~707.2 eV matches Fe_3C in literature[83, 84], while the other peak (~711 eV) could be the oxidation of Fe_3C on the surface, resulting in Fe^{3+} characteristics[83].

In order to examine the role of Fe_2O_3, we intentionally converted the iron compounds in Fe-CNT to Fe_2O_3 by annealing in air at 400 °C for 5 hour to obtain Fe-CNT-ox, as confirmed by XRD (Fig. 17c). Negligible differences in ORR performance

were observed (Fig. 19a,d), suggesting iron oxide is barely active for ORR. The influence of Fe by itself on ORR was also found to be trivial by comparing the ORR performance of CNT and Fe-CNT (Fig. 19a,d), but the difference in the ratios of the pyridinic N to graphitic N in CNT-PA (0.91) and Fe-CNT-PA (1.30) (Table 2) may suggest that iron is helpful in forming pyridinic nitrogen rather than graphitic nitrogen presumably due to the coordination of nitrogen with iron. The high ORR activities would have resulted in efficient 4-electron reactions for Fe-CNT-PA according to the Koutecky-Levich plots derived from RDE tests with different rotating speeds in both acidic (Fig. 22a) and basic (Fig. 22b) solutions (see Fig. 23 for polarization curves as a function of the rotational speed).

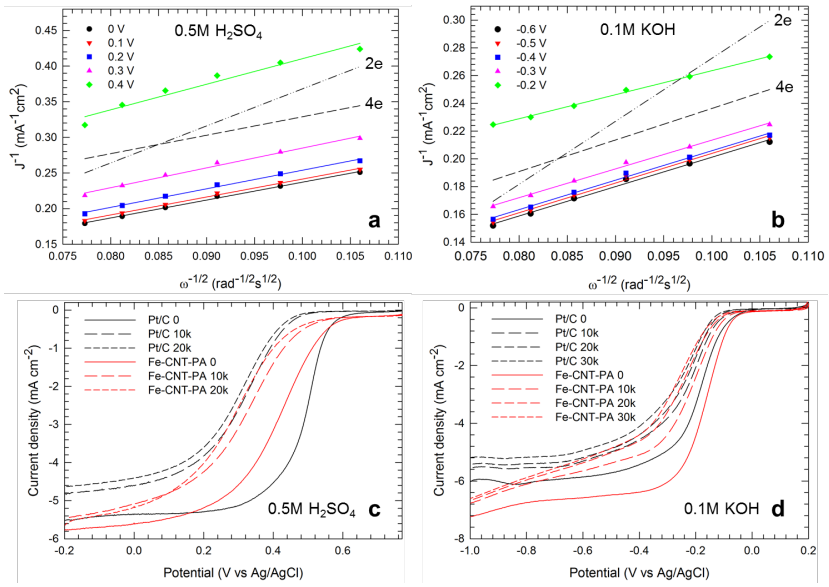

Figure 22 Koutecky-Levich plots (a,b) and RDE polarization curves at different cycle numbers (c,d) for Fe-CNT-PA in O_2-saturated 0.5M H_2SO_4 or O_2-saturated 0.1M KOH. The Koutecky-Levich plots were obtained from the results at 6 different rotational speeds of the electrode, starting from 1600 rpm to 850 rpm (every 150 rpm) 150 pm (see Fig. 23). The RDE polarization curves of Fe-CNT-PA were compared with those of commercial Pt/C (20-wt% Pt) before and after 10000, 20000, and/or 30000 CV cycles.

The rotating speed and scan rate of all curves in (a) and (d) is 1600 rpm and 5 mV s^{-1}, respectively.

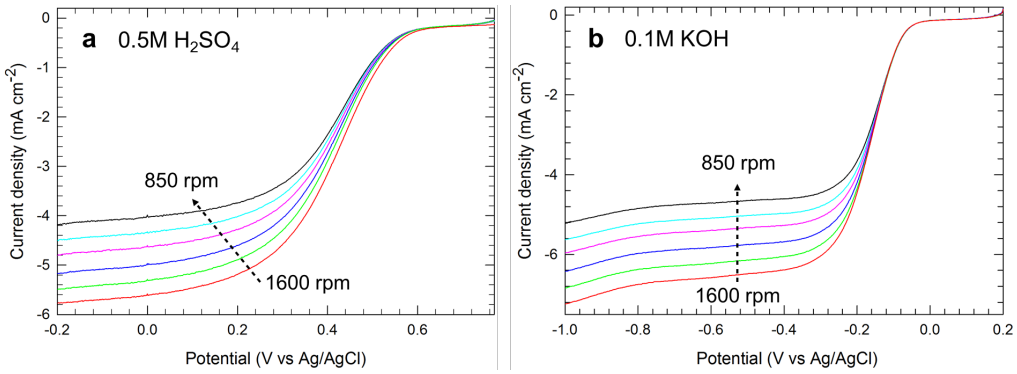

Figure 23 RDE test results at 1600 rpm and lower rotating speeds (every 150 rpm) with Fe-CNT-PA in O_2-saturated 0.5M H_2SO_4 for a and O_2-saturated 0.1M KOH for b.

More importantly, the long-term stability testing of Fe-CNT-PA in both 0.5M H_2SO_4 (Fig. 22c) and 0.1M KOH (Fig. 22d) shows better limiting current density retentions than those of Pt/C. The reduction of the half-wave potential for Fe-CNT-PA and Pt/C was 0.13 V and 0.21 V, respectively, after 20000 cycles in O_2-saturated 0.5M H_2SO_4. In O_2-saturated 0.1M KOH, the half-wave potentials of Fe-CNT-PA and Pt/C respectively decreased by 0.13 V and 0.11 V after 30000 cycles. In particular, the high stability of our Fe-CNT-PA is remarkable since non-precious metal or metal oxide based catalysts in such a harsh acidic environment usually show rapid and severe degradation due to the decomposition of catalyst structures and the protonation reaction[56, 57, 76]. In fact, the initial catalytic performances of various complexes such as multi-wall carbon nanotubes with cobalt porphyrin[72], carbon nanofibers pyrolyzed with of iron, polypyrrole, and ethylenediamine[59], and carbon black pyrolyzed with polymerized p-

phenylenediamine and ferric chloride[73] were comparable to Pt/C in 0.5M H_2SO_4. These studies, however, did not show such long-term stability.

Our Fe-CNT-PA catalysts also outperform recently-reported relatively-stable non-precious metal based catalysts tested in 0.5M H_2SO_4. For example, the limiting current density of our Fe-CNT-PA dropped ~9 % after 20000 cycles (Fig. 22c), but carbon particle complexes[11] made by sintering Fe, C, and polyaniline exhibited a similar drop after only 5000 cycles. It is also worth noting that our Fe-CNT-PA was cycled under O_2-saturated 0.5M H_2SO_4, while the carbon particle complexes were cycled under N_2-saturated 0.5M H_2SO_4. The higher O_2 concentration normally leads to a higher degradation rate of such catalysts, which implicates that our catalyst has an excellent long-term stability maintaining the active site even in the harsh environment.

Furthermore, in 0.1M KOH, the half-wave potential from our Fe-CNT-PA is 15 mV and 120 mV higher than those of aerogel hybrids made of iron nitride and nitrogen doped graphene[58] and nitrogen-doped graphene[85], respectively, and similar to those of polyaniline-derived N-/O-doped mesoporous carbons[51], and nitrogen-doped gelatin-carbon black sheets[86]. In terms of stability, degradations of our Fe-CNT-PA were marginal even after 30000 cycles in O_2 saturated 0.1M KOH, resulting in 0.13 V drop of the half wave potential and 8 % reduction in the limiting current density, which is comparable to or better than the recently reported[55, 87].

2.4 Conclusions

Free-standing nitrogen-doped CNT-based electrocatalysts for ORR were synthesized by using a facile and scalable method, showing striking limiting current

density and stability that are comparable to or better than those of platinum-based catalysts in both acidic and basic solutions. The excellent performance could be attributed to nitrogen-iron coordination forming highly ORR-active sites as well as the porous 3D structure facilitating mass transport. Iron and its compounds were found to be negligibly active in boosting ORR, but Fe^{3+} could be crucial in forming the primary ORR active site, which is Fe^{3+} coordinated with pyridinic nitrogen. We believe that the high electrical conductivity and high corrosion resistance of carbon nanotubes help to improve the catalytic activity and stability. The unique self-standing 3D porous structure along with outstanding performances will be of great promise for commercializing various electrochemical cells.

CHAPTER III

BIFUNCTIONAL NANO-SPONGES SERVING AS NON-PRECIOUS METAL CATALYSTS AND SELF-STANDING CATHODES FOR HIGH PERFORMANCE FUEL CELL APPLICATIONS*

3.1 Introduction

Microbial fuel cell (MFC) is a promising renewable energy technology for the production of electrical energy during wastewater treatment.[18] Electrochemically active bacteria (EAB) oxidize organic compounds and transfer electrons to the anode. The electrons move through an external circuit to the cathode where the electron acceptors are reduced.[88] Various electron acceptors such as ferricyanide and permanganate have been used in the cathode to improve the power generation, but they are not considered to be ideal cathode reactants due to toxicity, non-sustainability, and cost issues.[89] Oxygen is a cost-effective, sustainable, nature-friendly, and scalable electron acceptor for practical applications. However, the slow rate and high overpotential of the oxygen reduction reaction (ORR) are the two critical issues[90] that limit the performance of MFCs. There are two different chemical pathways (two- and four- electron) through which oxygen is reduced to hydrogen peroxide or water. The two-electron pathway exhibits a high overpotential for ORR, which is less efficient than the four-electron pathway normally observed with precious-metal based catalysts.[90, 91]

---

* Reprinted with permission from G. Yang, C. Erbay, S.-i. Yi, P. de Figueiredo, R. Sadr, A. Han and C. Yu, *Nano Energy*, 2016, **22**, 607-614.

Platinum-based catalysts have been regarded optimal for electrochemical reactions because they support the four-electron pathway and display low overpotential. However, the prohibitively high price of platinum prevents their use in large-scale applications.[92, 93] Thus, it is essential to develop low-cost ORR catalysts without sacrificing the performance of Pt-based catalysts. In the past several years, various catalysts have been proposed such as biocathodes (biofilm grown cathode),[94] conductive polymers (polyaniline,[95] polypyrrole[96]), macrocyclic compounds (Co-naphthalocyanine,[97] pyrolyzed iron ethylenediaminetetraacetic[98, 99]), metal oxides (manganese dioxide,[100, 101] lead oxide[102]), and carbon based (carbon nanotubes (CNTs),[103] graphene,[104, 105] activated carbon nanofibers[106]) materials. Recently, CNT-hybrid cathodes containing Pt,[107, 108] MnO_2,[101, 109, 110] chitosan,[111] and iron phthalocyanine (FePc)[112] have displayed promising properties such as low cost and improved ORR activities mainly due to the large surface area and good conductivity of CNTs. Moreover, their high mechanical strength and excellent chemical stability have contributed to the development of durable cathodes. Nevertheless, power generation and stability with these catalysts are typically inferior to those of conventional Pt-based catalysts, or/and their synthesis processes are too complicated to be viable in practice.

Here we fabricated three-dimensional (3D) nitrogen-enriched iron-coordinated CNT (N/Fe-CNT) sponges as high-performance cathodes using simple and low-cost fabrication processes. A two-stage chemical vapor deposition (CVD) method was used to synthesize a self-assembled 3D framework consisting of intertwined nitrogen-enriched CNTs. The structure and chemical composition of the N/Fe-CNT sponge were

investigated by scanning/transmission electron microscopy (SEM/TEM), X-ray diffraction (XRD), X-ray photoelectron spectroscopy (XPS), and Raman spectroscopy. The performances of the N/Fe-CNT-loaded MFCs were experimentally obtained using wastewater in anode chambers, and compared with that of MFCs with commercial Pt/C-coated carbon cloth (Pt-CC) cathodes. Cyclic voltammetry (CV) and rotating disk electrode (RDE) tests were also conducted to evaluate the electrocatalytic activity for ORR.

3.2 Experimental

3.2.1 Preparation of N/Fe-CNT sponges

Sponge-like porous 3D CNTs were first synthesized using a CVD method in a three-zone tube furnace equipped with a quartz tube (inner diameter: ~22 mm). Details can be found from our previous work.[113] Without taking out the as-synthesized CNT sponge from the quartz tube, the furnace temperature was increased to 800 °C. As soon as the reaction zone temperature reached 800 °C, pyridine (Alfa Aesar, 99+%) was injected into the tube using a syringe pump (Model KDS-100, KD Scientific) at a feeding rate of 20 mL h^{-1}, while argon gas and hydrogen gas were flowed at 1000 sccm and 100 sccm, respectively. The total amount of pyridine injected was proportional to the mass of pristine CNT sponge with a ratio of 25 mL of pyridine to 1 g of CNT sponge. After 1 h reaction, the quartz tube was naturally cooled under 200-sccm argon flow to room temperature.

3.2.2 Materials characterization

The morphology and microstructure of the N/Fe-CNT sponge were characterized with SEM (FEI Quanta 600) and TEM (JEOL JEM-2010). The crystalline structure of the

N/Fe-CNT sponge was studied by XRD measurement (Bruker-AXS D8 VARIO with Cu Kα X-ray) and XPS (Omicron XPS/UPS system with Argus detector, Mg Kα as the X-ray source) was conducted to reveal the chemical composition and environment of the N/Fe-CNT sponge. A survey scan was first recorded with 1.0 eV step size, followed by high-resolution scans of C 1s, N 1s, O 1s, and Fe 2p, using 0.05 eV step size. Raman spectroscopy was carried out on Horiba Jobin-Yvon LabRam with an excitation wavelength of 632.8 nm at room temperature.

3.2.3 MFC configuration and operation

The air bubbled two-chamber MFCs with a total volume of 40 mL (~20 mL each for cathode and anode) were used to test the performance of all cathodes (N/Fe-CNT sponges and Pt-CC). Cylindrical acrylic chambers with 3 cm in inner diameter and height were fabricated using a milling machine (MDX-40, Roland DGA). Carbon felt (1×1 cm^2) (Morgan, UK) was used as anode in all MFCs. Titanium wires were permanently glued to the electrodes using silver epoxy for electrical connection. After placing proton exchange membranes (Nafion 117^{TM}, Ion Power Inc.) with silicone rubber gaskets, the chambers were screwed tightly to prevent leakage. The anode chambers were inoculated with 20-vol% anaerobically activated sludge (Austin Wastewater Treatment Plant, Texas, USA) and 80-vol% medium solution containing PBS (100 mM) and autoclaved anaerobic nutrient mineral buffer (NMB, pH 7.0)[114, 115] (PBS:NMB = 37:1 by vol) with sodium acetate (2 g L^{-1}). The cathode chambers were filled with 100 mM PBS as catholyte and continuously purged with air to supply oxygen. When the voltage dropped below ~50 mV, the anolyte was replaced with fresh one and then nitrogen gas was purged for 15 min to

remove oxygen in the anode chambers. The anolyte was mixed using a magnetic stirrer (350 rpm) during the experiment. Cell voltages across an external resistor (1500 Ω) were recorded every 2 min using a data acquisition system (National Instruments) via a LabView™ (National Instruments) interface.[116, 117] Polarization curves were obtained by varying the load resistor from 10 kΩ to 50 Ω when the voltage was stable after several operation cycles. Power (P) curves were calculated using $P = V \times I$ with the recorded voltage (V) and measured current (I) with the load resistors. The current and power densities were normalized by the volume (20 mL) of the anode chamber.

3.2.4 Electrochemical measurements

The electrochemical measurements were conducted on an electrochemical workstation (CHI 604D, CH Instrument) with a three-electrode system (Ag/AgCl as a reference electrode, Pt wire as a counter electrode, and sample mounted glassy carbon electrode as a working electrode). To mount the samples on glassy carbon electrodes, catalyst ink was made by mixing 7-mg N/Fe-CNT sponge or Pt/C (20-wt% Pt, Fuel Cell Earth), 160-μL 5-wt% Nafion solution (Fuel Cell Earth), 170-μL ethanol (EMD Millipore, 92%-94%), and 670-μL deionized water, followed by sonication for 30 min. Then 5-μL catalyst ink was drop-casted on the glassy carbon electrode resulting an areal loading of 0.5 mg cm^{-2}. Both CV and RDE tests were performed in a O_2-saturated (bubbling oxygen gas for 30 min before each test) 50-mM PBS (pH=7.6) solution. CV tests were recorded in a potential range of -1.0 ~ 0.5 V with a scan rate of 0.1 V s^{-1}. RDE tests were conducted at different rotating speeds (1600 rpm to 850 rpm with 150 rpm interval) between -0.7 V and 0.4 V at 0.01 V s^{-1} scan rate. Stability tests were performed by cycling between -0.5

V and 0.1 V with a scan rate of 0.1 V s^{-1} for 20000 cycles followed by RDE test at 1000 rpm with a scan rate of 0.01 V s^{-1}.

3.3 Results and discussions

3.3.1 Microstructure of nano-sponges

Pristine CNT sponges were formed at the end of the first stage of the synthesis process, and a nitrogen doping process was carried out at a higher temperature in the second stage (see the experimental section). The form of the as-synthesized N/Fe-CNT sponge (Fig. 24a) reflects the cylindrical shape of a quartz furnace tube in which the sponge was synthesized, and no fracture was observed even with 90°-bending (Fig. 25). The self-standing and deformable features differentiate the N/Fe-CNT sponge from other catalysts previously reported for MFC cathodes,[103, 104, 107, 118-120] which require an additional catalyst loading layer such as carbon cloth and carbon paper due to their powdery catalysts. The additional catalyst loading layer will not only add extra cost to MFCs but also increase the internal resistance of cathode.

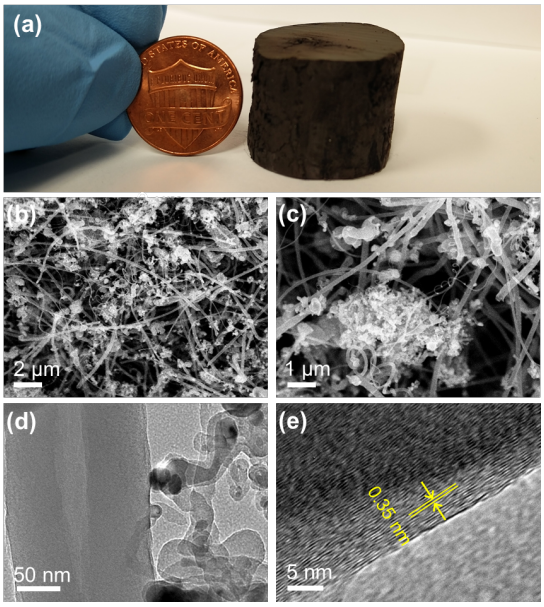

Figure 24 Morphology and structure of N/Fe-CNT. (a) An as-synthesized self-standing N/Fe-CNT sponge. (b-c) SEM images of N/Fe-CNT sponge showing small intertwined CNTs and small aggregates attached to the wall of CNTs. (d-e) TEM images of N/Fe-CNT showing graphitic layers of multi-wall CNTs.

Figure 25 Photo of an as-synthesized CNT sponge bent close to 90°, showing its excellent structural integrity.

SEM images in Fig. 24b and c show that CNTs were randomly oriented and intertwined, creating porous 3D sponge-like frameworks. A post-treatment with pyridine at 800 °C generated small aggregates composed of carbon and iron compounds on the wall of CNTs (Fig. 24c and d). In addition, a high-resolution TEM (HRTEM) image (Fig. 24e) revealed that the inner walls of CNTs were composed of more ordered graphitic layers compared to the less ordered outer walls due to the nitrogen incorporation. The graphitic structure ensures a high electrical conductivity, which is important in charge transfer processes during ORR.[113]

In the XRD pattern of the N/Fe-CNT sponge (Fig. 26a), the peak at 26.2° corresponds to (002) planes of concentric graphitic carbon, which indicates the interlayer distance of 0.34 nm (close to 0.35 nm measured from the HRTEM image shown in Fig. 24e) according to the Bragg's law. Other peaks were assigned to iron or iron-carbon compounds (Fe_3C and $Fe_{15.1}C$). No peak associated with nitrogen-containing compounds was found in the XRD result, suggesting nitrogen was mostly incorporated into the graphitic carbon (*e.g.*, pyridinic and graphitic nitrogen) or amorphous iron-nitrogen compounds. Raman spectra (Fig. 26b), therefore, were taken to investigate the effect of nitrogen incorporation into the graphitic carbon structure. The Raman spectra of both pristine CNT sponge and N/Fe-CNT sponge displayed D-band (~1330 cm^{-1}) and G-band peaks (~1572 cm^{-1}) of graphitic materials.[121] The D-band is associated with a double resonance effect by defects, while the G-band is related to the in-plane vibration mode of sp^2 carbon.[122] The intensity ratio of the D-band to G-band (I_D/I_G) qualitatively indicates the crystallinity of the graphitic carbon structure. I_D/I_G is higher for N/Fe-CNT sponge

(0.81) compared to CNT sponge (0.44), suggesting disordered structures induced by the nitrogen incorporation.[123]

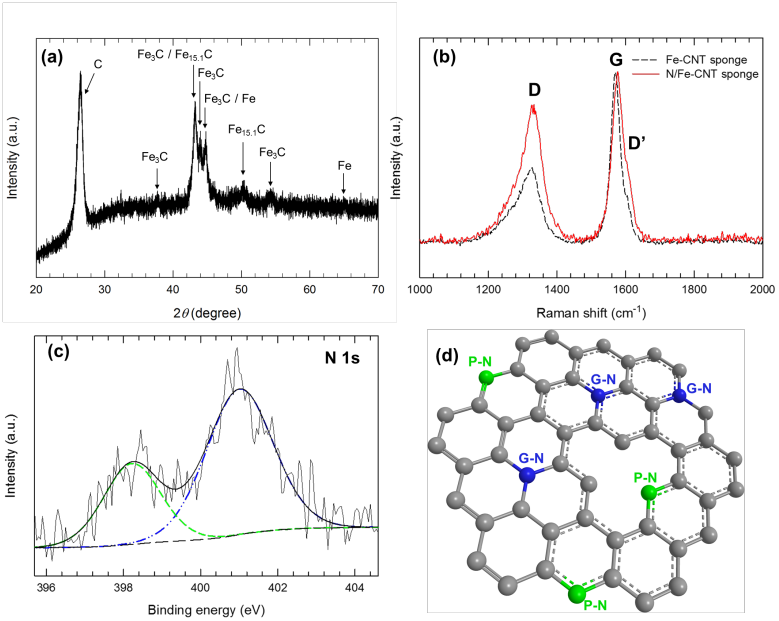

Figure 26 Crystal structure and chemical composition of N/Fe-CNT. (a) XRD pattern of a N/Fe-CNT sponge where carbon, iron, and iron compound peaks were identified. (b) Raman spectra of a pristine CNT sponge and a N/Fe-CNT sponge, indicating the increased number of defects after nitrogen incorporation. (c) High-resolution scan of N 1s, deconvoluted into pyridinic nitrogen (398.4 eV) and graphitic nitrogen (401.0 eV). (d) Schematic representation of nitrogen incorporated graphitic structure. The spheres represent carbon and nitrogen atoms, and P-N and G-N respectively denote pyridinic nitrogen and graphitic nitrogen.

The chemical structure and composition of the N/Fe-CNT sponge were further characterized by XPS (Fig. 27), revealing the presence of carbon, nitrogen, oxygen, and iron, which is consistent with the elements in the precursors. The high-resolution scan of N 1s (Fig. 26c) displayed two components corresponding to the pyridinic nitrogen (398.4 eV) and graphitic nitrogen (401.0 eV). The pyridinic nitrogen is bonded with two carbon atoms, contributing one p-electron to the conjugated π system, having a lone pair of

electrons positioned in plane with the graphitic carbon. The graphitic nitrogen is bonded with three carbon atoms by replacing the original carbon atoms in the graphitic plane. Their structures are schematically shown in Fig. 26d. These nitrogen groups were intentionally made with the pyridine precursor since they are essential in improving the catalytic activity of the carbon-based catalysts for ORR.[113] The nitrogen composition was found to be ~2% according to the XPS results (Table 3, Fig. 27).

Table 3 Atomic composition of the N/Fe-CNT sponge.

C at%	Fe at%	N at%	O at%
85.34	0.24	2.01	12.41

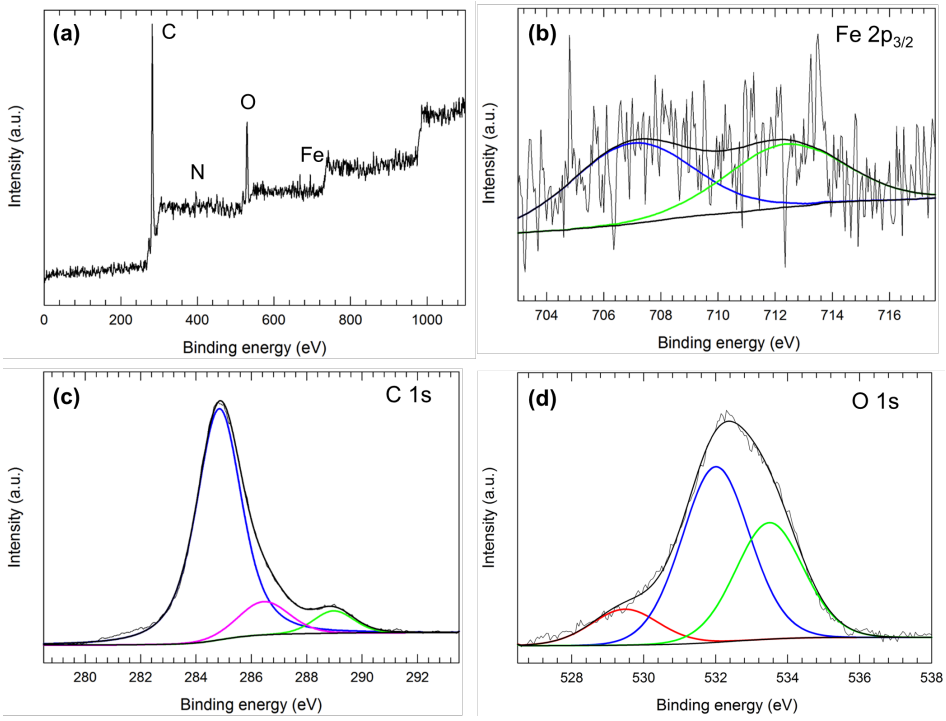

Figure 27 XPS results of the N/Fe-CNT sponge. (a) Survey scan. High-resolution scans of Fe $2p_{3/2}$ (b), C 1s (c), and O 1s (d).

3.3.2 Microbial fuel cell performances

Four different N/Fe-CNT sponges (N/Fe-CNT10, N/Fe-CNT12, N/Fe-CNT15, N/Fe-CNT18) were tested as cathodes, as listed in Table 4, to investigate their performances for power generation in two-chamber MFCs (20-mL each for cathode and anode chambers). The variation in the tested samples was designed to identify the best pore volume per electrode mass (or surface area) as well as to investigate the dependency of power generation on electrode mass (or surface area). For ORR, the pore volume per mass is closely related to oxygen diffusion and the effective electrical conductivity, while the mass of the CNT sponge is proportional to its active surface area. Note that we used mass as an indicator of the electrode surface area, which is estimated to be 19 m^2 per gram of CNT.[124] For comparison, we used Pt-CC whose single side was loaded with Pt/C and then cut into two squares (1.8×1.8 cm^2). The two pieces were then attached using silver epoxy so that the Pt/C loaded sides were facing opposite each other and the Pt/C were in direct contact with the solution during MFC testing. The thickness of the single Pt-CC sheet was measured to be 0.35 mm. The area of the 2D Pt-CC (3.2 cm^2) was chosen to be close to the cross sectional area of the 3D N/Fe-CNT samples (3.1 cm^2). This design allowed us to investigate the influence of porous structures on MFC performance. The anode was made of 1×1 cm^2 carbon felt (same size for all testing), and all other conditions were kept the same.

Table 4 Characteristics of the tested cylindrical N/Fe-CNT sponge samples whose diameter is 20 mm. The pore volumes are average values calculated with CNTs whose outer/inner diameters and density are respectively 150/20 nm and 2.2 g cm^{-3}.

	Length (mm)	**Mass (mg)**	**Volume/Mass (cm^3 g^{-1})**	**Density (mg cm^{-3})**	**Pore volume (μm^3)**
N/Fe-CNT10	10	362	8.67	115	0.796
N/Fe-CNT12	12	402	9.37	107	0.894
N/Fe-CNT15	15	413	11.4	87.7	1.239
N/Fe-CNT18	18	385	14.7	68.1	1.864

Five MFCs loaded with N/Fe-CNT10, N/Fe-CNT12, N/Fe-CNT15, N/Fe-CNT18, and Pt-CC cathodes were constructed and tested in a batch mode. Fig. 28a shows the output voltage as a function of time over 3 months with a 1500-Ω external resistor for N/Fe-CNT12 and Pt-CC cathodes. Both cells demonstrated negligible degradation over 3 months, and the N/Fe-CNT loaded cell showed slightly higher output voltage, indicating excellent stability and activity. We also obtained volumetric power densities based on anode chamber volume (20 mL) at steady power production stages (Fig. 28b). The maximum power densities of N/Fe-CNT12 (14.1 W m^{-3}) and Pt-CC (12.8 W m^{-3}) loaded MFCs were similar, but N/Fe-CNT10 loaded MFC, which is shorter than N/Fe-CNT12, had a lower maximum power density (9.1 W m^{-3}). The longer N/Fe-CNT15 and N/Fe-CNT18 resulted in higher maximum power densities compared to the MFCs with N/Fe-CNT12 and N/Fe-CNT10.

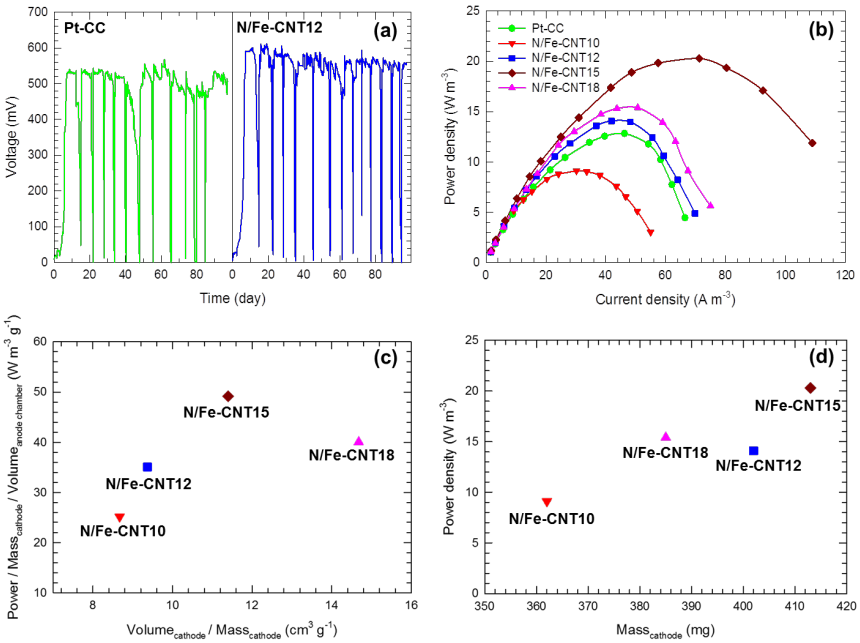

Figure 28 MFC performances with N/Fe-CNT sponge and Pt-CC cathodes. (a) Voltage output over 1.5 kΩ resistor from MFCs equipped with N/Fe-CNT12 and Pt-CC cathodes. (b) Polarization curves with all N/Fe-CNT sponges and Pt-CC cathodes. (c) Volumetric (anode volume) power produced per cathode mass with the change of pore volume per cathode mass. (d) Volumetric (anode volume) power with respect to the mass of cathodes. To obtain the volumetric power, the measured power was divided by the volume of the anode chamber (20 mL).

However, as for the MFCs with the two highest maximum power densities, the shorter N/Fe-CNT15 (20.3 W m^{-3}) produced higher power than the longer N/Fe-CNT18 (15.4 W m^{-3}). We believe that this trend in the power density is related to the competing effects caused by the oxygen diffusion/reduction rate, the effective electrical conductivity, and the active surface area, which are closely related to the pore volume per cathode mass and the cathode mass (or surface area). As shown in Fig. 28c, the volumetric (anode volume) power produced per cathode mass increased with the enlarged pore volume per cathode mass until it reaches 11.4 cm^3/g (N/Fe-CNT15). Then, this power density dropped

when the pore volume per cathode mass was further raised to 14.7 cm^3/g (N/Fe-CNT18). The initial increase in the power per cathode mass, which indicates the productivity of cathode by normalization with cathode mass, suggests that the reaction is strongly influenced by oxygen supply. Smaller pore volumes may result in insufficient oxygen conditions (lack of electron acceptors) due to limited oxygen diffusion, thereby retarding ORR. Table 4 displays the average pore volumes calculated with CNTs whose outer/inner diameters and density were estimated to be 150/20 nm and 2.2 g cm^{-3}, respectively. The power density drop for N/Fe-CNT18 (Fig. 28c) is likely to come from the lower effective electrical conductivity compared to N/Fe-CNT15. When sponges are too porous, the number of electrically connected junctions between CNTs are small, resulting in less effective electron conduction through the CNTs. This may also suggest that the pore volume in N/Fe-CNT15 is large enough for sufficient oxygen supply. On the other hand, more active mass resulted in larger volumetric power density, as observed from the power density of N/Fe-CNT10, N/Fe-CNT18, and N/Fe-CNT15 (Fig. 28d). Despite the larger cathode mass of N/Fe-CNT12 than that of N/Fe-CNT18, the power generation from N/Fe-CNT12 and N/Fe-CNT18 was similar, which could be attributed to the smaller pore volume in N/Fe-CNT12 (Fig. 28c). Additionally, polarization curves of all cathodes showing voltage with respect to current density were compared in Fig. 29.

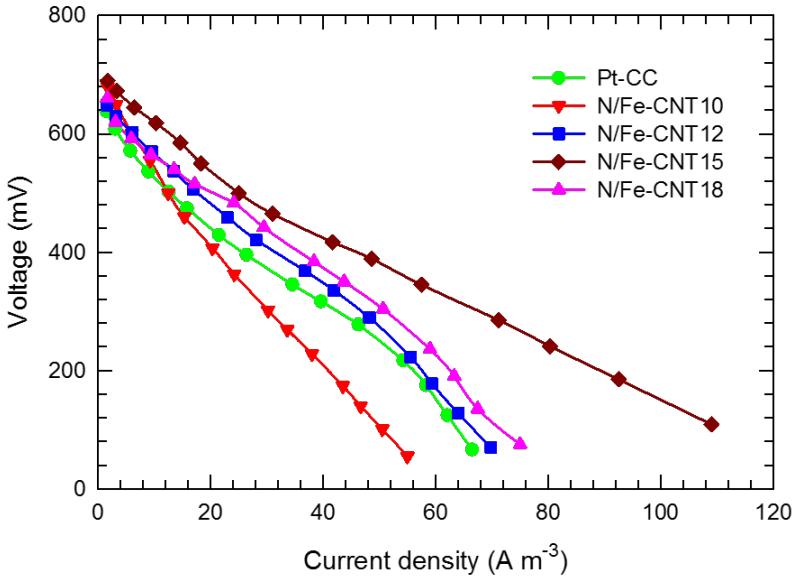

Figure 29 Polarization curves of all MFCs equipped with the N/Fe-CNT sponge and the Pt-CC cathodes.

3.3.3 Electrochemical tests for catalytic activity

In order to uncover the reason behind the high performance of the N/Fe-CNT sponges as cathodes for MFCs, electrochemical properties of the N/Fe-CNT sponges were further characterized by CV and RDE tests. In both tests, the catalysts (N/Fe-CNT sponge and Pt/C) were made into catalyst ink and then dropped on glassy carbon electrodes followed by drying (see the experimental part). According to the CV results (Fig. 30a) in O_2-saturated 50-mM phosphate buffer solution (PBS) (pH=7.6), strong oxygen reduction peaks were observed for both N/Fe-CNT and Pt/C. The resemblance of the peak location and intensity suggests similar catalytic activity for ORR.

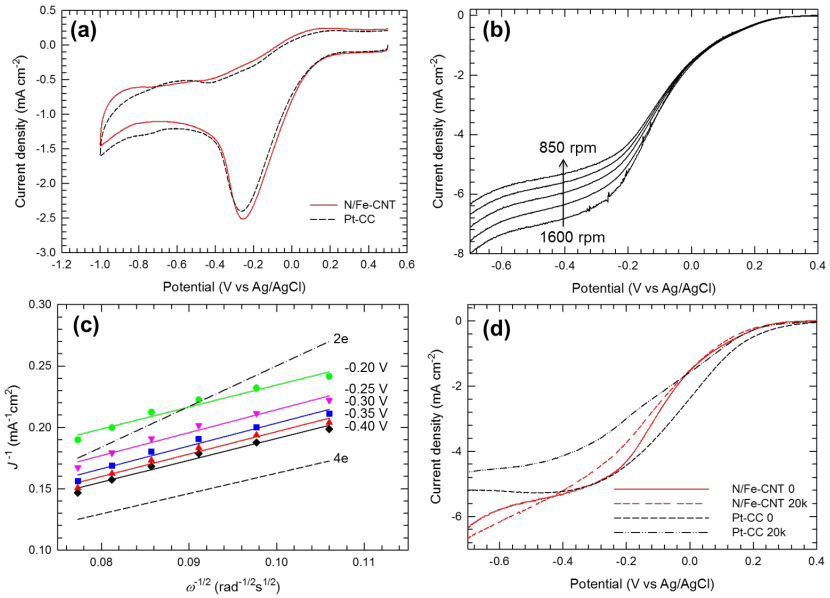

Figure 30 Electrochemical properties of N/Fe-CNT. (a) CV results of N/Fe-CNT and Pt/C catalysts showing strong oxygen reduction peaks. (b) RDE test results of N/Fe-CNT in O_2-saturated 50 mM PBS. The rotating speed was changed from 1600 rpm to 850 rpm with 150 rpm interval. All data were recorded from 0.4 V to -0.7 V with a scan rate of 0.01 V s^{-1}. (c) Koutecky-Levich plots of N/Fe-CNT, indicating the 4-electron ORR process. (d) RDE test results (1000 rpm) of N/Fe-CNT and Pt/C before and after 20000 CV cycles. All electrochemical tests were performed in O_2-saturated 50 mM PBS. The scan rate was 0.1 V s^{-1} and 0.01 V s^{-1} for CV and RDE, respectively.

RDE tests for both N/Fe-CNT (Fig. 30b) and Pt/C (Fig. 31a) were performed in the same O_2-saturated 50 mM PBS with rotating speed changing from 1600 rpm to 850 rpm at 150 rpm interval. The inclined plateaus from N/Fe-CNT near -0.6 V *vs* Ag/AgCl, compared to reltaively flat one from Pt/C, is likely to be caused by the porous structure of our catalysts[125] as well as nonuniformity of catalytic sites.[126] Oxygen accessibility of some catalytic sites in the porous structure is presumably different from others due to tortuous paths and carbonaceous clumps having different accessbility, which results in lower potentials and/or longer diffusion time.[127-129] On the other hand, according to XPS results, our samples contain different kinds of ORR active sites such as pyridinic nitrogen,

graphitic nitrogen, and their coordination with iron. Since different catalytic sites may participate in ORR at different ranges of potentials, our multi-catalytic sites would have resulted in an inclined plateau as a whole, which has been explained using a model with different electrocatalytic sites.[126] The Koutecky-Levich plots were generated based on the RDE test results, as shown in Fig. 30c and Fig. 31b respectively for N/Fe-CNT and Pt/C. According to the Koutecky-Levich equation, $J^{-1} = {J_K}^{-1} + B^{-1}\omega^{-1/2}$ and $B = 0.6\ 2nFCD^{2/3}\nu^{-1/6}$, where J_K is the kinetic limiting current density, ω is the rotational speed, n is the number of electron transferred, F is the Faraday constant (F = 96485 C mol^{-1}), C is the bulk concentration of O_2 (1.3×10^{-6} mol cm^{-3}), D is the diffusion coefficient of O_2 (2.7×10^{-5} cm^2 s^{-1}), and ν is the kinematic viscosity of the solution (0.01 cm^2 s^{-1}), there is a linear relation between J^{-1} and $\omega^{-1/2}$ and the slope depends on the number of electrons involved in the reaction. The linear relation and similar slopes for both N/Fe-CNT sponge and Pt/C indicate the four-electron process, suggesting the efficient one-step ORR (O_2 + $4H^+ + 4e^- \rightarrow H_2O$).

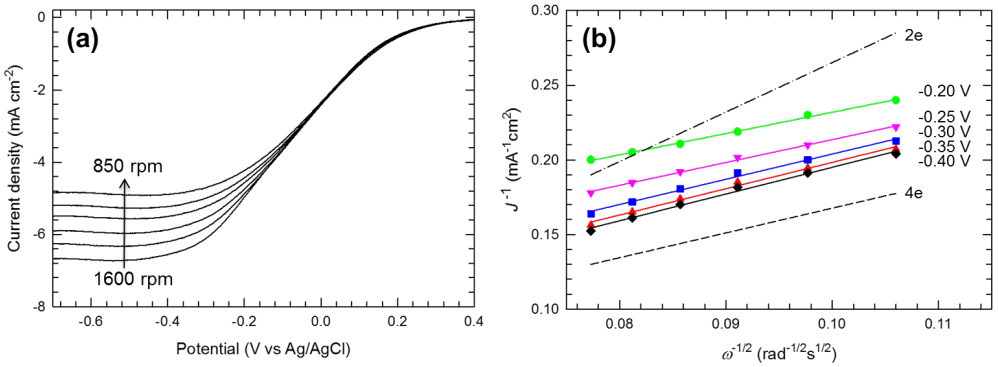

Figure 31 (a) RDE test results of Pt/C in O_2-saturated 50 mM PBS. The rotating speed was changed from 1600 to 850 rpm with 150 rpm interval. All data were recorded from 0.4 V to -0.7 V with a scan rate of 0.01 V s-1. (b) Koutecky-Levich plots of Pt/C, indicating the 4-electron ORR process.

We also investigated two important aspects on the practicability of our MFCs, which are long-term stability and material/manufacutring cost of cathode. Stability is one of the most important aspects, particularly for non-precious metal based ORR catalysts. To investigate the stability of N/Fe-CNT sponge, it was cycled between -0.5 V and 0.1 V for 20000 cycles followed by RDE test at 1000 rpm. The results are presented in Fig. 30d together with those from Pt/C for comparison. After 20000 cycles, the degradation of N/Fe-CNT was smaller than that of Pt/C, but both N/Fe-CNT and Pt/C were marginally degraded with similar limiting current densities and voltage shifts.

The high price of MFCs is a major hurdle for their wide deployment, mainly due to the prohibitive cost of Pt catalysts. Powdery Pt/C catalysts also require additional catalyst loading materials and processes, further increasing the manufacturing cost of MFC electrodes. Non-precious metal based catalysts such as nitrogen-doped graphene,[119] nitrogen-enriched Fe/Fe_3C-carbon nanorods,[120] and nitrogen-doped CNTs[103] typically involve complicated and long fabrication steps. Although their initial power generation performances are comparable to those of their Pt/C electrodes, these systems may not be practically viable. Here we compared the raw material costs of our N/Fe-CNT sponge and Pt/C (not including catalyst loading layer), as shown in Table 5. It is striking that the cost of 1g N/Fe-CNT sponge is only \$0.69, which is about 1.4% of 1g Pt/C (\$50 g^{-1}). Furthermore, it is much cheaper than previously reported alternative catalysts with comparable performances as that of Pt/C,[104, 120] to the best of our knowledge.

Table 5 Cost analysis and comparison of N/Fe-CNT sponge and commercial Pt/C.

N/Fe-CNT sponge			**Pt/C (10 wt% Pt with Vulcan XC-72 carbon) *****
Chemicals	**Amount**	**Cost**	**Cost**
Ferrocene, 99% ($335/2.5 kg) *	0.17 g	$ 0.023	$250/5g
C_2H_4, UHP ($225/300 ft^3) **	1.3 L (80 sccm × 16.7 min)	$ 0.036	
H_2, UHP ($45/300 ft^3) **	10.3 L (260 sccm × 16.7 min + 100 sccm × 60 min)	$ 0.055	
Ar, UHP ($48/300 ft^3) **	61.3 L (80 sccm × 16.7 min + 1000 sccm × 60 min)	$ 0.346	
Pyridine, 99+% ($757/25 L) *	25 mL	$ 0.757	
Total	Average N/Fe-CNT sponge yield: 1.77 g	$ 0.69 per gram of N/Fe-CNT sponge	$ 50 per gram of Pt/C

3.4 Conclusions

In summary, we have demonstrated a facile and low-cost method of synthesizing nitrogen/iron-coordinated CNTs in 3D sponge forms, which were directly used as self-standing cathodes for MFCs. The N/Fe coordination along with highly conductive porous CNTs resulted in high-power generation and long-term stability, which are comparable to those from Pt/C-based MFCs, demonstrating its potential as a promising alternative to expensive Pt/C loaded cathodes. We also found that the pore volume and cathode mass of the 3D sponges need to be optimized to maximize the performance, which may pave the way for future development of precious-metal-free self-standing cathodes for MFCs. The excellent MFC performances with the N/Fe-CNT sponge cathodes can be attributed to the efficient four-electron ORR process according to the Koutecky-Levich plots from the RDE tests as well as the high catalytic activity according to the CV results. The distinct features of our N/Fe-CNT sponges include self-standing characteristics suitable for cathode without conducting substrates (*e.g.*, carbon cloth/paper) or additional steps (*e.g.*, catalyst loading process), as well as considerably lower material/manufacturing costs with performances comparable to those of precious metal loaded MFCs. To the best of our knowledge, the synthesis cost of our N/Fe-CNT sponge is by far the lowest for MFC cathodes with performances similar to Pt/C loaded cathodes, which may bring MFCs and related fuel cell technologies one step closer to practical large-scale applications.

CHAPTER IV

TRAPPING POLYSULFIDES CATHOLYTE IN CARBON NANOFIBER SPONGES FOR IMPROVING THE PERFORMANCES OF SULFUR BATTERIES*

4.1 Introduction

Recent progresses in electrical vehicles and portable electronic devices brought strong desire to develop less expensive batteries with higher specific energy capacity, which has triggered the worldwide endeavor to investigate Li-S batteries. Recent investigation of Li-S batteries aims to replace the commercial lithium intercalation-based Li-ion batteries (LIB). Compared to the reversible insertion/extraction of less than one Li ion per transition metal ion by intercalation-based cathode materials (e.g. $LiCoO_2$), one sulfur atom can take up to two electrons together with two lithium ions ($S+2Li^++2e^- \leftrightarrow Li_2S$), yielding a capacity as high as 1672 mAh/g at an average redox potential of ~2.2 V (*vs*. Li/Li^+).[130-132] With the Li metal as anode, the theoretical energy density of a Li-S cell can be as high as 2567 Wh/kg, more than 6-fold higher than that of commercial Li-ion batteries (e.g. 387 Wh/kg of $LiCoO_2$/graphite battery).[133, 134]

Nonetheless, Li-S batteries have problems that should be addressed before they are viable for commercialization. First, due to the insulating nature of elemental sulfur and discharge products (e.g. Li_2S/Li_2S_2), large amount of inactive carbonaceous materials[132, 135, 136] or conductive polymers[137, 138] have to be added to lower the ohmic polarization.

---

* Reprinted with permission from X. Pu, G. Yang and C. H. Yu, *Journal of the Electrochemical Society*, 2015, **162**, A1396-A1400.

However, these inactive materials often significantly decrease the actual energy density based on the "total" weight of cathode. Second, irreversible sulfur during polysulfide shuttle between cathode and anode is known as a major cause of rapid capacity fading and low columbic efficiency.[131] For example, high-order lithium polysulfides (Li_2S_x, $4 \leq x \leq 8$) generated during discharge/charge cycles are highly soluble in the organic electrolyte, which diffuse to Li anode and then reduced to insoluble low-order lithium polysulfides. Active electrode materials are continuously consumed during the shuttle, resulting in low columbic efficiency and poor cycling life. Meanwhile, the deposition or aggregation of solid sulfur and/or Li_2S in cathode often makes the active materials inaccessible, deteriorating the cycling and rate performances.[139]

To solve these problems, various approaches have been proposed to trap solid sulfur in porous carbonaceous nanostructures;[135] to suppress the dissolution of polysulfides using concentrated electrolyte;[140] and to catch dissolved shuttle species using porous carbon interlayer.[132, 141] However, none of these approaches have completely prevented the dissolution and shuttling of polysulfides. Contrary to the strategy of avoiding the dissolution of polysulfides, liquid-type polysulfides-containing catholyte has been recently reported by our group and other research group as active materials.[142-145] Compared to the sluggish reaction associated with insulating solid-phase sulfur, dissolved polysulfides can alleviate the irreversible deposition of S or Li_2S at "dead" sites, and therefore offer a higher utilization of active materials.[145, 146] In addition, the use of synthetic polysulfides catholyte provides a more convenient sulfur loading method with a better control of sulfur/electrolyte ratio in a cell compared to traditional sulfur

impregnation[147]. In order to realize the new liquid-type sulfur batteries in practice, it is necessary to carry out in-depth research to better design catholyte reservoirs as well as unveil reaction mechanisms in cathode.

Herein, we presented a new method of the massive production of 3-dimensional (3D) free-standing networks of carbon nanofiber (CNF) sponges, which were then used as both catholyte reservoir and binder-free conductive framework in cathode of Li-S batteries. The unique microporous structure of the CNF sponge accommodated a large amount of catholyte as well as made intimate contacts with dissolved redox species in cathode. The reaction mechanism of Li-S batteries with liquid catholyte was investigated by the evolution of electrochemical impedance spectra at a series of different stages during the 1st charge/discharge cycle. High capacity and stable cycling were achieved for more than 300 cycles. Furthermore, the influence of catholyte concentration and loading volume on the battery performances was systematically investigated.

4.2 Experimental

4.2.1 Synthesis of catholyte

Polysulfide catholyte (Li_2S_6) was synthesized by directly reacting elemental sulfur with stoichiometric Li_2S in an electrolyte containing 1-M lithium bis(trifluoromethane) sulfonimide (LiTFSI) (Sigma Aldrich, 99.995%) and 0.5-M $LiNO_3$ (Alfa Aesar, 99.999%) in dioxolane:dimethoxyethane (DOL:DME) (1:1 by volume) (Alfa Aesar, 99%). Sulfur (Sigma Aldrich, 99.5%) and Li_2S (Sigma Aldrich, 99.98%) with a molar ratio of 5:1 were added into the electrolyte to make 2-M and 4-M Li_2S_6 catholytes (the molar concentrations were calculated based on sulfur). To fully dissolve sulfur and Li_2S, the mixture was heated

in an oil bath at 90 ^{o}C for 3 days with continuous stirring under Ar atmosphere. The final solution had a reddish color without noticeable sediment.

4.2.2 Synthesis of CNF sponges

Ferrocene (Sigma Aldrich, 98%) powder and C_2H_4 gas (99.999%) was used as a catalyst and a carbon source, respectively, for a "one-step" chemical vapor deposition (CVD) process so as to produce a long 3D CNF sponge (Fig. 32a). The synthesis was conducted in a quartz tube (1 inch in diameter) with a 3-zone furnace (Lindberg/Blue M STF55346C). The temperatures of the first and third zone were set at 120 ^{o}C and 650 ^{o}C, respectively. The ferrocene powder was placed in the middle of the first zone. The temperature of the third zone was raised to 650 ^{o}C in 20 min with 100-sccm Ar (99.999%). After reaching 650 ^{o}C, the Ar flow was switched to a line passing through a water bubbler to introduce moisture for promoting the growth of the fiber,[148, 149] and H_2 and C_2H_4 (260 and 80 sccm respectively) were added. After a 30-min growth process, the furnace was naturally cooled down to room temperature, and then a large quantity of ~1.4 g of CNF sponge, as shown in Fig. 32a, was collected.

4.2.3 Testing and characterization of battery cells

Fig. 32b illustrates design of the sulfur battery with a CNF sponge soaked with polysulfide catholyte as cathode and Li metal as anode. 2032-type coin cells were assembled for testing the battery performances. First, Li metal foil was wetted with a drop (~10 μL) of the electrolyte (1-M LiTFSI + 0.5-M $LiNO_3$ in DOL:DME (1:1 by vol.)), and then a Celgard2400 separator was placed on top of the Li foil. Subsequently, the CNF sponge with a thickness of ~1 mm (areal loading was ~4.6 mg/cm^2) was placed on top of

the separator and then 2.5~10-μL of the 2-M or 4-M catholyte per milligram of the CNF sponge was dropped to soak the sponge. The weight percentage of sulfur in cathode was calculated by ($mass_{sulfur\ in\ catholyte}$)/($mass_{sulfur\ in\ catholyte}$ + $mass_{cnf}$), which is equivalent to sulfur loading wt% used for typical solid sulfur cells (i.e., mass of sulfur divided by combined mass of sulfur, conductive additives, and binders). For 24-wt% sulfur, 5 μL/mg_{cnf} of 2-M catholyte or 2.5 μL/mg_{cnf} of 4-M catholyte were used; for 40 wt% sulfur, 10 μL/mg_{cnf} of 2-M catholyte or 5 μL/mg_{cnf} of 4-M catholyte were used. The cells were cycled between 1.7~3 V at 800 mA/g_{sulfur} using Arbin BT2000 galvanostat. The electrochemical impedance spectra were measured using an electrochemical workstation (CHI 604D) at seven different stages in the first discharge/charge cycle of a cell with 5-μL/ mg_{cnf} loading of 2-M catholyte. The ionic conductivity of the catholyte was measured by using a miniature dip-in conductivity probe (eDAQ ET915). Microstructures were characterized by using a scanning electron microscope (SEM) (JEOL JSM-7500F) and a transmission electron microscope (TEM) (JEOL JEM-2010).

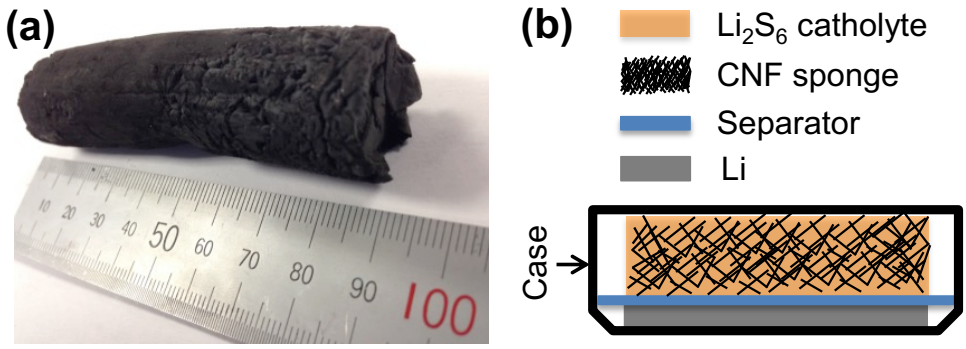

Figure 32 (a) A photograph of a CNF synthesized by using a facile one-step CVD method. (b) Schematic illustration of the Li-S battery with a CNF sponge as a reservoir of liquid-type polysulfides. The CNF sponge eliminated binders and a current collector.

4.3 Results and discussions

4.3.1 Microstructure of CNF sponge

Our CNF sponges feature randomly entangled porous CNF networks without using any surfactant or after-treatment (see as-synthesized CNF shown in Fig. 33a), providing a facile and easy way for a scale-up process to fabricate conductive frameworks. In contrast, it is difficult to make such 3D structures with typical mass-produced CNFs or carbon nanotubes due to the difficulties in separating their bundles and assembling them into porous networks. In addition, a large amount of surfactants are typically required for the separation, which may severely decrease electrical conductivity and porosity due to the presence of surfactants or their residues.[150-154] According to the TEM images shown in Fig. 33b, the diameter of the CNF is 150~200 nm. The graphitic layers of the CNF can be observed from the high resolution TEM, as shown in Fig. 33c.

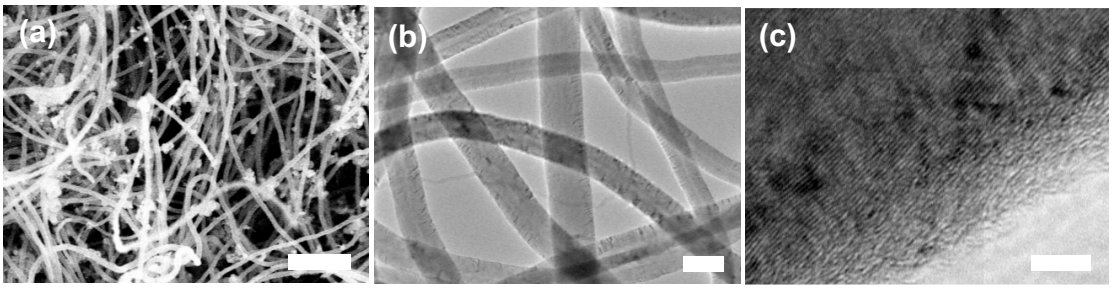

Figure 33 SEM (a) and TEM (b) images of the CNF sponge. (c) A high resolution TEM image of a CNF, showing graphitic layers of the CNF. The scale bars indicate 2 μm for (a), 200 nm for (b), and 5 nm for (c).

4.3.2 Impedance study to reveal working mechanism

In order to understand the working mechanism of our sulfur batteries, electrochemical impedance spectroscopy of a cell with 5 $\mu L/mg_{cnf}$ of 2-M catholyte was

carried out between 10^{-2}~10^{5} Hz at seven different charge/discharge stages during the first cycle. Fig. 34a shows the charge/discharge profiles of the cell. The small sharp peaks came from the interruption of galvanostatic test for the impedance measurement. The open circuit voltage of the cell was ~2.3 V. The first discharge corresponds to the reduction of Li_2S_6 to Li_2S, and shows a single voltage plateau around 2.1 V, due to the absence of the reduction reaction of S to Li_2S_6. After the cell was discharged to 1.7 V, the subsequent charge shows a much higher capacity since the corresponding reaction is an oxidation reaction from Li_2S to S.

The evolution of impedance spectra corresponding to the seven different stages (see Fig. 34a) is shown in Fig. 34b. For all the spectra, two semi-circles at high and medium frequencies, and a sloping line at low frequencies were observed from the Nyquist plots. A model of equivalent circuit was presented in the inset of Fig. 34a. The high-frequency semicircle is related to the contact resistance (the diameter of the semicircle, R_f) and constant phase element of the CNF/electrolyte interface (CPE1); the medium-frequency semicircle corresponds to the charge-transfer resistance (R_{ct}) and constant phase element at solid/electrolyte interface (CPE2); the smallest value on the real axis is the electrolyte resistance (R_s); and Z_w is the Warburg impedance of the lithium diffusion in solid phase, which corresponds to the slope of the inclined line.[155]

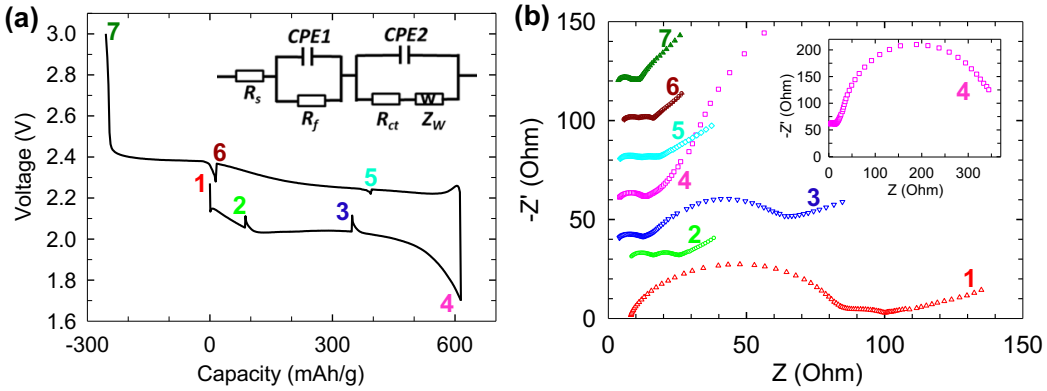

Figure 34 (a) The discharge/charge profiles of the first cycle of a cell with 5 μL/mg_{cnf} of 2-M catholyte at 0.5-C rate. The numbers correspond to the points where the impedance spectra were taken. The inset in (a) shows an equivalent circuit model of the impedance test. (b) Impedance spectra recorded at the seven different stages as indicated accordingly in the profile of (a). The inset in (b) shows the full spectroscopy at stage 4.

As shown in Fig. 34b and Table 6, R_{ct} (*i.e.*, the charge transfer resistance) was gradually increased from stage 1 (2.0 Ohm) to stage 4 (343.2 Ohm), which corresponds to the discharge process that converts the soluble Li_2S_6 to insoluble Li_2S_2/Li_2S. We believe the electrically insulating Li_2S/Li_2S_2 was deposited on the CNF, raising the charge transfer resistance. The large charge transfer resistance at the discharged state indicates that deposited solid Li_2S_2/Li_2S considerably deteriorates the kinetics of the cell. Upon charging, R_{ct} at stage 5 became small, suggesting a quick reversible oxidation of Li_2S_2/Li_2S back to soluble high-order polysulfides, which is also consistent with recent findings.[156] From stage 5 to stage 7, the slope (|Z'/Z|) of the linear line at low frequencies was slightly enlarged (Fig. 34b), confirming the deposition of solid sulfur on the CNF. Although insulating sulfur is dominantly present on cathode as a result of de-lithiation of the lithium polysulfide at the fully charged state (stage 7), we observed that R_{ct} at stage 7 is

comparable to those at the stages with soluble polysulfides, which could be ascribed to uniformly distributed sulfur on the large surface areas of the porous sponge cathode.

Table 6 Charge-transfer resistances (R_{ct}), contact resistance (R_f) and electrolyte resistance (R_s) of a cell with 5 μL/ mg_{cnf} of 2-M catholyte loading at different stages in the first cycle.

Stage	R_{ct} (Ohm)	R_f (Ohm)	R_s (Ohm)
1	2.0	76.8	8.2
2	9.0	7.4	8.6
3	52.2	7.8	4.0
4	343.2	2.7	4.1
5	6.0	6.7	4.3
6	4.1	5.2	5.8
7	2.0	4.4	3.6

The electrolyte resistance (R_s) is also related to the conversion reactions between Li_2S_2/Li_2S and soluble polysulfides. According to our measurements and literature,[157] highly concentrated catholyte has smaller ionic conductivity and thus higher R_s, due to the increased viscosity. For example, the ionic conductivity values of catholyte at three different concentrations (0, 2, and 4 M) of Li_2S_6 were measured to be 10.7, 6.6, and 4.0 mS/cm, respectively. From stage 1 to stage 2, R_s was not significantly changed, indicating almost unchanged catholyte concentrations. On the other hand, at stage 3 and 4, R_s was reduced to only about a half of the value at stage 1 (see Table 6), suggesting that the deposition of solid Li_2S_2/Li_2S on the CNF framework lessened the polysulfide

concentration in the electrolyte. As for the charge process, the reaction would occur in the following sequence: deposited Li_2S_2/Li_2S, soluble polysulfides, and solid sulfur, which could result in an increase of R_s from stage 4 (4.1 Ohm) to stage 6 (5.8 Ohm) followed by a decrease to 3.6 Ohm at stage 7. Clearly, the charge/discharge of a sulfur battery is a process of repeated dissolution/deposition of the redox species. Therefore, the design of appropriate "container" to trap these redox species (i.e. polysulfides) in cathode is essential to improve the performances of sulfur batteries. In a typical Li-S cell with solid sulfur in cathode, the weight percentage of sulfur determines energy density and cycling performance. For instance, the energy density increases by raising sulfur loading that depends on the specific surface area, pore volume and size of conductive carbonaceous materials.[158] In our liquid-type cell, the concentration and volume of catholyte, which determine sulfur loading, are major parameters to optimize capacity and cycling performance. We used two different concentrations of catholyte (2 M and 4 M based on sulfur atom), and their volumes were varied to achieve 24 wt% and 40 wt% of sulfur in cathode.

4.3.3 Electrochemical performances of catholyte sulfur batteries

Fig. 35a shows the charge/discharge profiles of the first two cycles of the four different cells. The typical voltage plateau at 2.3 V is absent during the first discharge due to the starting reaction from Li_2S_6, but it appeared during the second cycle, increasing the capacity. An increase of the 2-M catholyte volume from 5 $\mu L/mg_{cnf}$ to 10 $\mu L/mg_{cnf}$ decreased the specific capacity significantly, which indicates the extra sulfur was not fully utilized. We also observed that the 4-M catholyte delivered higher capacities compared to

the 2-M catholyte (Fig. 35a) when the sulfur loading is the same (*e.g.*, 2.5 μL/mg_{cnf} of 4-M catholyte *vs.* 5 μL/mg_{cnf} of 2-M catholyte). We believe the larger volume of 2-M catholyte made the diffusion distance of polysulfides and Li ions longer (further evidence is presented in discussion of Fig. 36), resulting in the lower capacities. On the other hand, when the catholyte volume is the same (5 μL/mg_{cnf}), the 2-M catholyte shows a higher specific capacity presumably due to the higher ionic conductivity of the dilute catholyte and a smaller amount of insulating charge/discharge products on the CNFs. These effects of catholyte concentration and volume on the performances are consistent with those of Li-S batteries with solid cathode,[159] where solid sulfur/liquid electrolyte ratio was the key to get reproducible data. Compared to our previous work,[145] the diameter of the carbon scaffold made in this work is larger, which might explain its lower sulfur loading capability.

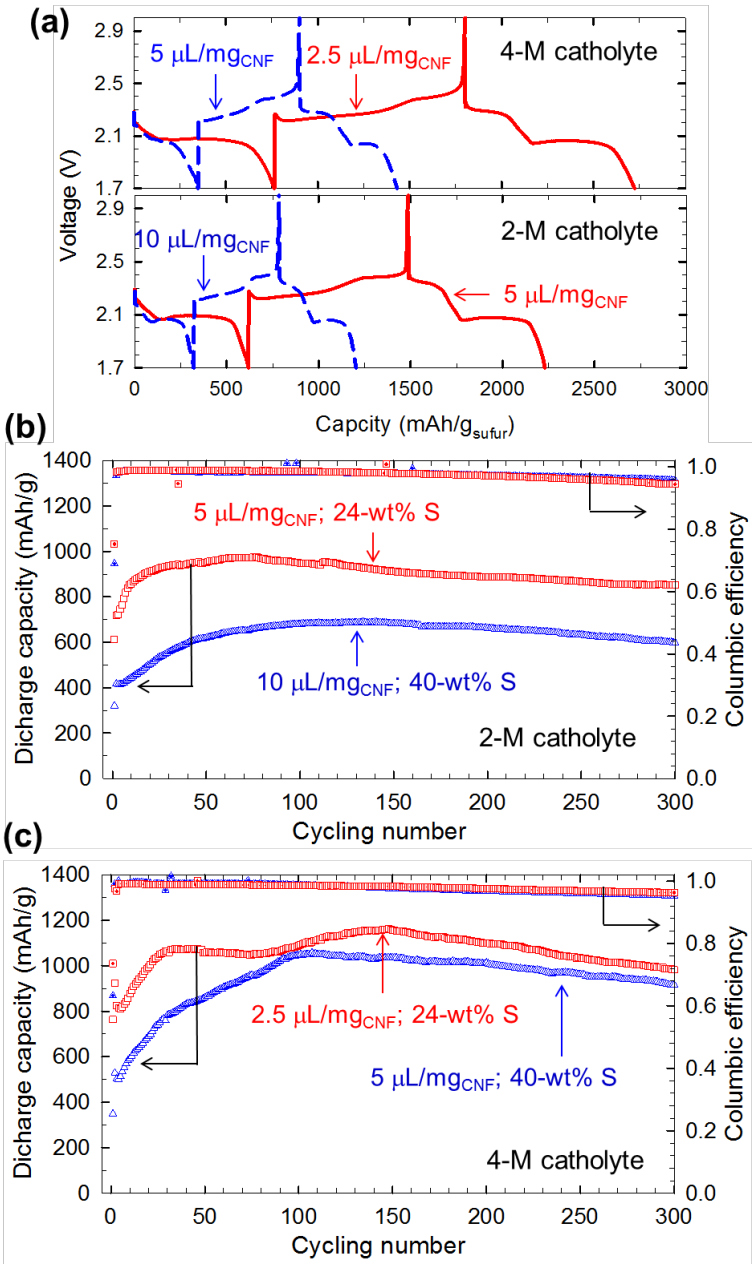

Figure 35 (a) Discharge/charge profiles of the first two cycles at 0.5-C rate when different catholyte concentrations and loadings were used. Cycling performances at 0.5 C when the catholyte concentration is 2 M (b) and 4 M (c).

Fig. 35b and c respectively display the cycling performances of cells with 2-M catholyte and 4-M catholyte at 800 mA/g_{sulfur}. The relatively low initial specific capacity

was continuously increased to a saturation point in the following cycles, which could be owing to the improved uniformity of polysulfides in the CNF framework. The polysulfides would not be uniformly distributed at the beginning since we simply dropped catholyte on the CNF framework for the preparation of cathode. Upon cycling, repeated dissolution and deposition of these reactive species are likely to redistribute polysulfides throughout the cathode. The longer cycles to reach the saturation point for the 4-M catholyte compared with the 2-M catholyte may have caused by delayed diffusion of polysulfides due to the higher viscosity and the lower ionic conductivity.

The maximum discharge capacities, 974 and 688 mAh/g respectively with 5 and 10 $\mu L/mg_{cnf}$ of 2-M catholyte were slightly reduced to 852 mAh/g (88%) and 598 mAh/g (87%), respectively, at the 300^{th} cycle. As for 4-M catholyte, higher maximum capacities – 1160 mAh/g and 1020 mAh/g respectively for 2.5-$\mu L/mg_{cnf}$ and 5-$\mu L/mg_{cnf}$ catholyte – were achieved. At the 300^{th} cycle, the corresponding capacity retention was 79% and 91%, respectively. The columbic efficiencies of the four cells throughout the whole cycling except the first cycle were all above 95%.

It should be noted that neither polymer binder nor Al current collector was used in our cells. Both of them are generally required for Li-S and other Li-ion batteries, but they are typically not considered for calculating the specific capacity. Considering this, the sulfur loading weight used in our measurement is comparable to, if not better than, most of reported sulfur wt% in conventional thin film electrodes, where the weights of current collector, conducting additives, and polymer binder should be considered for fair comparison.

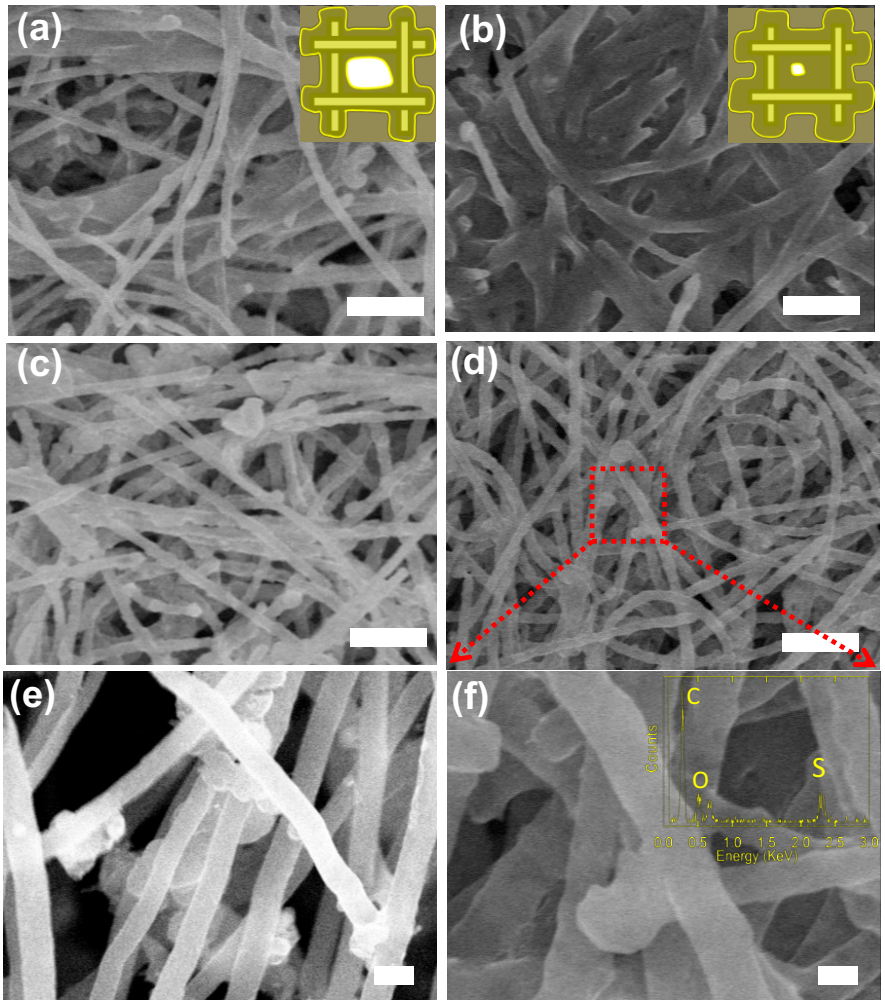

Figure 36 SEM images of CNF sponges after 300 cycles. As-disassembled sponges with 2.5 μL/mg_{cnf} of 4-M catholyte loading (a) and 5 μL/mg_{cnf} of 2-M catholyte loading (b). The insets in (a) and (b) show the higher loading volume (5 μL/mg_{cnf}, b) gives sulfur longer diffusion distance to reach the CNF networks. The disassembled sponges with 2.5 μL/mg_{cnf} of 4-M catholyte loading (c) and 5 μL/mg_{cnf} of 2-M catholyte loading (d) "after washing" with ample DOL. It is clear that the diameter of the as-grown CNF sponge (e) is smaller than that of the CNF sponge (f) after the cycling test with the washing process. The inset in (f) is the EDS spectra of the whole image in (f), indicating the uniform deposition of sulfur at the charged state. The scale bars in (a)~(d) indicate 2 μm, and those for (e) and (f) indicate 200 nm.

Fig. 36a and b respectively show SEM images of the as-dried CNF sponges disassembled from the cells with 2.5 μL/mg_{cnf} of 4-M and 5 μL/mg_{cnf} of 2-M catholyte

(both have 24-wt% sulfur) after 300 cycles at the charged state (no washing process). The amount of residual lithium salts would indicate the catholyte volume, suggesting a longer diffusion distance for the 5-μL/mg_{cnf} case, as illustrated in Fig. 36a and b. After washing away the residual lithium salts with a plenty of DOL, we observed that the porous structures of the CNF sponges were maintained without noticeable aggregation of solid sulfur, as shown in Fig. 36c and d. When the CNFs at the charged state (Fig. 36f) was compared with the pristine CNFs (Fig. 36e), we observed an increase in the diameter of the CNFs due to sulfur as confirmed with the energy dispersive spectroscopy (EDS) spectra (inset of Fig. 36f). The uniform deposition of sulfur on the surface of CNF is likely to be the reason for the stable cycling performances.

4.4 Conclusions

CNF sponges were employed as a polysulfide catholyte reservoir as well as a self-standing conductive framework, eliminating a current collector and binders in cathode. By optimizing the catholyte concentrations and loading volumes, we have achieved a highly stable cycling performance with capacity retention higher than 90% at 800 mA/g_{sulfur} for 300 cycles. According to the impedance spectra during the first discharge/charge cycle along with electron microscopy images, sulfur was uniformly deposited on the entire surface of CNFs at the fully charged state, and solid Li_2S_2/Li_2S deposition at the fully discharged state deteriorated the kinetics. We believe the polysulfides were redistributed during deposition and dissolution processes during cycling, and the large surface area of the CNF framework served as a reservoir to alleviate the polysulfide shuttle. The facile scalable one-step synthesis process of the CNF sponges with inexpensive raw materials

used in our sulfur batteries will be helpful for developing practically viable Li-S batteries in the near future.

CHAPTER V

TRENCH-WALL CARBON NANOTUBE SPONGES AS STABLE AND EFFICIENT SULFUR/LITHIUM DUAL HOST FOR HIGH AREAL CAPACITY BATTERIES

5.1 Introduction

Considering the increasing demand for low-cost and efficient energy storage solutions, the importance of the developing energy storage systems with high energy density cannot be overstated.[160, 161] Since their first appearance in the market, Li-ion batteries have been widely adopted in portable electronics and recently in electric vehicles.[162] Although extensive efforts have been made to achieve their theoretical limit of energy storage, the fully developed Li-ion batteries cannot satisfy large-scale applications like transportation and stationary energy storage.[39, 163, 164] New chemistry and materials have been explored beyond the horizon of traditional Li-ion batteries.[165] On the cathode side, conversion chemistry has shown a promise to replace the intercalation chemistry of traditional Li-ion batteries. Conversion-type cathode materials like sulfur and oxygen can provide 2567 Wh kg^{-1} and 3505 Wh kg^{-1}, respectively, energy storage, compared to that of intercalation-type cathode $LiCoO_2$ (387 Wh kg^{-1}).[166] Research on Li-S batteries began in the 1940s and has attracted a rapidly increasing attention since the pioneer work published by Nazar's group in 2009.[43] Substantial progress has been made and reported to solve inherent Li-S battery issues like lithium polysulfide dissolution and shuttle, insulating nature of the end-products, and sulfur cathode volume variation during cycling.[167-169] As a result, the specific capacity and cycling performance have been

markedly improved, showing a high promise for real applications. However, it is worth noting that a low areal loading of sulfur (active material) has negated the high-energy-density merit of Li-S batteries but helped to beautify researchers' results by showing the energy density based on the mass of sulfur only (not whole cathode or battery pack). Therefore the actual energy density of the "cell" or "battery pack" has not been improved. To have high "cell-level" energy density, the areal loading of sulfur has to be increased to ~10 mg/cm^2 or higher from the literature values (typically ~1 mg/cm^2 and a few of them reaching up to 3 mg/cm^2).[170-173]

Here we report a 3D CNT based framework with unique trench-wall feature on CNTs, acting as a stable and efficient dual host for both sulfur and lithium metal. The characteristic trench-wall CNTs provide nano-reactors for sulfur with high loadings at the cathode, enabling enough reactive surface/space to achieve high areal capacity. Through a mechano-chemical treatment, the surface is also functionalized with –COOH groups, converting the inert pristine carbon surface to polysulfide-philic and lithiophilic surface. It demonstrated a considerable improvement on immobilizing polysulfide even at a high sulfur loading. Through a thermal infusion method, Li was infiltrated and hosted by the 3D framework. The highly porous "host" would not only provide a favorable surface for lithium deposition but also enough space to accommodate the lithium plating and stripping, resulting in stable cycling and reduced overpotential. Thanks to the unique features of sulfur/lithium dual host, exceptional cycling performance has been achieved with, to our best knowledge, the best areal capacity retention (10 mAh cm^{-2}) after 100

cycles at a high current density of 5 mA cm^{-2}, bringing the Li-S batteries one step further to practical applications for high energy storage.

5.2 Experimental

5.2.1 Preparation of sandwich-type cathodes

The synthesis of MC-CNT starts from CNT sponge, which has been developed and reported by our group[174]. After cutting a thin (~1 mm) piece of CNT sponge, a mechanochemical method was used to create trenched wall structure on CNT sponge. A chemical solution prepared by dissolving $KMnO_4$ (AMRESCO) in sulfuric acid (BDH Chemicals, ACS Grade) was used as the exfoliating agent. The amounts of $KMnO_4$ and sulfuric acid are controlled based on the weight of CNT sponge to be treated. The weight ratio of $KMnO_4$ to CNT sponge was 1:2, and the concentration of exfoliating agent was kept at 0.5 g ml^{-1}. The mechano-chemical process was performed with a typical vacuum filtration set by adding the exfoliating agent dropwise on top of the CNT sponge placed on the glass filter, while maintaining a vacuum condition underneath. The vacuum level was controlled to obtain different levels of trench-like feature (MC-CNT-L, MC-CNT-H, MC-CNT-UH). Enough DI water was used to rinse the MC-CNT to get rid of residual $KMnO_4$ and H_2SO_4 after the mechano-chemical process, followed by rinsing with ethanol (EMD Millipore, 95%) and drying at 80^oC overnight.

5.2.2 Preparation of molten Li infused CNT and MC-CNT anodes

The whole fabrication process was performed in the glovebox filled with argon gas. Oxygen and moisture levels were monitored and kept under 1 ppm. A piece of lithium metal (Alfa Aesar, 99.9%) was cut and placed on top of a stainless steel sheet which was

on a hot plate with temperature controller. The temperature of the hot plate temperature was set to 350^{o}C during the infusion process. After lithium melting, a piece of CNT or MC-CNT was put in contact with the molten lithium to start the infusion process. The process was stopped by keeping them separated when CNT or MC-CNT was fully covered with Li.

5.2.3 Materials characterization

Structural investigation was carried out using scanning electron microscopy (FEI Quanta 600) with energy dispersive spectroscopy (Oxford) and high-resolution transmission electron microscopy (FEI Tecnai G2 F20 ST FE-TEM). Chemical composition was obtained with X-ray photoelectron spectroscopy (Omicron XPS/UPS system with Argus detector, Mg Kα as the X-ray source). Chemical bond characteristics were inspected by Fourier transform infrared spectroscopy (FTIR). Raman spectroscopy was utilized to inspect the bond change after different treatments. The interaction between polysulfides and different cathode materials was studied by ultraviolet–visible spectroscopy (UV-Vis).

5.2.4 Coin cell assembly and test

2032 coin-type cells (MTI) were assembled in the Ar-filled glovebox. The anode was pure lithium metal (Alfa Aesar, 99.9%) or molten lithium infused CNT or MC-CNT. The cathode was sandwich-type sulfur cathode. A piece of separator (Celgard 2400) was inserted between the cathode and anode to avoid short circuit. The battery tests were performed on Arbin BT2000 or Landt CT2001 galvanostat.

5.3 Results and discussions

5.3.1 Mechano-chemical preparation of trench-wall CNT

Self-standing CNT sponge structures (Fig. 37a) have been reported to effectively improve the Li-S battery performance by serving as a three-dimensional (3D) electronic and ionic conductive framework and withholding polysulfide solution.[132, 175] Nevertheless, its pristine graphitic surface is not polysulfide-philic, therefore the prevention of polysulfide shuttle relies solely on physisorption mechanism (Fig. 37b, c). This would remain as an effective way, provided the areal loading of sulfur is low e.g. < 3 mg cm^{-2}. A high areal loading of sulfur requires large and favorable surface to promote the complete reaction of active materials as well as additional chemisorption mechanism to impede shuttle resulted from the increased amount of polysulfide.

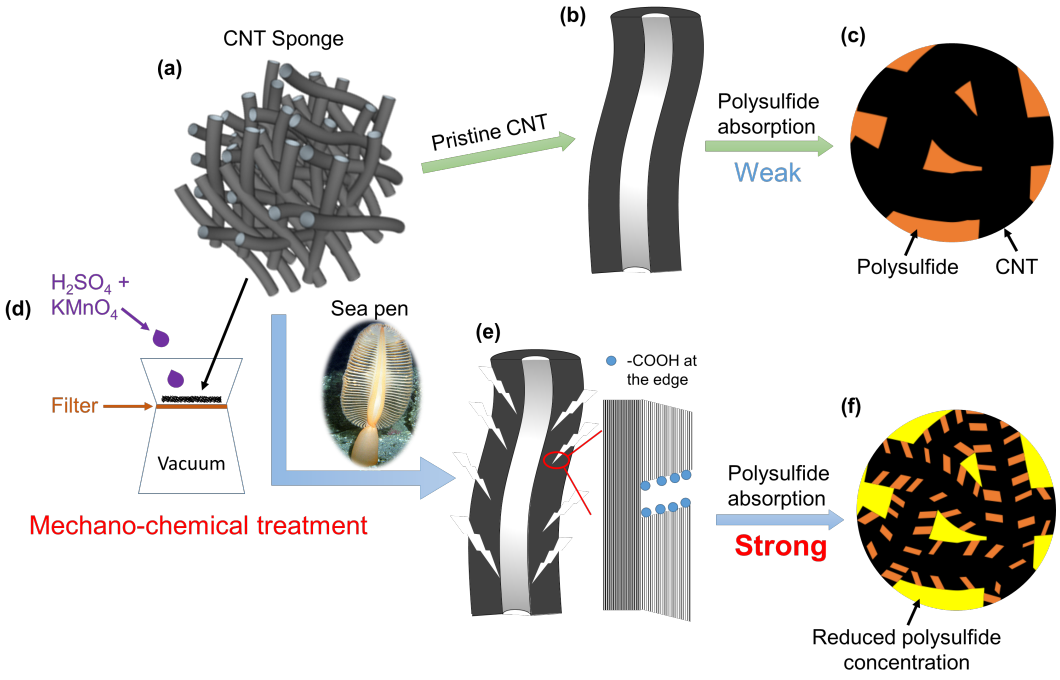

Figure 37 Illustration of the synthesis of trenched-wall CNT sponge and its favorable polysulfie absorption.

Inspired by a colonial marine animal – sea pen (Fig. 37 inset) with multiple polyps, we intentionally create trench-like structure on the wall of CNTs through a mechano-chemical method (Fig. 37d). The highly oxidative nature of the exfoliating agent made with $KMnO_4$ and H_2SO_4 tends to break the carbon-carbon bond of graphitic layers, leaving carboxyl groups at the edge of layers.[176] During the bond cleavage process, additional mechanical force created by pressure difference between two sides of the CNT sponge was applied to assist the penetration of exfoliating agent. The mechano-chemical treatment eventually gave rise to a unique trench-wall CNT structure (Fig. 37e). Compare to pristine CNT structure, the surface of trench-wall CNT turns to polysulfide-philic and lithiophilic (Fig. 37f) because of the affinity between polysulfide/lithium and the oxidized surface especially within the trench area. The trench would also provide physically enough surface area and serve as nano-reactor to promote the complete reaction of active materials, which is of vital importance in the high areal loading scenario.

5.3.2 Microstructure of trench-wall CNT

Fig. 38a and b show the low-magnification and high-resolution TEM images, respectively, of a CNT from pristine CNT sponge (P-CNT). It exhibits a hollow tubular structure with wall consisting of multiple well-ordered graphitic layers. Fig. 38c shows the microstructure of the CNT with chemical treatment only (C-CNT, see details in experimental section). It can be found that after chemical treatment the surface became rough, which is believed to originate from the oxidation of a few surface layers (5-10 nm from the outermost layer). The inner layers remain intact and there is no trench-like feature on the wall. After applying additional mechanical force simultaneously with the chemical

exfoliating agent, the unique trench-like structure appears (Fig. 38d). MC-CNT-H denotes the CNTs were mechano-chemically treated and with a high vacuum pressure underneath the filter (Fig 1d). We suppose the exfoliating agent is forced to penetrate into the inner walls of CNTs by breaking the relatively weak carbon-carbon bonds along the path, leaving trench-like microstructure on the wall. This process is likely stopped with the gradually reduced bond breaking or oxidative capability of the exfoliating agent at the penetration front. To verify our hypothesis, we altered the applied force by changing the vacuum level. We found that the extent of trench feature can be controlled by the applied force or vacuum level. When the force/vacuum is low (MC-CNT-L), narrow trenches (~5 nm wide) were formed on the walls and the surface graphitic layers became disordered (Fig. 39a). Fig 2e and d are high-resolution images of a specific trench and the surface of mechano-chemical treated CNTs with high vacuum (MC-CNT-H), respectively. Within the trench area, the strong exfoliation effect generates nanoribbons within the 30~40 nm wide trench. Compared to the surface of C-CNT and MC-CNT-L, the surface of MC-CNT is not only much more disordered but also exfoliated. These features would play essential roles in hosting large amount of polysulfide and lithium, and assisting electrochemical reactions. When the vacuum level was increased to an ultra-high level (MC-CNT-UH), the resulted trench-like structure was more pronounced with enlarged trenches (Fig. 39b). It is also noticed that the surface of MC-CNT-UH (Fig. 39c) was smoother than the lower vacuum treated counterparts MC-CNT-L and MC-CNT-H. This could be attributed to the large force brought by the ultra-high vacuum, which may “wash away” the exfoliated nanoribbons.

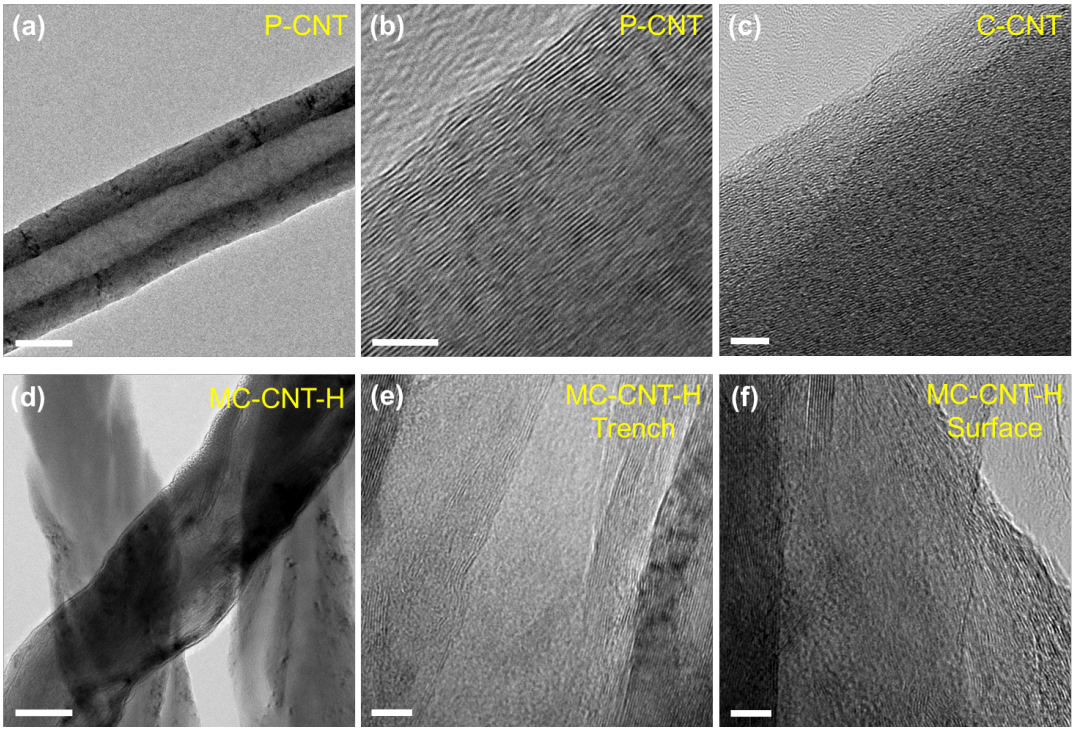

Figure 38 Microstructure of pristine CNT, chemically treated CNT, and mechano-chemical treated CNT.

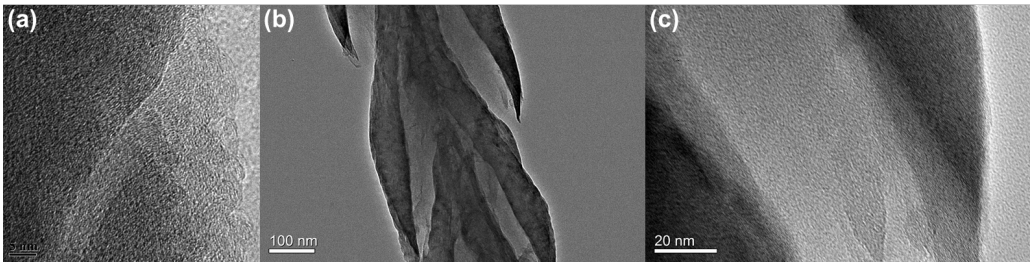

Figure 39 TEM images of trench-wall CNT with low vacuum (a), and ultra-high vacuum (b)(c).

5.3.3 Electrochemical performances

In order to fabricate a high sulfur loading cathode, we developed a sandwich-type cathode with active sulfur powder being sandwiched and then pressed between two pieces of CNT sponges. This is a facile method of making high areal loading sulfur cathodes

without any normally utilized and complicated sulfur thermal infusion procedures, indicating its manufacture-friendliness. The anode was prepared by thermally infusing lithium into MC-CNT-H. The molten lithium can spontaneously infuse into the MC-CNT-H because (1) the structure is highly porous to accommodate enough lithium; (2) the surface has a high affinity with lithium owing to the high binding energy between lithium and carbonyl groups[177]; (3) the nano-sized trench-like structure generated capillary force promoting the intake of molten lithium. The 2032 coin cell type Li-S batteries were assembled with different cathode and anode configurations to test their electrochemical performances. The cathodes were all sandwich-type with the same areal loading of sulfur (10 mg cm^{-2}) and the anodes were either pure lithium metal or lithium infused MC-CNT-H (Li@MC-CNT-H). The cycling performances were compared in Fig. 40a. The best performance was observed in the cell with sulfur sandwiched between two pieces of MC-CNT-H (S@MC-CNT-H) as cathode and Li@MC-CNT-H as anode. It demonstrated an areal capacity of 12.1 mAh cm^{-2} at the beginning and a stable cycling for more than 250 cycles at a high current density of 4.8 mA cm^{-2}. None of the other cells can survive more than 170 cycles under this harsh cycling condition. The prominent cycling performance improvement can be ascribed to the synergetic effects of the superior sulfur/lithium dual host. To get the root of it, we conducted electrochemical impedance (EIS) analysis of three cells at their 10th and 50th cycles and the corresponding Nyquist plots are compared in Fig. 40b. For all plots, the semicircle indicates the combined interfacial resistance and charge transfer resistance at both cathode and anode sides.[178-181] The positive cathode effect of using MC-CNT-H can be seen by comparing the spectra from S@P-CNT / Li

and S@MC-CNT-H / Li, since they have the same lithium metal anode. At the 10th cycle, S@P-CNT / Li showed a large combined resistance of ~310 Ω compared that of S@MC-CNT-H / Li (~82 Ω), suggesting a closer interaction and more favorable charge transfer between the surface of MC-CNT-H and the polysulfide. There is also a noticeable increase in the electrolyte resistance, represented by the intercept on the real axis at high frequency region, from 10th to 50th cycle. The increasing electrolyte resistance can be explained by the increasing polysulfide concentration in the electrolyte.[175] For S@P-CNT / Li, the increase is ~51 Ω, which is higher than that of S@MC-CNT-H / Li (~18 Ω). The limited polysulfide dissolution from the S@MC-CNT-H cathode is evidence of its high polysulfide absorbing capability, which will be discussed in the later section. On the other hand, the favorable anode effect of MC-CNT-H can be found by comparing the spectra from S@MC-CNT-H / Li and S@MC-CNT-H / Li@MC-CNT-H. Since the cathodes are same, any differences in performance is supposed to originate from the anode side. A marked decrease in the combined interfacial and charge transfer resistance was observed when changing the anode from pure lithium metal to lithium infused MC-CNT-H, corresponding to the surface condition change from non-lithiophilic to lithiophilic. The reduced resistance would further relate to better lithium depositing and stripping kinetics. Besides, it is worth noting that the combined interfacial and charge transfer resistance of S@MC-CNT-H / Li@MC-CNT-H remained almost identical with the initial value after 50 cycles, demonstrating its superior stability. The improved kinetics and stability at both cathode and anode sides brought by the sulfur/lithium dual host would contribute to the outstanding performance even at extremely high current density (Fig. 40c). The S@C-

CNT was used as the control, which showed a relatively low areal capacity at low current density and a noticeable degradation when cycled at large current density. Replacing the cathode with S@MC-CNT-L did effectively improve the delivered areal capacity at lower current density (i.e. 1.6 mA cm^{-2} and 3.2 mA cm^{-2}) because of the more favorable cathode surface condition promoting the electrochemical reaction at the interface. However, the rapid drop on areal capacity was seen when increasing the current density to 8.0 mA cm^{-2} and 16 mA cm^{-2}. This is further largely improved, especially at high current density, when S@MC-CNT-H was used as the cathode, indicating the widening of trenches on CNT walls from ~5 nm to ~40 nm would help to create enough and effective nano-reactors necessitated in the high areal loading scenario. The best high rate performance was observed when MC-CNT-H was used as a dual host (S@MC-CNT-H / Li@MC-CNT-H). A high areal capacity of 13.3 mAh cm^{-2} was delivered at low current density, and more importantly it showed little degradation when gradually increase the current density. It demonstrated an areal capacity of 10.9 mAh cm^{-2} at the extremely high current density of 16 mA cm^{-2}, which to our best knowledge is the highest areal capacity at this high rate. We attribute the outstanding performance to the synergetic improvement on reaction kinetics at both cathode and anode caused by MC-CNT-H. This is clear exhibiting on the charge/discharge profiles (Fig. 40d). At high current density, a large overpotential is usually expected and it become even larger when the areal loading is high, since the reaction will be limited by effectiveness of electron transfer between the conducting and active electrode surface and the electrochemically active materials. The large overpotentials displayed by S@C-CNT / Li, S@MC-CNT-L / Li, and S@MC-CNT-H /

Li mean poor reaction kinetics resulted from insufficient active surface area and unfavorable surface conditions for lithium deposition/stripping. By increasing active surface area through exfoliation of graphitic layers and creation of effective nano-reactors, and improving lithium deposition/stripping by creating lithiophilic surface, a striking reduction on overpotential was found on the charge/discharge profile of S@MC-CNT-H / Li@MC-CNT-H.

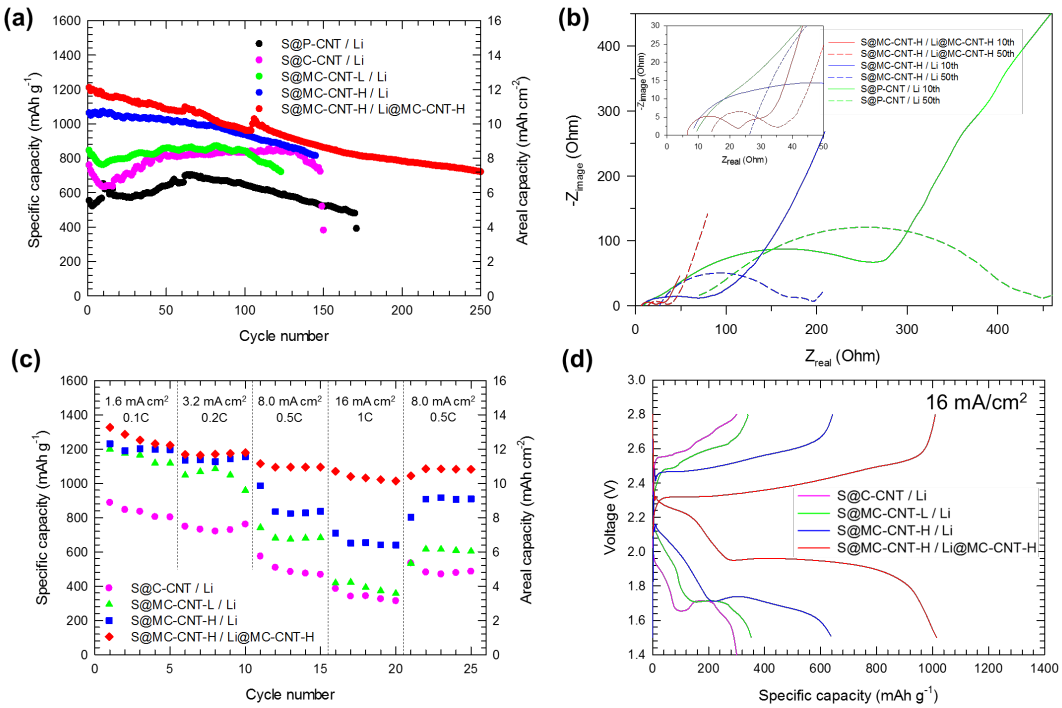

Figure 40 Electrochemical performance of different Li-S cells.

For practical applications, the areal capacity delivered at high cycling rate is much more important than the specific capacity (based on active material e.g. sulfur only) that is commonly used and reported in literature, because the areal capacity is directly related the energy density of the whole cell while the specific capacity only counts the active

material. The cycling rate at which the areal capacity delivered is important as well, since it would determine the power of the final cell. Another significant factor of the high areal capacity cells is the stability. Showing high areal capacities at the first few cycles means little to practical applications. Therefore we compared our cell performance with other Li-S cells claiming high energy density and demonstrating at least 100 cycles (Fig. 41, the value of areal capacity is extracted at the 100th cycle). First, we found almost all cells reported in literature are focused on the materials of cathode and they generally can be categorized into four groups: (1) CNT/S composite cathodes; (2) graphene or graphene oxide/S composite cathodes; (3) Mixed CNT and graphene or graphene oxide/S composite cathodes; and (4) others like using polymer or inorganic metal-based materials together with sulfur to make composite cathodes. In Fig. 41, most of the cells reported in literature show data points at the left and bottom corner, meaning a low areal capacity delivered at low current density. The rest of them are showing either a relatively high areal capacity but at low current density or a high current density but low areal capacity. In contrast, the Li-S cell equipped with our trench-wall CNTs enabled sulfur/lithium dual host illustrate a high capacity of 10.3 mAh cm^{-2} after 100 cycles with a cycling rate of 4.8 mA cm^{-2}, outperforming all previously reported cells considering the three critical factors – areal capacity, stability, and current density, for practical applications.

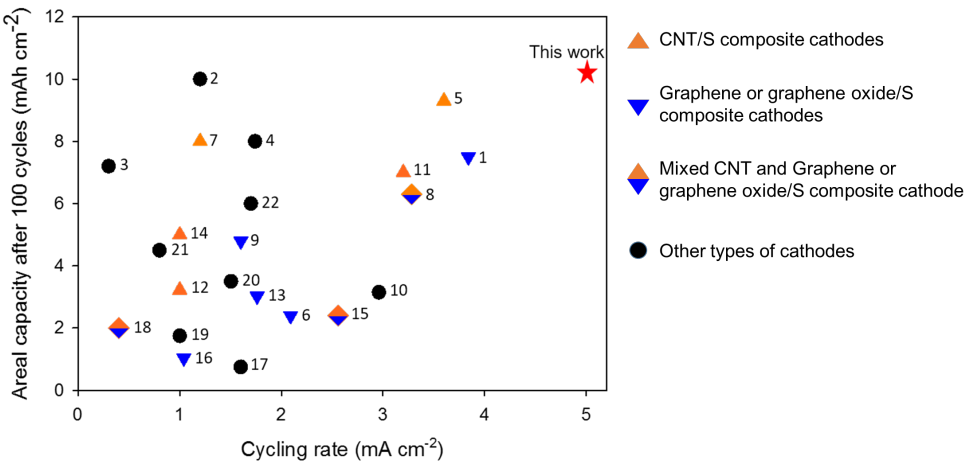

Figure 41 A comparison of this work and results in recently published articles.

It is worth noting that the trench-wall CNTs is, to our best knowledge, the first single material used to simultaneously and effectively tackle the problems from both cathode and anode sides. A significant merit of it comes to the anode side – safe and reliable lithium anode with high areal capacity, which has been regarded as the ultimate anode for all lithium-based batteries. The electrochemical performance of our Li@MC-CNT-H anode were characterized in symmetric cell configuration and compared with the bare Li metal counterpart. Fig. 42a and b compare the voltage profiles of them at two cycling rates and same cycling capacity (41.7 mAh cm^{-2}). At lower cycling rate (8.3 mA cm^{-2}, Fig. 42a), Li@MC-CNT-H showed stable cycling with small hysteresis, compared to the large (~3 times larger) and gradually enlarged hysteresis from profiles of pure lithium metal. The small hysteresis corresponds to a better kinetics, which proves our hypothesis that trench-wall CNTs provide a lithiophilic surface favorable for lithium deposition and stripping. When the cycling rate is doubled, the hysteresis increased for both of them, but Li@MC-CNT-H still maintained a much smaller value (~ 50% of that

from pure lithium metal), indicating its consistently better performance. The superior capability of being a lithium host was also found when tested in the cell configuration of Li/MC-CNT-H. The cell showed a stable cycling performance for more than 900 cycles at an extremely high cycling rate of 30 mA cm^{-2}. We also noticed that there is a capacity increase at the beginning, which is likely to be an activation process. In this cell configuration, lithium was incorporated into the trench-wall CNT host in an electrochemical way (during charging) instead of being thermally infused into the MC-CNT-H before cell assembly like those anodes used by previously mentioned cells. Due to the thickness of MC-CNT-H, the electrochemical incorporation of lithium happened in a non-uniform way at the beginning due to the electrolyte concentration gradient along the thickness direction. As cycle continued, the wetting condition of the MC-CNT-H surface became more uniform along with a better distribution of electrolyte within the MC-CNT-H.

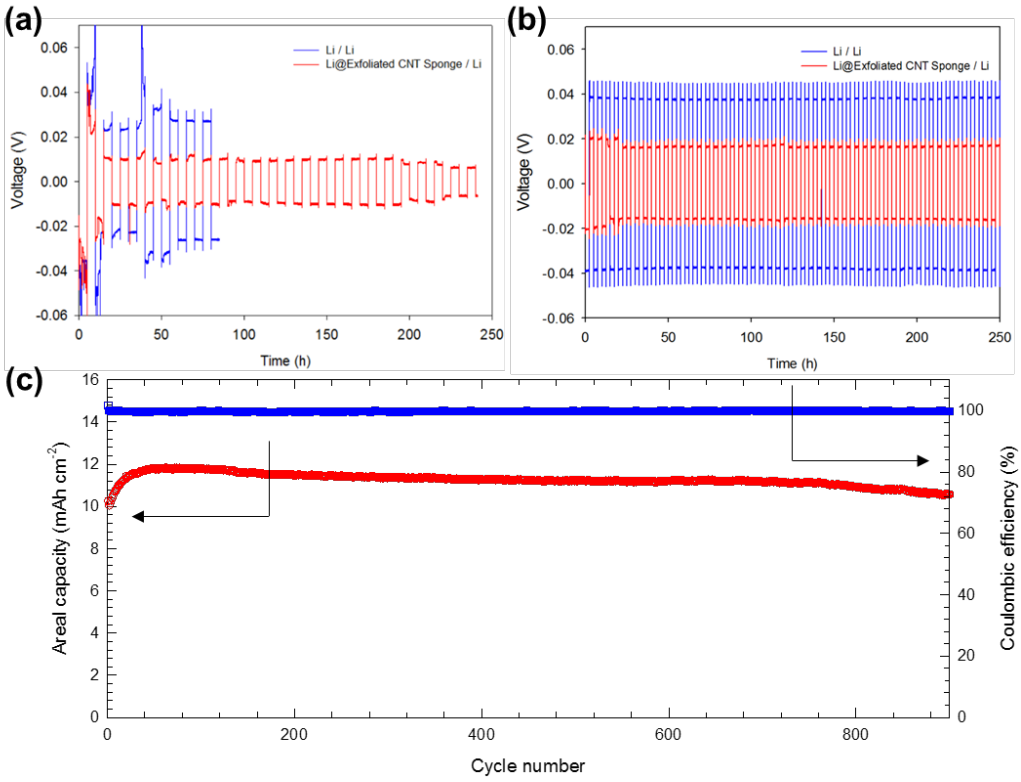

Figure 42 Electrochemical characterization of MC-CNT anode.

5.4 Conclusions

In this work, we developed a unique trench-wall CNTs framework which can function as a free-standing sulfur/lithium dual host, which is the first reported material to effectively tackle the challenges from both cathode and anode sides to achieve high energy Li-S batteries. The facile and controllable mechano-chemical method was developed to create unique nano-trenches on the wall of CNTs and turn the surface to polysulfide-philic and lithiophilic. A manufacture-friendly cathode fabrication process has been developed to make sandwich-type cathodes with high sulfur loading. The anode enabled by trench-wall CNTs with thermally infused lithium demonstrated stable performance at high

current density and high areal capacity, indicating a reliable ultimate anode for all types of lithium-based batteries. The cell with trench-wall CNTs as sulfur and lithium host at cathode and anode side, respectively, exhibits outstanding electrochemical performances with so far the highest areal capacity retention after 100 cycles under high current density. We believe our dual-host design shed light on the material and structure development for high energy density batteries in practical application.

CHAPTER V

CONCLUSIONS

Throughout my Ph.D. research, I have invented a new carbon based material – carbon nanotube sponge, which has a self-standing porous structure constructed entirely by multi-wall carbon nanotubes. The highly conductive nature enables its wide applications in battery electrodes and fuel cell catalysts. Through logic design on morphology, microstructure, and surface functionality, materials fabricated with the carbon nanotube sponge as the base material demonstrated largely enhanced electrochemical performances, shedding light on the material design for energy conversion and storage systems.

REFERENCES

1. M. Winter and R. J. Brodd, *Chem Rev*, 2004, **104**, 4245-4269.
2. J. Zhang, Z. Xia and L. Dai, *Sci Adv*, 2015, **1**, e1500564.
3. D. Strmcnik, M. Escudero-Escribano, K. Kodama, V. R. Stamenkovic, A. Cuesta and N. M. Markovic, *Nat Chem*, 2010, **2**, 880-885.
4. M. Lefevre, E. Proietti, F. Jaouen and J. P. Dodelet, *Science*, 2009, **324**, 71-74.
5. B. C. H. Steele and A. Heinzel, *Nature*, 2001, **414**, 345-352.
6. H. A. Gasteiger, S. S. Kocha, B. Sompalli and F. T. Wagner, *Appl Catal B-Environ*, 2005, **56**, 9-35.
7. F. Jaouen, E. Proietti, M. Lefevre, R. Chenitz, J. P. Dodelet, G. Wu, H. T. Chung, C. M. Johnston and P. Zelenay, *Energ Environ Sci*, 2011, **4**, 114-130.
8. G. Wu, C. M. Johnston, N. H. Mack, K. Artyushkova, M. Ferrandon, M. Nelson, J. S. Lezama-Pacheco, S. D. Conradson, K. L. More, D. J. Myers and P. Zelenay, *J Mater Chem*, 2011, **21**, 11392-11405.
9. R. Bashyam and P. Zelenay, *Nature*, 2006, **443**, 63-66.
10. E. Proietti, F. Jaouen, M. Lefevre, N. Larouche, J. Tian, J. Herranz and J. P. Dodelet, *Nat Commun*, 2011, **2**.
11. G. Wu, K. L. More, C. M. Johnston and P. Zelenay, *Science*, 2011, **332**, 443-447.
12. H. Alt, H. Binder and G. Sandstede, *Journal of Catalysis*, 1973, **28**, 8-19.
13. H. Jahnke, M. Schenborn, G. Zirnmermann, *Top. Curr. Chem.*, 1976, **61**.
14. A. Ishihara, Y. Ohgi, K. Matsuzawa, S. Mitsushima and K.-i. Ota, *Electrochimica Acta*, 2010, **55**, 8005-8012.

15. E. HaoYu, S. Cheng, K. Scott and B. Logan, *Journal of Power Sources*, 2007, **171**, 275-281.

16. M. Bron, J. Radnik, M. Fieber-Erdmann, P. Bogdanoff and S. Fiechter, *Journal of Electroanalytical Chemistry*, 2002, **535**, 113-119.

17. C. W. B. Bezerra, L. Zhang, K. Lee, H. Liu, A. L. B. Marques, E. P. Marques, H. Wang and J. Zhang, *Electrochimica Acta*, 2008, **53**, 4937-4951.

18. B. E. Logan and K. Rabaey, *Science*, 2012, **337**, 686-690.

19. R. A. Rozendal, H. V. M. Hamelers, K. Rabaey, J. Keller and C. J. N. Buisman, *Trends Biotechnol*, 2008, **26**, 450-459.

20. D. R. Lovley, *Curr Opin Biotech*, 2008, **19**, 564-571.

21. Y. A. Gorby, S. Yanina, J. S. McLean, K. M. Rosso, D. Moyles, A. Dohnalkova, T. J. Beveridge, I. S. Chang, B. H. Kim, K. S. Kim, D. E. Culley, S. B. Reed, M. F. Romine, D. A. Saffarini, E. A. Hill, L. Shi, D. A. Elias, D. W. Kennedy, G. Pinchuk, K. Watanabe, S. Ishii, B. Logan, K. H. Nealson and J. K. Fredrickson, *PNAS*, 2006, **103**, 11358-11363.

22. J. Wei, P. Liang and X. Huang, *Bioresource Technology*, 2011, **102**, 9335-9344.

23. Z. Du, H. Li and T. Gu, *Biotechnol Adv*, 2007, **25**, 464-482.

24. D. R. Lovley, *Curr Opin Biotechnol*, 2008, **19**, 564-571.

25. C. I. Torres, A. K. Marcus, H. S. Lee, P. Parameswaran, R. Krajmalnik-Brown and B. E. Rittmann, *FEMS Microbiol Rev*, 2010, **34**, 3-17.

26. K. Watanabe, M. Manefield, M. Lee and A. Kouzuma, *Curr Opin Biotechnol*, 2009, **20**, 633-641.

27. B. E. Logan, *Microbial Fuel Cells, 1st ed.*, John Wiley & Sons Inc. Hoboken, NJ, 2008.

28. S. L. Chen, H. Q. Hou, F. Harnisch, S. A. Patil, A. A. Carmona-Martinez, S. Agarwal, Y. Y. Zhang, S. Sinha-Ray, A. L. Yarin, A. Greiner and U. Schroder, *Energ Environ Sci*, 2011, **4**, 1417-1421.

29. Y. Fan, S. Xu, R. Schaller, J. Jiao, F. Chaplen and H. Liu, *Biosens Bioelectron*, 2011, **26**, 1908-1912.

30. J. Z. Sun, H.; Yang, Q.; Song, J.; Xue, A., *Electrochim Acta*, 2010, **55**, 3041–3047.

31. J. E. Mink, J. P. Rojas, B. E. Logan and M. M. Hussain, *Nano Lett*, 2012, **12**, 791-795.

32. N. Thepsuparungsikul, Phonthamachai, N, Ng, H. Y., *Water Sci Technol*, 2012, **65**, 1208-1214.

33. X. Xie, L. Hu, M. Pasta, G. F. Wells, D. Kong, C. S. Criddle and Y. Cui, *Nano Lett*, 2011, **11**, 291-296.

34. Y. Zhao, K. Watanabe and K. Hashimoto, *Phys Chem Chem Phys*, 2011, **13**, 15016-15021.

35. H. Y. W. Tsai, C.C.; Lee, C.Y.; Shih, E.P., *J Power Sources*, 2009, **194**, 199–205.

36. S. Ci, Wen, Z., Chen, J. & He, Z., *Electrochem Commun*, 2012, **14**, 71–74.

37. T. Sharma, Reddy, A. L. M., Chandra, T. S. & Ramaprabhu, S., *Int J Hydrogen Energy*, 2008, **33**, 6749–6754.

38. D. Larcher and J. M. Tarascon, *Nat Chem*, 2015, **7**, 19-29.

39. J. M. Tarascon and M. Armand, *Nature*, 2001, **414**, 359-367.

40. K. Mizushima, P. C. Jones, P. J. Wiseman and J. B. Goodenough, *Mater Res Bull*, 1980, **15**, 783-789.

41. M. M. Thackeray, W. I. F. David, P. G. Bruce and J. B. Goodenough, *Mater Res Bull*, 1983, **18**, 461-472.

42. R. Van Noorden, *Nature*, 2014, **507**, 26-28.

43. X. L. Ji, K. T. Lee and L. F. Nazar, *Nat Mater*, 2009, **8**, 500-506.

44. Y.-X. Yin, S. Xin, Y.-G. Guo and L.-J. Wan, *Angewandte Chemie International Edition*, 2013, **52**, 13186-13200.

45. E. Proietti, F. Jaouen, M. Lefevre, N. Larouche, J. Tian, J. Herranz and J. P. Dodelet, *Nat Commun*, 2011, **2**.

46. H. L. Wang, Y. Y. Liang, Y. G. Li and H. J. Dai, *Angew Chem Int Edit*, 2011, **50**, 10969-10972.

47. M. R. Gao, J. Jiang and S. H. Yu, *Small*, 2012, **8**, 13-27.

48. W. Zhou, J. Sunarso, M. W. Zhao, F. L. Liang, T. Klande and A. Feldhoff, *Angew Chem Int Edit*, 2013, **52**, 14036-14040.

49. Y. Y. Liang, H. L. Wang, J. G. Zhou, Y. G. Li, J. Wang, T. Regier and H. J. Dai, *J Am Chem Soc*, 2012, **134**, 3517-3523.

50. Y. Liang, Y. Li, H. Wang and H. Dai, *J Am Chem Soc*, 2013, **135**, 2013-2036.

51. R. Silva, D. Voiry, M. Chhowalla and T. Asefa, *J Am Chem Soc*, 2013, **135**, 7823-7826.

52. K. Gong, F. Du, Z. Xia, M. Durstock and L. Dai, *Science*, 2009, **323**, 760-764.

53. H. Jin, H. M. Zhang, H. X. Zhong and J. L. Zhang, *Energ Environ Sci*, 2011, **4**, 3389-3394.

54. Y. Li, W. Zhou, H. Wang, L. Xie, Y. Liang, F. Wei, J. C. Idrobo, S. J. Pennycook and H. Dai, *Nature nanotechnology*, 2012, **7**, 394-400.

55. L. Lin, Q. Zhu and A.-W. Xu, *J Am Chem Soc*, 2014, **136**, 11027-11033.

56. J. Herranz, F. Jaouen, M. Lefevre, U. I. Kramm, E. Proietti, J. P. Dodelet, P. Bogdanoff, S. Fiechter, I. Abs-Wurmbach, P. Bertrand, T. M. Arruda and S. Mukerjee, *J Phys Chem C*, 2011, **115**, 16087-16097.

57. B. Wang, *J Power Sources*, 2005, **152**, 1-15.

58. H. Yin, C. Zhang, F. Liu and Y. Hou, *Adv. Funct. Mater.*, 2014, **24**, 2930-2937.

59. H.-S. Oh and H. Kim, *J Power Sources*, 2012, **212**, 220-225.

60. X. C. Gui, J. Q. Wei, K. L. Wang, A. Y. Cao, H. W. Zhu, Y. Jia, Q. K. Shu and D. H. Wu, *Adv. Mater.*, 2010, **22**, 617-+.

61. L. B. Hu, H. Wu, Y. F. Gao, A. Y. Cao, H. B. Li, J. McDough, X. Xie, M. Zhou and Y. Cui, *Adv. Energy Mater.*, 2011, **1**, 523-527.

62. Z. P. Zeng, X. C. Gui, Z. Q. Lin, L. H. Zhang, Y. Jia, A. Y. Cao, Y. Zhu, R. Xiang, T. Z. Wu and Z. K. Tang, *Adv. Mater.*, 2013, **25**, 1185-1191.

63. X. C. Gui, Z. P. Zeng, Y. Zhu, H. B. Li, Z. Q. Lin, Q. M. Gan, R. Xiang, A. Y. Cao and Z. K. Tang, *Adv. Mater.*, 2014, **26**, 1248-1253.

64. Q. Y. Peng, Y. B. Li, X. D. He, X. C. Gui, Y. Y. Shang, C. H. Wang, C. Wang, W. Q. Zhao, S. Y. Du, E. Z. Shi, P. X. Li, D. H. Wu and A. Y. Cao, *Adv. Mater.*, 2014, **26**, 3241-+.

65. X. Pu, G. Yang and C. Yu, *Adv. Mater.*, 2014, **26**, 7456-7461.

66. H. M. Cheng, F. Li, G. Su, H. Y. Pan, L. L. He, X. Sun and M. S. Dresselhaus, *Appl. Phys. Lett.*, 1998, **72**, 3282-3284.

67. C. Yu and J. Park, *J. Solid State Chem.*, 2010, **183**, 2268-2273.

68. J. Park, Y. Ryu, H. Kim and C. Yu, *Nanotechnology*, 2009, **20**, 105608:105601-105608.

69. Y. Ryu and C. Yu, *J. Mater. Chem.*, 2012, **22**, 6959-6964.

70. M. S. Dresselhaus, A. Jorio and R. Saito, *Annu. Rev. Condens. Matter. Phys.*, 2010, **1**, 89-108.

71. S. Kundu, T. C. Nagaiah, W. Xia, Y. M. Wang, S. Van Dommele, J. H. Bitter, M. Santa, G. Grundmeier, M. Bron, W. Schuhmann and M. Muhler, *J Phys Chem C*, 2009, **113**, 14302-14310.

72. I. Hijazi, T. Bourgeteau, R. Cornut, A. Morozan, A. Filoramo, J. Leroy, V. Derycke, B. Jousselme and S. Campidelli, *J Am Chem Soc*, 2014, **136**, 6348-6354.

73. Y. Zhu, B. Zhang, X. Liu, D.-W. Wang and D. S. Su, *Angew Chem Int Edit*, 2014, DOI: 10.1002/anie.201405314, n/a-n/a.

74. T. Xing, Y. Zheng, L. H. Li, B. C. C. Cowie, D. Gunzelmann, S. Z. Qiao, S. M. Huang and Y. Chen, *Acs Nano*, 2014, **8**, 6856-6862.

75. M. K. Debe, *Nature*, 2012, **486**, 43-51.

76. F. Jaouen, E. Proietti, M. Lefevre, R. Chenitz, J. P. Dodelet, G. Wu, H. T. Chung, C. M. Johnston and P. Zelenay, *Energ Environ Sci*, 2011, **4**, 114-130.

77. K. Artyushkova, B. Kiefer, B. Halevi, A. Knop-Gericke, R. Schlogl and P. Atanassov, *Chem Commun*, 2013, **49**, 2539-2541.

78. G. Faubert, R. Cote, J. P. Dodelet, M. Lefevre and P. Bertrand, *Electrochim Acta*, 1999, **44**, 2589-2603.

79. G. Faubert, R. Cote, D. Guay, J. P. Dodelet, G. Denes and P. Bertrand, *Electrochim Acta*, 1998, **43**, 341-353.

80. T. Droubay and S. Chambers, *Phys. Rev. B*, 2001, **64**.

81. A. P. Grosvenor, B. A. Kobe, M. C. Biesinger and N. S. McIntyre, *Surf. Interface Anal.*, 2004, **36**, 1564-1574.

82. T. Fujii, *Phys. Rev. B: Condens. Matter*, 1999, **59**, 3195-3202.

83. S. J. Li, H. Yumoto, M. Shimotomai and M. Ishihara, *Thin Solid Films*, 1999, **345**, 23-28.

84. J. S. Moon, Y. W. Lee, S. B. Han, D. H. Kwak, K. H. Lee, A. R. Park, J. I. Sohn, S. N. Cha and K. W. Park, *Physical Chemistry Chemical Physics : PCCP*, 2014, **16**, 14644-14650.

85. L. Qu, Y. Liu, J.-B. Baek and L. Dai, *Acs Nano*, 2010, **4**, 1321-1326.

86. G. Nam, J. Park, S. T. Kim, D. B. Shin, N. Park, Y. Kim, J. S. Lee and J. Cho, *Nano Letters*, 2014, **14**, 1870-1876.

87. H. T. Chung, J. H. Won and P. Zelenay, *Nat Commun*, 2013, **4**.

88. G. Reguera, K. D. McCarthy, T. Mehta, J. S. Nicoll, M. T. Tuominen and D. R. Lovley, *Nature*, 2005, **435**, 1098-1101.

89. H. Rismani-Yazdi, S. M. Carver, A. D. Christy and O. H. Tuovinen, *J. Power Sources*, 2008, **180**, 683-694.

90. B. Erable, D. Féron and A. Bergel, *ChemSusChem*, 2012, **5**, 975-987.

91. Y. Qiao, S.-J. Bao and C. M. Li, *Energy Environ. Sci.*, 2010, **3**, 544-553.

92. R. A. Rozendal, H. V. M. Hamelers, K. Rabaey, J. Keller and C. J. N. Buisman, *Trends Biotechnol.*, 2008, **26**, 450-459.

93. K. Ben Liew, W. R. W. Daud, M. Ghasemi, J. X. Leong, S. Su Lim and M. Ismail, *Int. J. Hydrogen Energy*, 2014, **39**, 4870-4883.

94. L. Jourdin, S. Freguia, B. C. Donose, J. Chen, G. G. Wallace, J. Keller and V. Flexer, *J. Mater. Chem. A*, 2014, **2**, 13093-13102.

95. Y. Ren, D. Pan, X. Li, F. Fu, Y. Zhao and X. Wang, *J. Chem. Technol. Biotechnol.*, 2013, **88**, 1946-1950.

96. M. Lu, L. Guo, S. Kharkwal, H. n. Wu, H. Y. Ng and S. F. Y. Li, *J. Power Sources*, 2013, **221**, 381-386.

97. J. R. Kim, J.-Y. Kim, S.-B. Han, K.-W. Park, G. D. Saratale and S.-E. Oh, *Bioresour. Technol.*, 2011, **102**, 342-347.

98. X. Xia, F. Zhang, X. Zhang, P. Liang, X. Huang and B. E. Logan, *ACS Appl. Mater. Interfaces*, 2013, **5**, 7862-7866.

99. L. Wang, P. Liang, J. Zhang and X. Huang, *Bioresour. Technol.*, 2011, **102**, 5093-5097.

100. S. Khilari, S. Pandit, M. M. Ghangrekar, D. Das and D. Pradhan, *RSC Adv.*, 2013, **3**, 7902-7911.

101. Y. Zhang, Y. Hu, S. Li, J. Sun and B. Hou, *J. Power Sources*, 2011, **196**, 9284-9289.

102. J. M. Morris, S. Jin, J. Wang, C. Zhu and M. A. Urynowicz, *Electrochem. Commun.*, 2007, **9**, 1730-1734.

103. L. Feng, Y. Yan, Y. Chen and L. Wang, *Energy Environ. Sci.*, 2011, **4**, 1892-1899.

104. L. Feng, Y. Chen and L. Chen, *ACS Nano*, 2011, **5**, 9611-9618.

105. Y. Liu, H. Liu, C. Wang, S.-X. Hou and N. Yang, *Environ. Sci. Technol.*, 2013, **47**, 13889-13895.

106. X. Yang, W. Zou, Y. Su, Y. Zhu, H. Jiang, J. Shen and C. Li, *J. Power Sources*, 2014, **266**, 36-42.

107. X. Xie, M. Pasta, L. Hu, Y. Yang, J. McDonough, J. Cha, C. S. Criddle and Y. Cui, *Energy Environ. Sci.*, 2011, **4**, 1293-1297.

108. H. Wang, Z. Wu, A. Plaseied, P. Jenkins, L. Simpson, C. Engtrakul and Z. Ren, *J. Power Sources*, 2011, **196**, 7465-7469.

109. Y. Chen, Z. Lv, J. Xu, D. Peng, Y. Liu, J. Chen, X. Sun, C. Feng and C. Wei, *J. Power Sources*, 2012, **201**, 136-141.

110. K. B. Liew, W. R. Wan Daud, M. Ghasemi, K. S. Loh, M. Ismail, S. S. Lim and J. X. Leong, *Int. J. Hydrogen Energy*.

111. X.-W. Liu, X.-F. Sun, Y.-X. Huang, G.-P. Sheng, S.-G. Wang and H.-Q. Yu, *Energy Environ. Sci.*, 2011, **4**, 1422-1427.

112. Y. Yuan, B. Zhao, Y. Jeon, S. Zhong, S. Zhou and S. Kim, *Bioresour. Technol.*, 2011, **102**, 5849-5854.

113. G. Yang, W. Choi, X. Pu and C. Yu, *Energy Environ. Sci.*, 2015, DOI: 10.1039/C5EE00682A.

114. C. Erbay, S. Carreon-Bautista, E. Sanchez-Sinencio and A. Han, *Environ. Sci. Technol.*, 2014, **48**, 13992-13999.

115. C. Erbay, X. Pu, W. Choi, M.-J. Choi, Y. Ryu, H. Hou, F. Lin, P. de Figueiredo, C. Yu and A. Han, *J. Power Sources*, 2015, **280**, 347-354.

116. H. Hou, L. Li, C. U. Ceylan, A. Haynes, J. Cope, H. H. Wilkinson, C. Erbay, P. d. Figueiredo and A. Han, *Lab Chip*, 2012, **12**, 4151-4159.

117. H. Hou, L. Li, Y. Cho, P. de Figueiredo and A. Han, *PloS one*, 2009, **4**, e6570.

118. Y. Ahn, I. Ivanov, T. C. Nagaiah, A. Bordoloi and B. E. Logan, *J. Power Sources*, 2014, **269**, 212-215.

119. L. Y. Feng, L. Q. Yang, Z. J. Huang, J. Y. Luo, M. Li, D. B. Wang and Y. G. Chen, *Sci Rep-Uk*, 2013, **3**.

120. Z. H. Wen, S. Q. Ci, F. Zhang, X. L. Feng, S. M. Cui, S. Mao, S. L. Luo, Z. He and J. H. Chen, *Adv Mater*, 2012, **24**, 1399-1404.

121. E. B. Barros, N. S. Demir, A. G. Souza Filho, J. Mendes Filho, A. Jorio, G. Dresselhaus and M. S. Dresselhaus, *Phys. Rev. B*, 2005, **71**.

122. Z. H. Ni, H. M. Wang, Y. Ma, J. Kasim, Y. H. Wu and Z. X. Shen, *ACS Nano*, 2008, **2**, 1033-1039.

123. B. Guo, Q. Liu, E. Chen, H. Zhu, L. Fang and J. R. Gong, *Nano Lett.*, 2010, **10**, 4975-4980.

124. A. Peigney, C. Laurent, E. Flahaut, R. R. Bacsa and A. Rousset, *Carbon*, 2001, **39**, 507-514.

125. S. L. Gojkovic, S. Gupta and R. F. Savinell, *J Electroanal Chem*, 1999, **462**, 63-72.

126. R. Z. Jiang and F. C. Anson, *J Electroanal Chem*, 1991, **305**, 171-184.

127. G. Tamizhmani, J. P. Dodelet, D. Guay and G. Lalande, *J Electrochem Soc*, 1994, **141**, 41-45.

128. G. Lalande, G. Faubert, R. Cote, D. Guay, J. P. Dodelet, L. T. Weng and P. Bertrand, *J Power Sources*, 1996, **61**, 227-237.

129. G. Lalande, R. Cote, D. Guay, J. P. Dodelet, L. T. Weng and P. Bertrand, *Electrochim Acta*, 1997, **42**, 1379-1388.

130. P. G. Bruce, S. A. Freunberger, L. J. Hardwick and J. M. Tarascon, *Nature Mater.*, 2012, **11**, 19-29.

131. X. Ji and L. F. Nazar, *J. Mater. Chem.*, 2010, **20**, 9821-9826.

132. X. Pu, G. Yang and C. Yu, *Adv Mater*, 2014, **26**, 7456-7461.

133. X. Pu and C. Yu, *Nanoscale*, 2012, **4**, 6743-6747.

134. X. Pu, L. Yin and C. Yu, *J Nanopart Res*, 2012, **14**, 1-7.

135. X. Ji, K. Lee and L. Nazar, *Nature Mater.*, 2009, **8**, 500-506.

136. S. Xin, L. Gu, N.-H. Zhao, Y.-X. Yin, L.-J. Zhou, Y.-G. Guo and L.-J. Wan, *J. Am. Chem. Soc.*, 2012, **134**, 18510-18513.

137. L. Xiao, Y. Cao, J. Xiao, B. Schwenzer, M. H. Engelhard, L. V. Saraf, Z. Nie, G. J. Exarhos and J. Liu, *Adv. Mater.*, 2012, **24**, 1176-1181.

138. Y. Yang, G. Yu, J. J. Cha, H. Wu, M. Vosgueritchian, Y. Yao, Z. Bao and Y. Cui, *ACS Nano*, 2011, **5**, 9187-9193.

139. R. Demir-Cakan, M. Morcrette, Gangulibabu, A. Gueguen, R. Dedryvere and J.-M. Tarascon, *Energy Env. Sci.*, 2013, **6**, 176-182.

140. L. Suo, Y.-S. Hu, H. Li, M. Armand and L. Chen, *Nat. Commun.*, 2013, **4**, 1481.

141. Y.-S. Su and A. Manthiram, *Nat. Commun.*, 2012, **3**, 1166.

142. Y. Yang, G. Zheng and Y. Cui, *Energy Env. Sci.*, 2013, **6**, 1552-1558.

143. C. Barchasz, F. Mesguich, J. Dijon, J.-C. Leprêtre, S. Patoux and F. Alloin, *J. Power Sources*, 2012, **211**, 19-26.

144. S. S. Zhang and J. A. Read, *J. Power Sources*, 2012, **200**, 77-82.

145. X. Pu, G. Yang and C. Yu, *Adv. Mater.*, 2014, **26**, 7456-7461.

146. R. D. Rauh, K. M. Abraham, G. F. Pearson, J. K. Surprenant and S. B. Brummer, *J. Electrochem. Soc.*, 1979, **126**, 523-527.

147. S. S. Zhang, *Electrochem Commun*, 2013, **31**, 10-12.

148. K. Hata, D. N. Futaba, K. Mizuno, T. Namai, M. Yumura and S. Iijima, *Science*, 2004, **306**, 1362-1364.

149. P. B. Amama, C. L. Pint, L. McJilton, S. M. Kim, E. A. Stach, P. T. Murray, R. H. Hauge and B. Maruyama, *Nano Lett.*, 2008, **9**, 44-49.

150. Y. Ryu, L. Yin and C. Yu, *J. Mater. Chem.*, 2012, **22**, 6959-6964.

151. Y. Ryu, D. Freeman and C. Yu, *Carbon*, 2011, **49**, 4745-4751.

152. S. L. Kim, K. Choi, A. Tazebay and C. Yu, *ACS Nano*, 2014, **8**, 2377-2386.

153. C. Yu, Y. Ryu, L. Yin and H. Yang, *ACS Nano*, 2011, **5**, 1297–1303.

154. Y. Ryu and C. Yu, *Solid State Comm.*, 2011, **151**, 1932-1935.

155. X. Wang, Q. Xiang, B. Liu, L. Wang, T. Luo, D. Chen and G. Shen, *Sci. Rep.*, 2013, **3**.

156. Q. Wang, J. Zheng, E. Walter, H. Pan, D. Lv, P. Zuo, H. Chen, Z. D. Deng, B. Y. Liaw, X. Yu, X. Yang, J.-G. Zhang, J. Liu and J. Xiao, *Journal of The Electrochemical Society*, 2015, **162**, A474-A478.

157. R. Xu, I. Belharouak, J. C. M. Li, X. Zhang, I. Bloom and J. Bareño, *Adv. Energy Mater.*, 2013, **3**, 833-838.

158. X. Li, Y. Cao, W. Qi, L. V. Saraf, J. Xiao, Z. Nie, J. Mietek, J.-G. Zhang, B. Schwenzer and J. Liu, *J. Mater. Chem.*, 2011, **21**, 16603-16610.

159. S. Zhang, *Energies*, 2012, **5**, 5190-5197.

160. J.-H. Hsu, W. Choi, G. Yang and C. Yu, *Organic Electronics*, 2017, **45**, 182-189.

161. C. P. Grey and J. M. Tarascon, *Nat Mater*, 2017, **16**, 45-56.

162. J. Lu, Z. H. Chen, Z. F. Ma, F. Pan, L. A. Curtiss and K. Amine, *Nat Nanotechnol*, 2016, **11**, 1031-1038.

163. J. B. Goodenough and K. S. Park, *J Am Chem Soc*, 2013, **135**, 1167-1176.

164. S. Chu and A. Majumdar, *Nature*, 2012, **488**, 294-303.

165. M. Armand and J. M. Tarascon, *Nature*, 2008, **451**, 652-657.

166. P. G. Bruce, S. A. Freunberger, L. J. Hardwick and J. M. Tarascon, *Nat Mater*, 2012, **11**, 19-29.

167. Q. Pang, X. Liang, C. Y. Kwok and L. F. Nazar, *Nat Energy*, 2016, **1**.

168. A. Manthiram, Y. Z. Fu, S. H. Chung, C. X. Zu and Y. S. Su, *Chem Rev*, 2014, **114**, 11751-11787.

169. Y. X. Yin, S. Xin, Y. G. Guo and L. J. Wan, *Angew Chem Int Edit*, 2013, **52**, 13186-13200.

170. D. Lv, J. Zheng, Q. Li, X. Xie, S. Ferrara, Z. Nie, L. B. Mehdi, N. D. Browning, J.-G. Zhang, G. L. Graff, J. Liu and J. Xiao, *Advanced Energy Materials*, 2015, **5**, 1402290-n/a.

171. M. A. Pope and I. A. Aksay, *Advanced Energy Materials*, 2015, **5**, 1500124-n/a.

172. J. Song, Z. Yu, M. L. Gordin and D. Wang, *Nano Letters*, 2016, **16**, 864-870.

173. W. Zhou, B. Guo, H. Gao and J. B. Goodenough, *Advanced Energy Materials*, 2016, **6**, 1502059-n/a.

174. G. Yang, W. Choi, X. Pu and C. Yu, *Energ Environ Sci*, 2015, **8**, 1799-1807.

175. X. Pu, G. Yang and C. H. Yu, *J Electrochem Soc*, 2015, **162**, A1396-A1400.

176. D. V. Kosynkin, A. L. Higginbotham, A. Sinitskii, J. R. Lomeda, A. Dimiev, B. K. Price and J. M. Tour, *Nature*, 2009, **458**, 872-U875.

177. D. Lin, Y. Liu, Z. Liang, H.-W. Lee, J. Sun, H. Wang, K. Yan, J. Xie and Y. Cui, *Nat Nano*, 2016, **11**, 626-632.

178. G. Bieker, M. Winter and P. Bieker, *Phys Chem Chem Phys*, 2015, **17**, 8670-8679.

179. Z. F. Deng, Z. A. Zhang, Y. Q. Lai, J. Liu, J. Li and Y. X. Liu, *J Electrochem Soc*, 2013, **160**, A553-A558.

180. N. A. Canas, K. Hirose, B. Pascucci, N. Wagner, K. A. Friedrich and R. Hiesgen, *Electrochim Acta*, 2013, **97**, 42-51.

181. S. Risse, N. A. Canas, N. Wagner, E. Hark, M. Ballauff and K. A. Friedrich, *J Power Sources*, 2016, **323**, 107-114.